MINISTÉRIO DA CIÊNCIA, TECNOLOGIA, INOVAÇÕES E COMUNICAÇÕES
INSTITUTO NACIONAL DE PESQUISAS ESPACIAIS

sid.inpe.br/mtc-m21b/2017/06.10.13.55-TDI

SEASONAL MONITORING OF ATMOSPHERIC CONSTITUENTS USING MULTI-ANGLE MODIS DATA AS SUPPORT FOR ATMOSPHERIC CORRECTION IN THE AMAZON REGION

Vitor Souza Martins

Master's Dissertation of the Graduate Course in Remote Sensing, guided by Drs. Cláudio Clemente Faria Barbosa, and Lino Augusto Sander de Carvalho, approved in May 26, 2017.

URL of the original document:
<http://urlib.net/8JMKD3MGP3W34P/3P44SHH>

INPE
São José dos Campos
2017

PUBLISHED BY:

Instituto Nacional de Pesquisas Espaciais - INPE
Gabinete do Diretor (GB)
Serviço de Informação e Documentação (SID)
Caixa Postal 515 - CEP 12.245-970
São José dos Campos - SP - Brasil
Tel.:(012) 3208-6923/6921
E-mail: pubtc@inpe.br

MINISTÉRIO DA CIÊNCIA, TECNOLOGIA, INOVAÇÕES E COMUNICAÇÕES
INSTITUTO NACIONAL DE PESQUISAS ESPACIAIS

sid.inpe.br/mtc-m21b/2017/06.10.13.55-TDI

SEASONAL MONITORING OF ATMOSPHERIC CONSTITUENTS USING MULTI-ANGLE MODIS DATA AS SUPPORT FOR ATMOSPHERIC CORRECTION IN THE AMAZON REGION

Vitor Souza Martins

Master's Dissertation of the Graduate Course in Remote Sensing, guided by Drs. Cláudio Clemente Faria Barbosa, and Lino Augusto Sander de Carvalho, approved in May 26, 2017.

URL of the original document:
<http://urlib.net/8JMKD3MGP3W34P/3P44SHH>

INPE
São José dos Campos
2017

Cataloging in Publication Data

Martins, Vitor Souza.

M366s Seasonal monitoring of atmospheric constituents using multi-angle MODIS data as support for atmospheric correction in the Amazon region / Vitor Souza Martins. – São José dos Campos : INPE, 2017.

xxx + 145 p. ; (sid.inpe.br/mtc-m21b/2017/06.10.13.55-TDI)

Dissertation (Master in Remote Sensing) – Instituto Nacional de Pesquisas Espaciais, São José dos Campos, 2017.

Guiding : Drs. Cláudio Clemente Faria Barbosa, and Lino Augusto Sander de Carvalho.

1. Aerosol monitoring. 2. MAIAC-MODIS. 3. Atmospheric correction. 4. Amazon atmosphere. I.Title.

CDU 528.8:504.5(811.3)

Aluno (a): *Vítor Souza Martins*

Título: "SEASONAL MONITORING OF ATMOSPHERIC CONSTITUENTS USING MULTI-ANGLE MODIS DATA AS SUPPORT FOR ATMOSPHERIC CORRECTION IN THE AMAZON REGION"

Aprovado (a) pela Banca Examinadora em cumprimento ao requisito exigido para obtenção do Título de *Mestre* em *Sensoriamento Remoto*

Dra. Evlyn Márcia Leão de Moraes Novo

Presidente / INPE / SJCampos - SP

Dr. Cláudio Clemente Faria Barbosa

Orientador(a) / INPE / SJCampos - SP

Dr. Lino Augusto Sander de Carvalho

Orientador(a) / INPE / São José dos Campos - SP

Dr. Yosio Edemir Shimabukuro

Membro da Banca / INPE / São José dos Campos - SP

Dr. Mauro Antonio Homem Antunes

Convidado(a) / UFRRJ / Seropédica - RJ

Este trabalho foi aprovado por:

( ) maioria simples

(X) unanimidade

São José dos Campos, 26 de maio de 2017

"O conhecimento amplia a vida. Conhecer é viver uma realidade que a ignorância impede desfrutar."

Carlos Bernardo González Pecotche

Dedico a meus pais, Antônio e Claudia
A minha irmã, Clarice e a meus avós.

Com amor.

ACKNOWLEDGEMENTS

Aos meus orientadores, Dr. Claudio C.F. Barbosa e Dr. Lino A. S. de Carvalho, pela dedicação, aprendizado, amizade e confiança no desenvolvimento deste trabalho. O apoio de vocês contribuiu muito para minha formação acadêmica. Agradeço pela experiência vivida na região amazônica e aos amigos do Laboratório de Instrumentação de Sistemas Aquáticos (LabISA).

Agradeço ao Programa de Pós-Graduação do Instituto Nacional de Pesquisas Espaciais (INPE), aos professores do SERE pelo conhecimento, e à Coordenação de Aperfeiçoamento de Pessoal de Nível Superior (CAPES), pelo auxílio financeiro. A todos os meus amigos do INPE, obrigado pelos bons momentos.

Um agradecimento especial à Dr. Evlyn M. L. M. Novo pela amizade e apoio nessa etapa. Levarei comigo seus conselhos e uma admiração eterna.

I thank Dr. Alexei Lyapustin for all assistance and contribution with MAIAC data. I thank all AERONET PIs to efforts in maintaining the aerosol monitoring across South America. Ao Dr. Flavio J. Ponzoni pelas primeiras reflexões e “insights” sobre correção atmosférica.

A toda minha família, em especial a meu pai, Antônio, minha mãe, Cláudia, minha irmã, Clarice, pelo carinho que transformam a minha vida. A minha companheira, Flávia Xavier pelo carinho e paciência durante esse tempo. Aos amigos, Lucas, Bárbara, Matheus, Naná, Diego, Duda, Jorge e Conceição, pela amizade de sempre.

ABSTRACT

Satellite data provide the only viable means for systematic monitoring of remote and large ecosystem, such as Amazon. However, atmospheric attenuation distorts optical remote sensing measurements, and therefore, accurate atmospheric correction (A/C) is a key requirement for retrieving reliable surface reflectance (R_{sup}). In this sense, the knowledge of the seasonal patterns of cloud cover and atmospheric constituents is essential for remote sensing applications. Multi-angle Implementation of Atmospheric Correction (MAIAC) is a new Moderate Resolution Imaging Spectroradiometer (MODIS) algorithm that combines time series approach and image processing to derive surface reflectance and atmosphere products, such as aerosol optical depth (AOD), columnar water vapor, and cloud mask. In this research, three main analyses were performed: (i) validation of MAIAC AOD retrievals using ground-data from 19 AERONET sites in the South America; (ii) evaluation of seasonal pattern of cloud cover and key atmospheric constituents over the Amazon basin; and (iii) assessment of AC methods (6SV, ACOLITE and Sen2Cor) applied to MultiSpectral Instrument (MSI) Sentinel-2 image over Amazon floodplain lakes. In the first analysis (i), MAIAC AOD Terra/Aqua retrievals showed high agreement with ground-based AERONET measurements, with correlation coefficient (R) close to unity (R_{terra}: 0.956 and R_{Aqua}: 0.949). However, MAIAC accuracy varies with land cover type, and comparisons revealed a high fitness for cropland, forest, savanna and grassland covers, with more than 66% of retrievals within the expected error ($\Delta AOD = \pm 0.05 * AOD \pm 0.05$) and R exceeding 0.8 for both Terra and Aqua products. Over bright surfaces, however, MAIAC retrievals showed lower correlation than those of vegetated areas, and overestimated retrievals over shrubland and barren areas. In the second analysis (ii), the seasonal pattern of cloud cover and key atmospheric constituents presented clear distinction amongst four Amazon regions, with relative high (low) cloud cover and low (high) atmospheric loading during wet (dry) season, exception for water vapor content. The sub-basin analysis showed that Negro and Caqueta-Japurá sub-basins are under quasi-constant cloud cover (80-100%) throughout the year, while High-Madeira and Tapajos present a cloudiness regime during dry season. For the temporal analysis, drought years present the most critical regimes of aerosol loading, with a peak in September. In the last analysis (iii), A/C results of the MSI visible bands illustrate the limitation of the methods over dark lakes ($R_{sup} < 1\%$), and a better match of the R_{sup} shape compared with in-situ measurements over turbid lakes, although the accuracy varied depending on the spectral bands and methods. Particularly above 705 nm, R_{sup} was highly affected by adjacent effects of forest, and the proposed adjacency effect correction minimized the spectral distortions in R_{sup} (RMSE < 0.006). In conclusion, the availability of multi-angle MODIS products contributes with consistent information for both analyses of seasonal constituents and atmospheric correction, what opens a new endeavour for remote sensing studies over Amazon basin. Particularly for inland water, future studies should be focused on distinct surface-atmosphere conditions to assess the quality of these A/C methods.

Keywords: Aerosol monitoring. MAIAC-MODIS. Atmospheric correction. Amazon atmosphere.

MONITORAMENTO SAZONAL DOS CONSTITUINTES ATMOSFÉRICOS UTILIZANDO DADOS MULTIANGULARES DO SENSOR MODIS COMO SUPORTE PARA CORREÇÃO ATMOSFÉRICA NA REGIÃO AMAZÔNICA

RESUMO

Os dados orbitais fornecem uma única alternativa viável para o monitoramento sistemático de ecossistemas como a Amazônia. No entanto, a atenuação atmosférica da radiação solar distorce as medidas realizadas por sensores ópticos, portanto uma acurada correção atmosférica se torna indispensável para se obter dados consistentes de reflectância de superfície (R_{sup}). Nesse sentido, o conhecimento dos padrões sazonais dos principais constituintes atmosféricos e da frequência de nuvens é essencial para as aplicações do sensoriamento remoto óptico. Multi-angle Implementation of Atmospheric Correction (MAIAC) é um novo algoritmo aplicado ao sensor Moderate Resolution Imaging Spectroradiometer (MODIS). Esse algoritmo utiliza a abordagem do processamento de série temporal de imagens para geração de produtos em reflectância de superfície e extração de informações atmosféricas, como a profundidade óptica do aerossol (aerosol optical depth, AOD), a coluna de vapor d'água e a máscara de nuvem. Nesta pesquisa foram realizadas três principais análises: (i) a validação do produto MAIAC AOD utilizando medições in-situ de 19 estações da AERONET distribuídas na América do Sul; (ii) a análise dos padrões espaço-temporais referentes à frequência de nuvens e dos principais constituintes atmosféricos na região Amazônica; e (iii) a avaliação de métodos de correção atmosférica (6SV, ACOLITE e Sen2Cor) aplicados ao sensor MSI / Sentinel-2 em lagos de várzea na Amazônia. Na primeira análise (i), as estimativas de AOD do MAIAC Terra e Aqua demonstraram uma alta concordância com as medições in-situ da AERONET, com coeficientes de correlação (R) iguais a 0.956 (Terra) e 0.949 (Aqua). A acurácia do MAIAC varia com o tipo de cobertura. As comparações revelaram uma alta concordância das estimativas de AOD em áreas com agricultura, floresta, savana e pastagem - mais de 66% das estimativas ficaram dentro do erro esperado ($\Delta AOD = \pm 0.05 * AOD \pm 0.05$) e com R excedendo 0.8 para ambas as plataformas Terra e Aqua. No entanto, em áreas com alta reflectância de superfície (*bright surfaces*), as estimativas do MAIAC demonstraram uma baixa correlação quando comparadas àquelas em áreas vegetadas, em que se observa uma superestimativa dos valores para regiões sem vegetação (áridas) ou desérticas. Na segunda análise (ii), o padrão sazonal dos constituintes atmosféricos apresentou uma clara diferença entre os padrões sazonais das 4 regiões amazônicas (noroeste, central, nordeste e sul), com uma alta (baixa) cobertura de nuvens e baixa (alta) carga atmosférica durante o período úmido (seco), com exceção para as concentrações de vapor d'água. Os resultados por sub-bacias demonstraram que as bacias do Negro e da Caqueta-Japurá são fortemente afetadas pela alta frequêcia de nuvens (80 – 100%) ao longo do ano, enquanto Alto-Madeira e Tapajós apresentam uma janela temporal de 3 a 4 meses durante a estação seca com baixa cobertura de nuvens. Na análise temporal, os anos de seca extrema na região apresentaram as maiores cargas de aerossol, com os picos em setembro. Na análise (iii), os resultados da correção atmosférica nas bandas do visível ilustram a limitação dos métodos para os lagos com $R_{sup} < 1\%$ (*dark lakes*), enquanto em lagos de águas túrbidas há um melhor desempenho em relação a forma e

amplitude das curvas espectrais, embora a acurácia varie conforme a banda espectral e o método de correção. Em bandas espectrais com comprimentos de onda superiores a 705 nm, os valores de R_{sup} foram fortemente afetados pelos efeitos de adjacência relacionados à floresta, e o método proposto para correção da adjacência minimizou as distorções espectrais nos valores de R_{sup} (RMSE < 0.006). Como conclusão geral, a disponibilidade dos produtos multi-angulares do MAIAC contribui com uma nova fonte consistente de informações para ambas as análises de sazonalidade dos constituintes e correção atmosférica, o que abre novos esforços para aplicações na Amazônia. Para águas interiores em particular, os estudos futuros devem focar na aplicação dos métodos de correção atmosférica em diferentes condições de carga óptica e de tipos de água.

Palavras-chave: Monitoramento do aerossol. Produto MAIAC-MODIS. Correção atmosférica. Amazônia.

LIST OF FIGURES

Figure 2.1. Variation of the atmospheric temperature (Kevin) and pressure (hPa) in the 100 km of atmosphere. 6

Figure 2.2. Sources of natural and human-induced aerosol particles into atmosphere. 8

Figure 2.3. Basic scheme with vertical distribution of atmospheric constituents. 9

Figure 2.4. Extraterrestrial and terrestrial solar radiation from 0.25 to 3.0 µm. 10

Figure 2.5. Simulated transmittance of atmospheric water vapor (H2O), carbon dioxide (CO2), ozone (O3), nitrous oxide (N2O), carbon monoxide (CO), methane (CH4), oxygen (O2), and nitrogen dioxide (NO2). 11

Figure 2.6. Scattering distribution of solar radiation according to size parameter. 12

Figure 2.7. Atmospheric attenuation of ozone and water vapor (%) and scattering reflectance of Rayleigh and aerosol applied to TM/ Landsat 5. 13

Figure 2.8. Definition of extinction in homogeneous medium. 14

Figure 3.1. Geographical distribution of the AERONET sites. The code numbers identify AERONET sites described in Table 3.1. Background of Global Land Cover product (BROXTON et al., 2014) reclassified to seven land cover types. 27

Figure 3.2. Example of MAIAC aerosol loading on 08 September 2017 (dry season). (a) MODIS True-color image; (b) MAIAC AOD under partly cloudy (top-panel) and clear condition (bottom-panel). 28

Figure 3.3. Flow-chart of validation approach. 29

Figure 3.4. Scatter points of AOD550 versus Ångström exponent (440-670 nm) for land cover types. The scatter provides 5000 random pair-points from AERONET site per land cover type: Ji-Paraná SE (Cropland; Brown); São Paulo (Urban; Black); Manaus Embrapa (Forest; Green); Casleo (Shrubland/Barren; Gray); Ceilap RG (Savanna/grassland; Yellow). 34

Figure 3.5. Scatter plots of MAIAC Terra (a) and Aqua (b) against AERONET AOD550. The line 1:1 and MAIAC expected error (EE = ± 0.05 ± 0.05×AOD) are shown in solid blue and shaded gray area, respectively. In top-left text: regression equation, correlation coefficient (R), number of match-ups (n), and fraction of retrievals within EE. In bottom-right text: statistics binned by AOD intervals. 37

Figure 3.6. MAIAC-AERONET AOD bias (τM – τA) at 550 nm (y-axis) versus Ångström exponent (AE) from AERONET (x-axis). (a) AOD bias using all match-ups from both Terra and Aqua colored by binned AOD from AERONET retrieval. Match-ups are sorted by the AE and grouped into 50 equal bins for (b) lower and (c) higher than 0.4. Each box edge and whiskers represent the 25-75% and 5-95% of data with median (black line) and mean (red point). 38

Figure 3.7. Frequency distribution of MAIAC and AERONET AOD550. Text box: number of AOD550 values within interval, bias and number of match-ups (n). 39

Figure 3.8. Scatter plots of MAIAC and AERONET AOD550 comparisons for land cover types: Forest (a); shrubland and barren (b); savanna and grassland (c); cropland (d); urban (e); and mixed areas (f). The MAIAC Terra (i) and Aqua (ii) are presented for each land cover. The line 1:1 and MAIAC expected error (EE = ± (0.05 + 0.05×AOD)) are shown in solid blue and shaded gray area, respectively. In top-left text: regression equation, correlation coefficient (R), number of match-ups (n), and fraction within EE. In bottom-right text: statistics binned by AOD intervals. At least 15 match-ups were required to analysis binned by AOD. 43

Figure 3.9. Correlation analysis of AOD intervals using normalized RMSE versus correlation coefficient. Note the discontinuity in NRMSE-axis. At least 15 match-ups were required to perform this correlation analysis. 46

Figure 3.10. Spatial distribution of average MAIAC AOD550 within 2000-2015 for seasonal timescales: DJF (December-January–February), MAM (March-April–May), JJA (June-July–August) and SON (September-October–November). At least 15 match-ups of MAIAC vs. AERONET measurements were used to compute correlation coefficient per season. 48

Figure 3.11. Intercomparison of MAIAC Terra vs Aqua AOD retrievals in time series validation. The sample size (n) per year used to bias calculation and MAE is the mean absolute error (MAE). 53

Figure 4.1. The Amazon basin. AERONET sites used to validate MAIAC atmospheric observations: Manaus-Embrapa (2.89°S, 59.96°W) and Rio Branco (9.95°S, 67.86° W). 61

Figure 4.2. Block diagram of spatiotemporal analysis of 15-year MODIS atmospheric dataset: fraction of cloud cover (FCLOUD in percentage); aerosol optical depth at 550 nm (AOD550 nm unitless); total precipitable water (TPW in g.cm-2); total columnar ozone (TOZ in Dobson Units). 63

Figure 4.3. Temporal analysis of MAIAC AOD at 0.55 μm compared to AERONET measurements from Manaus (top panel) and Rio Branco (bottom panel) between 2011 and 2015. In the statistics text, n is the number of match-ups, So is the linear slope, correlation coefficient (R), root-mean-square-error (RMSE) between MAIAC and AERONET measurements. 65

Figure 4.4. Temporal analysis of MAIAC TPW (g.cm-2) compared to AERONET measurements from Manaus (top panel) and Rio Branco (bottom panel) between 2011 and 2015. In the statistics text, n is the number of match-ups, So is the linear slope, correlation coefficient (R), root-mean-square-error (RMSE) between MAIAC and AERONET measurements. 66

Figure 4.5. Seasonal distribution of key atmospheric constituent in the Amazon basin: fraction of cloud cover (FCLOUD in percentage); aerosol optical depth at 550 nm (AOD550 nm unitless); total precipitable water (TPW in g.cm-2); total columnar ozone (TOZ in Dobson Units). The line profiles represent the latitudinal and longitudinal averaged data in the quarter year (December-January-February (DJF); March-April-May (MAM); June-July-August (JJA); and September-October-November (SON). For example, the AOD average from SON season is presented in the Top-Left panel. The land cover context from MODIS Global Land Cover product is addressed here in the Bottom-Left panel. Background of Global Land Cover product (Broxton et al., 2014) reclassified to five land cover types. 68

Figure 4.6. Average precipitation and atmospheric constituents using 15-year data from Tropical Rainfall Measuring Mission (TRMM) and Moderate Resolution Imaging Spectroradiometer (MODIS) Terra products in the four regions. (a) Annual precipitation at 0.25° x 0.25° resolution and normalized coefficient of variation (CVnorm) resampled to 2.5° x 2.5° resolution. (b) Monthly precipitation from average TRMM data within 2000-2015 period; (c) Monthly cloud cover fraction

and atmospheric constituents from averaged data MODIS between Mar/2000 and Dec/2015. The y-axis of panels (c) shows the number of pixel for each concentration range: (ci) fraction of cloud cover, (cii) aerosol optical depth at 550 nm, (ciii) total precipitable water, (civ) total columnar ozone. 72

Figure 4.7. Time-series of quarterly bias (Δδ) for atmospheric constituents from Moderate Resolution Imaging Spectroradiometer (MODIS) Terra products in the four regions. (a) Fraction of cloud cover. (b) Aerosol optical depth at 550 nm. (c) Total precipitable water. (d) Total columnar ozone. The shaded vertical bar denotes the 2005, 2007, 2010, 2015 drought years (brown) and the 2009, 2012, 2014 flood years (blue) presented in Marengo and Espinoza (2016). 73

Figure 4.8. Time series of monthly cloud cover fraction and atmospheric constituents derived from Moderate Resolution Imaging Spectroradiometer (MODIS) Terra products in the six Amazon sub-basins. Centroid coordinates of sub-basins are presented in front of horizontal bar for each variable. 76

Figure 4.9. Seasonal pattern of atmospheric constituents in the six Amazon sub-basins: Napo-Putumayo-Javari, Negro and Paru-Jari basins (northern); and High-Madeira, low-Madeira and Tapajos basins (southern). Seasonality was normalized between 0 to 1 and arrow orientation indicates sub-basin location with northern (up arrow) and southern (down arrow). 77

Figure 4.10. Rayleight and aerosol scattering reflectance (ρ) computed by different aerosol optical depth (AOD) for various satellite sensors: Wide Field Imager (WFI), CBERS-4; Operational Land Imager (OLI), Landsat-8; Moderate Resolution Imaging Spectroradiometer (MODIS), Terra; Multispectral camera (MUX), CBERS-4; MultiSpectral Instrument (MSI), Sentinel-2. 78

Figure 4.11. Total water vapor transmittance (TH2O) simulated for various satellite sensors: (a) Wide Field Imager (WFI), CBERS-4; (b) Operational Land Imager (OLI), Landsat-8; (c) Moderate Resolution Imaging Spectroradiometer (MODIS), Terra; (d) Multispectral camera (MUX), CBERS-4; (e) MultiSpectral Instrument (MSI), Sentinel-2. 80

Figure 4.12. Total ozone transmittance (TO3) simulated for various satellite sensors: (a) Wide Field Imager (WFI), CBERS-4; (b) Operational Land Imager (OLI),

Landsat-8; (c) Moderate Resolution Imaging Spectroradiometer (MODIS), Terra; (d) Multispectral camera (MUX), CBERS-4; (e) MultiSpectral Instrument (MSI), Sentinel-2. 80

Figure 4.13. Cloud cover fraction (a, b) and aerosol optical depth (c, d) for July and August. Location of Landsat-8 scene grid is shown with path (vertical) and row (horizontal) information as one more reference for remote sensing users. Note the same cloud cover fraction but the distinct AOD condition between July and August. 81

Figure 4.14. Maximum and minimum months of (a, b) cloud cover and key atmospheric constituents: (c, d) aerosol optical depth, AOD; (e, f) total precipitable water, TPW; and (g, h) total columnar ozone, TOZ. Location of Landsat-8 scene grid is shown as one more reference for remote sensing users; see path (vertical) and row (horizontal) information. 86

Figure 5.1. Overview of study area and sample stations over four Amazon floodplain lakes: (a) Buá-Buá; (b) Mamirauá; (c) Panta-leão; and (d) Pirarara. 93

Figure 5.2. Average (solid line) and standard deviation (shadow-coloured) of water reflectance measured on four Amazon lakes: Buá-Buá (BUA), Mamirauá (MAM), Panta-Leão (PANTA) and Pirarara (PIRA). The square markers and error bars are Multi-Spectral Instrument (MSI) reflectance simulated (Rw,situ) and their standard deviation, respectively. 95

Figure 5.3. MODIS AOD products concurrently with MSI image on 12 August 2016: (a) MOD09 surface reflectance; (b) MAIAC AOD550 1 km; (c) MOD04 3 km Collection 6; and (d) MOD04 10 km Collection 6. 99

Figure 5.4. Example of water and forest endmembers selection at Mamirauá Lake. (a) Random points in the forest surface near to Mamirauá Lake. (b) Water and forest endmembers (Table 5.3). 105

Figure 5.5. Scatter plot of MAIAC AOD550 (y-axis) compared to AERONET AOD550 data (x-axis) from three sites in the Amazon region: Balbina, Belterra and Manaus-Embrapa. Solid blue and grey lines are the linear regression fits for Terra and Aqua, respectively. Red dashed lines are the MODIS standard expected error intervals ($\Delta AOD = \pm 0.05 \pm 0.15 \times AOD$) (REMER et al., 2005b). Text box:

Regression equation, correlation coefficient (R), match-ups (n), root mean square error (RMSE), mean ratio (AODMAIACAODAERONET), and EE is the number of retrievals falling within standard expected error. 108

Figure 5.6. Monthly average of aerosol optical depth (AOD) at 550 nm, water vapour content and cloud cover from MAIAC Terra (2000–2015) in Mamirauá region (see red-box in Figure 5.1). 110

Figure 5.7. Simulation of TOA reflectance based on month average AOD in August (biomass burning model) and average of water reflectance from four Amazon floodplain lakes. The table at the top right shows the percentage of atmospheric and surface contribution in TOA reflectance simulated for MSI VNIR bands.. 111

Figure 5.8. Comparison between MSI reflectance simulated from in-situ measurements, MSI TOA reflectance and MSI-corrected reflectance from three methods: 6SV model based on MAIAC product (a,b); ACOLITE (c,d); and Sen2Cor (e,f). The left column shows reflectance spectra from dark lakes (Buá-Buá and Mamirauá) and, the right column shows reflectance spectra from bright (Pirarara and Panta-Leão) lakes. 114

Figure 5.9. The mean ratio and RMSE for atmospheric correction methods from: dark lakes (a,b); and bright lakes (c,d). The left column shows the mean ratio (RsurRW,situ), with better cases being close to unity, and the right column shows the root mean square error (RMSE). Note that all mean ratio values higher than maximum bias accepted here are represented as 2. 116

Figure 5.10. Comparison between MSI TOA reflectance (grey), MSI-corrected reflectance from 6SV model (dark blue), and MSI-adjacency corrected reflectance (purple) and MSI reflectance simulated from in-situ measurements (light blue) from dark (a,c) and bright lakes (b,d). RMSE bars before (6SV) and after adjacency correction (6SV + adj. cor) applied to MSI image from 12 August 2016..... 118

LIST OF TABLES

Table 2.1. Atmosphere composition for U.S. standard atmosphere 1976. 7

Table 3.1. Over-Land AERONET sites used in this study. The ID number in parentheses is a reference to site location in Figure 1. 26

Table 3.2. Match-up analysis applied to various spatial (d) and temporal (t) window for Terra (a) and Aqua (b). First line: number of match-ups/correlation coefficient, second line: RMSE/Bias. The selected time-space threshold is presented in bold. 31

Table 3.3. Basic statistics of AERONET sites grouped according to major land cover type..... 33

Table 3.4. Land cover distribution around AERONET sites. 33

Table 3.5. Basic statistics of MAIAC retrievals from Terra (first line) and Aqua (second line) compared to AERONET measurements from mixed group. 44

Table 3.6. Temporal assessment of MAIAC products for seasons: DJF (December–February), MAM (March–May), JJA (June–August) and SON (September–November). For each season, first line is of Terra retrievals (shaded gray) and second line is of Aqua retrievals..... 51

Table 3.7. Long-term AERONET sites used in time series validation. 52

Table 4.1. Input parameters and their description of the simulation conditions. 64

Table 4.2. Quarterly averaged and standard deviation data of cloud cover fraction and key atmospheric constituents in the four Amazon regions. 74

Table 5.1. Spectral bands of MSI sensor on-board Sentinel-2 satellite. 97

Table 5.2. Input parameters of 6SV model for Sentinel MSI image..... 101

Table 5.3. Water and forest endmembers selected as input to LSU per lake. 106

LIST OF ABREVIATIONS

AERONET	AErosol RObotic NETwork
AOD	Aerosol optical depth
ATTO	Amazon Tall Tower Observatory
BFAST	Breaks For Additive Season and Trend
BRF	Bidirectional reflectance factor
CALIPSO	Cloud Aerosol-Lidar and Infrared Pathfinder Satellite Observations
CBERS	China-Brazil Earth Resources Satellite
CDOM	Coloured dissolved organic matter
Chl-a	Chlorophyll-a
CSR	Critical surface reflectance
DDV	Dense dark vegetation
EE	Expected error value
ENSO	El Niño–Southern Oscillation
EOS	Earth Observing System
GLC	Global Land Cover
IBGE	Brazilian Institute of Geography and Statistics
ITCZ	Intertropical convergence zone
LOWTRAN	Low Resolution Atmospheric Transmission Model
LSU	Linear Spectral Unmixing
MAIAC	Multi-Angle Implementation of Atmospheric Correction
MERIS	MEdium Resolution Imaging Spectrometer
MISR	Multiangle Imaging Spectroradiometer
MOD04	MODIS aerosol product
MODIS	Moderate Resolution Imaging Spectroradiometer
MODTRAN	Moderate Resolution Atmospheric Radiance and Transmittance Model
MSDR	Mamirauá Sustainable Development Reserve
MSI	Multispectral Instrument
NIR	Near infrared
OAC	Optically active component

OLI	Operational Land Imager
OMI	Ozone Monitoring Instrument
Q	Digital number
RSR	Relative Spectral Response
RT	Radiative transfer
SACZ	South Atlantic Convergence Zone
SALLJ	South America low-level jet
SASM	South American Summer Monsoon
SNR	Signal-Noise ratio
SRC	Spectral Regression Coefficient
SST	Sea surface temperature
TOA	Top-of-atmosphere
TPW	Total Precipitable Water
TRMM	Tropical Rainfall Measuring Mission
TSS	Total suspended solid
VNIR	Visible and Near-Infrared
VOCs	Volatile organic compounds
6SV	Vector version of Second Simulation of the Satellite Signal in the Solar Spectrum

LIST OF SIMBOLS

σ_{λ}^{abs}	Absorption coefficient of medium
ε	Aerosol type
AE, α	Ångström exponent
β	Ångström turbidity
P_r	Atmopsheric pressure at local
S_{λ}	Atmosphere spherical albedo
ρ_{λ}^{ATM}	Atmospheric intrinsic reflectance
P_{r_o}	Atmospheric pressure at sea level
d	Earth-Sun Distance
σ_{λ}^{ext}	Extinction coefficient of medium
d_s	infinitesimal path thickness
E	Irradiance
I_o	monochromatic beam
τ	Optical depth
$\Delta\delta_{qrt}$	Quarterly bias
L	Radiance
ρ, R	Reflectance
σ_{λ}^{sca}	Scattering coefficient of medium
$P_{\lambda}(\Theta)$	Scattering phase function
ω_{λ}	Single-scattering albedo
φ_0	Solar azimuth angle
θ_0	Solar Zenith Angle
T	Transmittance
φ_v	View azimuth angle
θ_v	View zenith angle
λ	Wavelength
W	Wind speed

CONTENTS

1 INTRODUCTION 1
1.1. Overview 1
1.2. Objective 3
1.3. Outline 4
2 THEORETICAL BACKGROUND 5
2.1. Earth's atmosphere and interaction with solar radiation 5
2.1.1. Atmosphere composition 5
2.1.2. Atmosphere attenuation: Scattering and absorption 9
2.1.3. Basic concepts of radiative transfer 13
2.1.4. Atmospheric constituents from space: multi-angle MODIS products 16
2.2. Optical remote sensing: radiometric conversion and atmospheric correction 18
3 VALIDATION OF MAIAC AOD RETRIEVALS USING GROUND-TRUTH AERONET DATA OVER SOUTH AMERICA 23
3.1. Introduction 23
3.2. Data Description 25
3.2.1. AERONET data 25
3.2.2. MAIAC 27
3.3. Validation approach 28
3.3.1. General 28
3.3.2. Spatio-temporal window 29
3.4. Land cover around AERONET sites 31
3.5. Statistical analysis 34
3.6. Results and Discussion 36
3.6.1. Overall MAIAC and AERONET AOD550 comparison 36
3.6.2. MAIAC and AERONET AOD550 comparison over land cover types 39
3.6.3. Impacts of AOD magnitude 44
3.6.4. Impacts of seasonal variability on AOD retrievals 46
3.6.5. Time series validation 51

3.7. Conclusion 53
4 SEASONAL PATTERN OF CLOUD COVER AND ATMOSPHERIC CONSTITUENTS AND ITS IMPLICATIONS FOR OPTICAL REMOTE SENSING 55
4.1. Introdution 55
4.2. Background 56
4.3. Data and methods 59
4.3.1. MAIAC 59
4.3.2. MOD08 ozone 61
4.3.3. Spatiotemporal Analysis 62
4.3.4. Sensitivity analysis to atmospheric constituents: Transmittance and Scattering effects 63
4.4. Results 64
4.4.1. Comparisons of MAIAC AOD and TPW at two AERONET sites 64
4.4.2. An overview of atmospheric constituents 66
4.4.3. Regional Analysis 69
4.4.4. Sub-basin analysis 74
4.4.5. Implication of key atmospheric constituents on optical remote sensing 77
4.5. Discussion 81
4.6. Summary and conclusion 87
5 ASSESSMENT OF ATMOSPHERIC CORRECTION METHODS FOR SENTINEL-2 MSI IMAGES APPLIED TO AMAZON FLOODPLAIN LAKES 89
5.1. Introduction 89
5.2. Materials 92
5.2.1. Site Description and Field Data 92
5.2.2. MSI/Sentinel-2 Data 95
5.2.3. MAIAC Atmospheric Data 97
5.3. Methods 99
5.3.1. 6SV Model + MAIAC Atmospheric Products 99
5.3.2. ACOLITE Algorithm 101

5.3.3. Sen2Cor Algorithm 102
5.3.4. Adjacency Effect Correction 103
5.4. Results and Discussion 106
5.4.1. Evaluation of MAIAC AOD550 106
5.4.2. Background of Atmospheric Constituents 108
5.4.3. TOA Simulation Analysis 110
5.4.4. Inter-Comparison of Atmospheric Correction Methods 112
5.4.5. Adjacency Effect Correction 116
5.5. Conclusions 118
6 FINAL CONSIDERATIONS 121
7 REFERENCES 125

1 INTRODUCTION

1.1. Overview

Earth observation satellites allow systematic surface-atmospheric monitoring. The new generation of orbital sensors, e.g., Multispectral Instrument (MSI)/Sentinel-2 and Operational Land Imager (OLI)/Landsat-8, offers high-quality data to continuous assessment of long-term changes on both local and global scales (BERGER et al., 2012; ROY et al., 2014). The direct and indirect radiative effects of aerosols and molecular gases need be accounted to retrieve reliable surface reflectance from remote sensing data (OUAIDRARI; VERMOTE, 1999; CLAVERIE et al., 2015; VERMOTE et al., 2016). In general, atmospheric attenuation includes absorption and scattering processes caused by air molecules and aerosol in the atmosphere. To minimize these effects, several atmospheric correction methods have been proposed for land and ocean, such as empirical image-based techniques (e.g. dark object) and radiative transfer (RT) models, such as Moderate Resolution Atmospheric Radiance and Transmittance Model (MODTRAN) (BERK et al., 2005), and vector version of Second Simulation of the Satellite Signal in the Solar Spectrum (6SV) (VERMOTE et al., 1997b).

Although RT models are sufficiently robust to solve the radiative transfer problem, data on atmospheric properties are key input and might limit routine atmospheric correction applications (VERMOTE et al., 2002). Amongst the input parameters, aerosols are the most complex constituent due to its short live in the lower troposphere and high variability of microphysical properties and emission sources (LENOBLE, 2013). Since part of satellite sensors was not designed with spectral bands suitable for atmospheric properties retrievals, alternative data sources are needed and mostly based on ground-based measurements or satellite atmospheric products (JU et al., 2012; NAZEER et al., 2014).

AERONET (AErosol RObotic NETwork) is a global network program developed by NASA for ground-based aerosol monitoring (HOLBEN et al., 1998). The direct sun and diffuse sky radiance measured by sun photometers are used to obtain the aerosol optical depth (AOD) within the 440 - 1020 nm spectral range. However, while such ground-

based AERONET measurements are limited to local observations, satellite products present viable means for large-scale aerosol monitoring. In this context, products developed based on the Moderate Resolution Imaging Spectroradiometer (MODIS) provide historical dataset of aerosol product (MOD04) based on "Dark Target" and "Deep Blue" algorithms (REMER et al., 2005; SAYER et al., 2013). Recently, a new multi-angle MODIS algorithm, named Multi-Angle Implementation of Atmospheric Correction (MAIAC), has been developed and contributes to scientific advances in aerosol retrievals at high 1 km resolution (LYAPUSTIN et al., 2011). MAIAC uses the time series approach and image processing to derive surface reflectance and atmospheric products, such as AOD, water vapor and cloud mask. Therefore, this algorithm provides useful dataset to understand the long-term distribution of aerosol burden in the South America.

In the Amazon region, satellite remote sensing faces seasonal variability of key atmospheric constituents (aerosol, water vapor and ozone content) and cloudiness regimes as response of the regional climatology (NAGY et al., 2016). The high amount of water vapor and biomass burning season are features of the Amazon atmosphere (ANDREAE et al., 2015). In the Southern region, wildfires and human-induced fires increase the aerosol burden in the dry season (ARAGÃO et al., 2007), and tropospheric ozone changes due to net radiation and ozone precursors in the same period (ZIEMKE et al., 2009). In the austral summer, high water vapor abundance contributes to the water recycling into atmosphere and so induced cloudiness regimes, especially with the beginning of rainy season (NOBRE et al., 2009).

In view of these topics, the dynamic of atmospheric constituents has a clear relevance for quantitative applications of satellite data. Particularly, satellite aerosol products are an important source of information for atmospheric studies and remote sensing applications, however, they require extensive validation to assess the quality of retrievals. Additionally, due to the complexity of atmospheric features in the Amazon ecosystem, evaluation of seasonal pattern of atmospheric constituents, and subsequent, assessment of atmospheric correction over Amazon floodplain lakes contributes to future remote sensing application to inland water studies in this tropical region.

1.2. Objective

The motivation of this research was understand the limitation of atmospheric correction and optimal method to retrieve surface water reflectance using satellite image. An accurate atmospheric correction requires input of atmospheric information, which is often scarce in the South America, especially in the Amazon region. This has led to evaluation of new multi-angle MODIS data as innovative alternative to comprehend the seasonal dynamic of atmospheric constituents in Amazon region and to fill the required atmospheric information for correction of satellite image, such as MSI/Sentinel-2. Due to the intrinsic multi-disciplinary nature of this work, we can clearly state three main objectives: (i) the validation of MAIAC AOD retrievals in South America (Chapter 3); (ii) the application of MAIAC/MODIS dataset to understand the annual and intra-annual pattern of cloud cover and atmospheric constituents in the Amazon basin (Chapter 4); and finally, (iii) the assessment of atmospheric correction methods for MSI/Sentinel-2 image over Amazon floodplain lakes (Chapter 5). Based on these objectives, the following research questions are addressed in this dissertation:

1. How adequate are MAIAC AOD retrievals in comparison to ground-truth AERONET measurements across South America? Is the quality feasible for aerosol monitoring? (Chapter 3)

2. *What is the main feature of cloud cover and atmospheric constituents in the Amazon basin? What are their implications for the remote sensing monitoring of Amazon ecosystem?* (Chapter 4)

3. *Are the atmospheric correction methods feasible to estimate the surface water reflectance in Amazon floodplain lakes? What are the challenges for atmospheric correction in region?* (Chapter 5)

1.3. Outline

This paper-based master thesis is organized as follows:

Chapter 1 introduces the topics of atmospheric attenuation caused by aerosol, water vapor and ozone, and atmospheric correction of satellite image with their relevance to remote sensing and Earth surface monitoring.

Chapter 2 presents the theoretical background with topics including atmosphere composition, structure and attenuation processes of solar radiation. This chapter also describes the radiative transfer theory, radiometric conversion and atmospheric correction of satellite images.

Chapter 3 describes the validation analysis of the MAIAC AOD product for MODIS Terra and Aqua at 19 AERONET sites over South America. The results are also stratified by land cover type to examine the influence of this on retrieval performance.[*1]

Chapter 4 presents the seasonal pattern of cloud cover and key atmospheric constituents over Amazon basin. This analysis is related to implications for optical remote sensing and addresses the most critical regions and periods for surface observation by satellite images.[*2]

Chapter 5 assesses three atmospheric correction models for new MSI sensor on board of Sentinel-2A platform in the Amazon floodplain lakes. The results of atmospheric correction are compared to simultaneous in-situ measurements. In addition, linear spectral model is used to adjacency correction of forest neighbor over water reflectance.[*3]

Chapter 6 summarizes the main findings of this study and synthesizes them with respect to optical remote sensing and atmospheric correction.

[*1] This chapter is an adapted version of the paper: MARTINS, V.S.; LYAPUSTIN, A; CARVALHO, L.A.S.; BARBOSA, C.C.F.; NOVO, E.M.L.M.. Validation of high-resolution MAIAC aerosol product over South America. **Journal Geophysical Research: Atmospheres**. (Under review).

[*2] This chapter is an adapted version of the paper: MARTINS et al. (2017). Seasonal pattern of atmosphere constituents and their implications on optical remote sensing over the Amazon.

[*3] This chapter is an adapted version of the paper: MARTINS, V.S.; BARBOSA, C.C.F.; CARVALHO, L. A.S.; JORGE, D.S.F.; LOBO, F.D.L.; and NOVO, E.M.L.M.. Assessment of Atmospheric Correction Methods for Sentinel-2 MSI Images Applied to Amazon Floodplain Lakes. **Remote Sensing**, *9*(4), 322. 2017. (Published).

2 THEORETICAL BACKGROUND

2.1. Earth's atmosphere and interaction with solar radiation

This chapter outlines the vertical structure and constitution of Earth's atmosphere, absorption and scattering of solar radiation, and satellite atmospheric product from multi-angle MODIS data. Additionally, provides principles of energy transfer in the atmosphere, such as Beer-Lambert's law.

2.1.1. Atmosphere composition

The atmosphere is a layer composed by a mixture of various gases and suspended liquid and solid particles around the Earth. Due to variation in temperature with height, the atmosphere is conventionally divided in layers (ANDREWS, 2010): Troposphere, stratosphere, mesosphere, thermosphere and exosphere (**Figure 2.1**). The vertical structure of atmosphere defines distinct distribution and concentration of constituents; density and pressure decrease continuously from terrestrial surface to the top-of-atmosphere. Generally, aerosols and water vapor are concentrated into tropospheric layer (up to 20 km) and temperature profile decreases with height (WALLACE; HOBBS, 2006). In the stratosphere layer (~20 to 50 km), ozone content is the most dominant gas and contributes to rise the temperature with height due to the absorption of solar radiation (ROYAL SOCIETY, 2007). The mesosphere (thermosphere) presents the temperature decreasing (rising) with altitude.

Figure 2.1. Variation of the atmospheric temperature (Kevin) and pressure (hPa) in the 100 km of atmosphere.

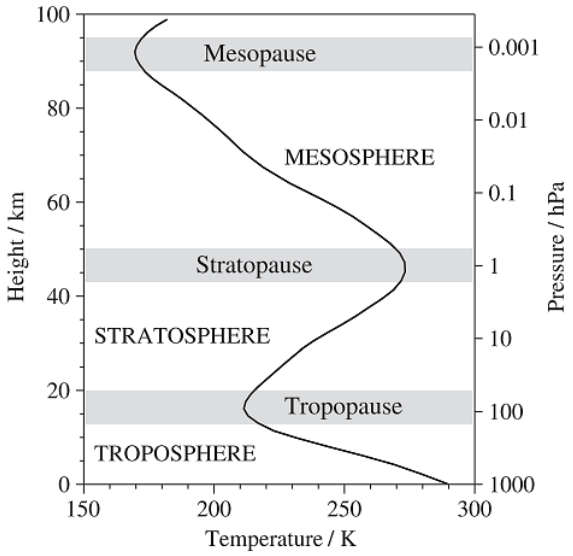

Source: Andrews (2010).

Atmospheric composition and concentration is distinct geographically due to terrestrial processes, elevation and climate season (IQBAL, 2012). In reference, the standard U.S. 1976 atmosphere composition includes nitrogen (78 %), oxygen (21%) and other gases (1%), such as carbon dioxide, ozone and argon (**Table 2.1**). Although we understand the importance of standard composition as an atmospheric reference, regional features need to be account for atmospheric transfer models. For example, amongst those gases, water vapor is highly variable in both space and time because the moisture transport and surface-atmospheric feedback (ENT et al., 2010). For remote sensing applications, troposphere layer has a significant influence in radiative transfer models, due to abundant amount of active gases distorting the propagation of electromagnetic radiation.

Table 2.1. Atmosphere composition for U.S. standard atmosphere 1976.

Constituent gas	Content (% by volume)
Nitrogen (N_2)	78.084
Oxygen (O_2)	20.948
Argon (Ar)	0.934
Carbon dioxide (CO_2)	0.333
Neon (Ne)	18.18×10^{-4}
Helium (He)	5.24×10^{-4}
Krypton (Kr)	1.14×10^{-4}
Xenon (Xe)	0.089×10^{-4}
Hydrogen (H_2)	0.5×10^{-4}
Methane (CH_4)	1.5×10^{-4}
Nitrous oxide (N_2O)	0.27×10^{-4}
Ozone (O_3)	$0\text{-}12 \times 10^{-4}$
Sulfur dioxide (SO_2)	0.01×10^{-5}
Nitrogen dioxide (NO_2)	0.01×10^{-5}
Ammonia (NH_3)	0.04×10^{-5}
Coarbon monoxide (CO)	0.19×10^{-4}
Water vapor (H_2O)	$0\text{-}0.04 \times 10^{-4}$

Source: Iqbal (1983).

In addition to air constituents, aerosols are suspended particles in the atmosphere with wide variety of shape, size and chemical composition (ANDREAE, 2007; LENOBLE et al., 2013). Aerosol sources range from natural and anthropogenic emissions, such as wildfire, desert dust, volcanoes, sea salt and biogenic compounds, biomass burning, fossil-fuel combustion and industrial pollution (**Figure 2.2**). Since most aerosols are emitted from the Earth's surface, the higher concentrations are observed in the lower layers of the troposphere and the physical characteristics depend on the aerosol source and transport (LENOBLE, 2013). Understanding the direct radiative effect of aerosols is still a challenge for scientific community (IPCC, 2007*)*, although their influence on radiative forces for climate system is already unquestionable. In addition to climate effects, the aerosol changes the air quality (MONKS et al., 2009), reduces the visibility and air pollution causes respiratory diseases in megacities (BELL et al., 2006).

Figure 2.2. Sources of natural and human-induced aerosol particles into atmosphere.

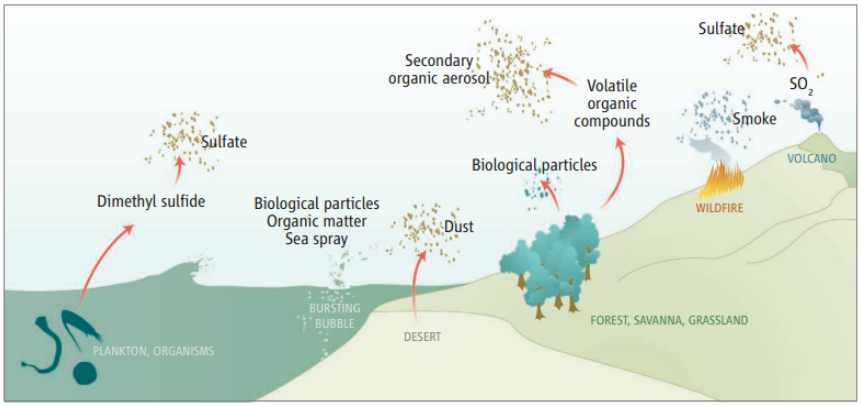

Source: Andreae (2007).

Artaxo et al. (2013) reported the basic processes that regulates the Amazon atmospheric composition and found that main aerosol particles in the region are natural biogenic aerosols and biomass burning emissions from cropland and pasture areas. In absence of fire emission, the secondary organic aerosol plays significant role as biogenic nuclei of cloud in the Amazon atmosphere (PÖSCHL et al., 2010; WANG et al., 2016).

In this context, radiative transfer model offers an explicit physical description of transmission function and scattering properties to integrate the columnar effects caused mostly by air molecules, water vapor, and aerosols (MISHCHENKO, 2008). Therefore, the vertical distribution of particles and gases in the atmosphere (**Figure 2.3**) is important during the development of physical-based models. The mathematical solution for propagation of solar radiation through atmosphere requires an introduction of radiative transfer concepts and description of main physical-optical processes: absorption and scattering radiation (LIOU, 2002).

Figure 2.3. Basic scheme with vertical distribution of atmospheric constituents.

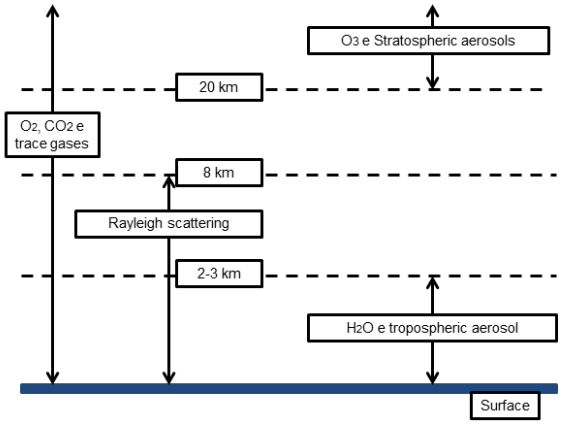

Source: Vermote et al. (1997a).

2.1.2. Atmosphere attenuation: Scattering and absorption

Optically active constituents in the earth's atmosphere are responsible for spectral attenuation of solar radiation, which is called atmospheric attenuation or extinction (LIOU, 2002). The loss of energy of a photon by absorption or change in its original direction of propagation due to scattering correspond to the attenuation or extinction process. Thus, propagation of solar radiation through atmosphere undergoes physical-optical attenuation caused by atmospheric constituents. **Figure 2.4** shows the attenuation of solar radiation caused by absorbing gases (IQBAL, 1983). The distribution of terrestrial solar incident radiation varies spectrally due to strong absorption features of oxygen (O_2), ozone (O_3), carbon dioxide (CO_2) and water vapor (H_2O). Therefore, it is observed that absorption features are spectrally dependent of each constituent (GAO et al., 2009). The atmospheric absorption is defined as the conversion of electromagnetic energy to another energy condition, usually, as thermal energy (LIOU, 2002). Thus, original photons interact with matter inducing molecular vibration, rotation or orbital transition of electrons. The main absorbing constituents are the O_2, O_3, CO_2 and H_2O. For example, water vapor has strong influence on absorption of solar radiation in near infra-red (NIR) bands and less impacts on visible wavelengths (GAO et al., 2009).

Figure 2.4. Extraterrestrial and terrestrial solar radiation from 0.25 to 3.0 µm.

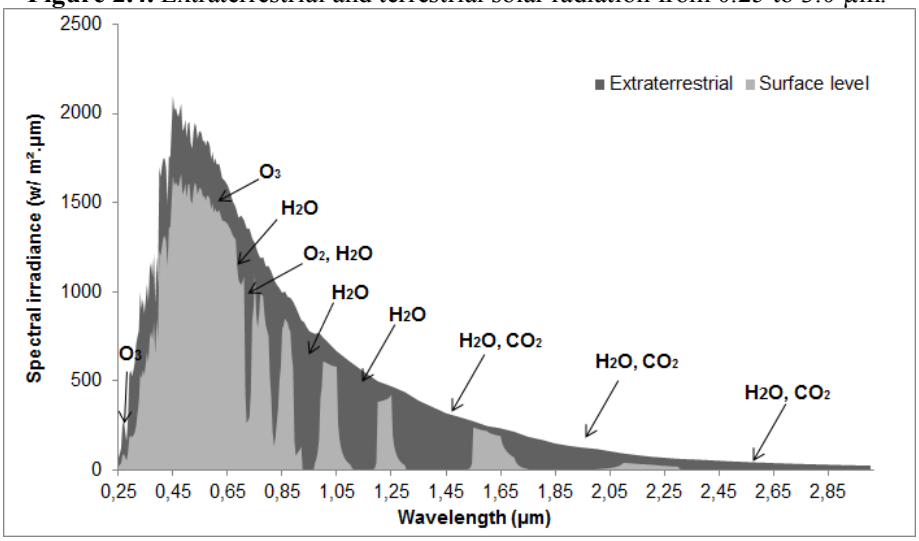

Source: Adapted from Iqbal (1983).

Understanding absorption features is useful to specify or design an optical sensor in order to locate the spectral sensor bands in region under weak absorption effects, so called "atmospheric window". Additionally, the knownledge of absorption regions is important to atmospheric studies, because these regions are used to estimate concentration of specific constituents. GAO et al. (2009) simulated the transmittance of key atmospheric constituents between 0.4 and 2.5 µm (**Figure 2.5**). Ozone absorption bands occur mostly in ultraviolet region (0.22 to 0.35 µm, not shown) and in visible wavelengths (~ 0.4 to 0.7 µm) with an important absorption feature between 0.55 and 0.65 µm (Chappuis band) (ROYAL SOCIETY, 2008). In contrast, water vapor and carbon dioxide have several strong absorption bands in infrared region (0.94, 1.14, 1.38 and 1.9 µm). These constituent features are important to radiative transfer models, in especial, for atmospheric correction. Earth observation satellites provides advanced and novel capabilities to monitor seasonal changes of these absorber gases, which could be used to parametrize the atmospheric correction models.

Figure 2.5. Simulated transmittance of atmospheric water vapor (H_2O), carbon dioxide (CO_2), ozone (O_3), nitrous oxide (N_2O), carbon monoxide (CO), methane (CH_4), oxygen (O_2), and nitrogen dioxide (NO_2).

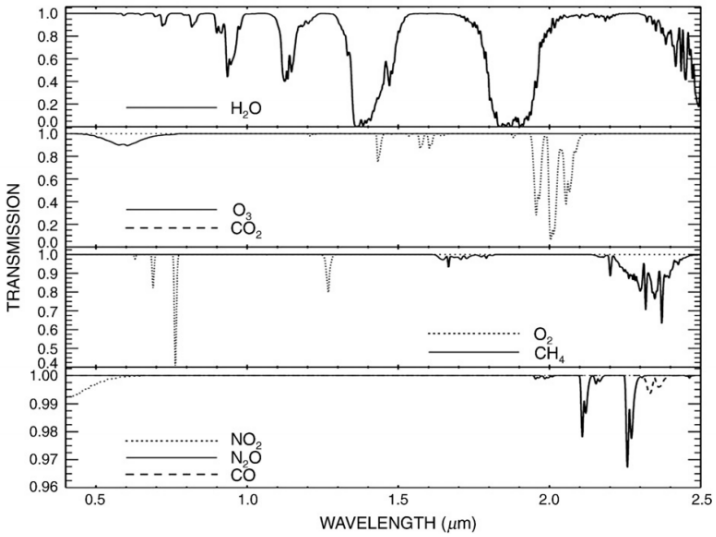

Source: Gao et al. (2009).

Scattering is an optical-physical process associated with photon-matter interaction with changes of direction along photon's trajectory. The shape and size of atmospheric constituents range from air molecules (~10^{-4} μm) to aerosols (~1 μm) and water drops (~10 μm) (IQBAL, 1983). The scattering processes are referred to Rayleigh scattering or Lorenz–Mie scattering according to size parameter of each particle. The size parameter is a ratio of the particle circumference to the incident wavelength ($sz = 2\pi r/\lambda$, where r is the particle radius and λ is wavelength). The molecular scattering, or Rayleigh, occurs when size parameter is smaller than that incident radiation wavelength ($sz < 0.1\ \lambda$), with extinction coefficient of ~ λ^{-4}. Thus, Rayleigh scattering coefficient decreases as wavelength increases, with high scattering in short wavelengths. The classical example is the blue sky as result of high scattering of blue wavelengths (ANDREWS, 2010). In turn, Lorenz-Mie scattering occurs when size parameter is higher than incident wavelength ($sz > \lambda$) (Figure 2.6), and it intensity is less wavelength dependent than Rayleigh (e.g. λ^{-2} for water vapor) and primarily dependent on particle size (IQBAL, 1983). Therefore, while the absorption processes are most wavelength dependent, scattering processes affect in broad spectral region with exponential decay

from shorter to longer wavelengths. While light is scattered equally in the forward and backward direction for small particles, as the particle increases in size more light tends to scatter in the forward direction (Figure 2.6).

Figure 2.6. Scattering distribution of solar radiation according to size parameter.

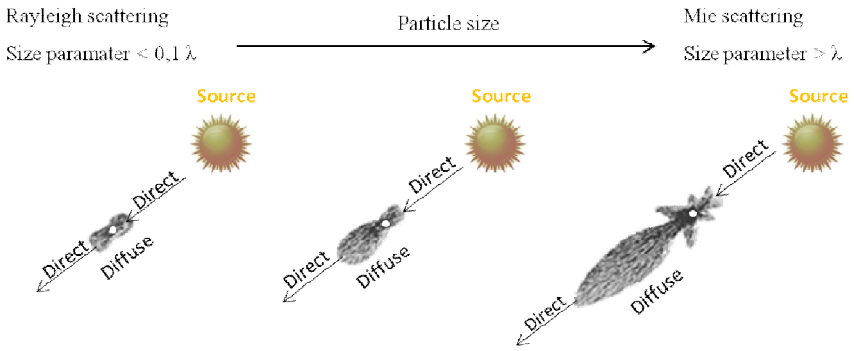

Source: Adapted from Iqbal (1983).

The physical description of scattering and absorption function allows compute the radiative transfer coefficient to support atmospheric correction of satellite images (KONDRATYEV et al, 1992). For example, 6SV is able to quantify the atmospheric transmittances and scattering effects based on the Successive Orders of Scattering approximation (SOS) approach that computes those effects on radiation photons considering atmosphere layers (VERMOTE, 1997a). **Figure 2.7** shows the atmospheric intrinsic reflectance (additive effect with upward arrow) caused by molecular gases and aerosol scattering, and absorption effect (downward arrow) due to ozone and water vapor in TM/Landsat 5 spectral bands. Is it clear from **Figure 2.7** that absorption effects of ozone and water vapor are presented by fraction attenuated in percentage and molecular gases and aerosols scattering are showed in absolute reflectance values. Ozone is more optically active in visible bands (transmittance from 5.2 to 13.45% in green band) and water vapor attenuation is predominant in infrared bands (3.5 to 16%). IQBAL (1983) showed that ozone effects is predominant in ultraviolet, with absorption coefficient reducing from 38 cm^{-1} at 290 nm (ultraviolet) to 0.009 cm^{-1} at 470 nm (blue). Further, author reported that ozone is quite stable spatially and varies amongst year periods and latitudes, while water vapor and aerosol are most variable constituents in atmosphere.

Figure 2.7. Atmospheric attenuation of ozone and water vapor (%) and scattering reflectance of Rayleigh and aerosol applied to TM/ Landsat 5.

TM spectral bands	Ozone (cm/atm) 0,247 - 0,480	Water vapor (g/cm²) 0,5 - 4,1	Rayleigh 1013 mb	Aerosol (Continental) Vis:10-60 km
ρ1 (0,45 - 0,52 µm)	↘ 1,5 a 2,9%	----	↗ 0,064 a 0,08	↗ 0,007 a 0,048
ρ2 (0,50 - 0,60 µm)	↘ 5,2 a 13,45	↘ 0,5 a 3%	↗ 0,032 a 0,04	↗ 0,006 a 0,04
ρ3 (0,63 - 0,69 µm)	↘ 3,1 a 7,9%	↘ 0,5 a 3%	↗ 0,018 a 0,02	↗ 0,005 a 0,034
ρ4 (0,76 - 0,90 µm)	----	↘ 3,5 a 14%	↗ 0,007 a 0,009	↗ 0,003 a 0,023
ρ5 (1,55 - 1,75 µm)	----	↘ 5 a 16%	↗ 0 a 0,001	↗ 0,001 a 0,007
ρ7 (2,08 - 2,35 µm)	----	↘ 2,5 a 13%	----	↗ 0,001 a 0,004

Source: Adapted from Vermote et al. (1999).

2.1.3. Basic concepts of radiative transfer

Radiative transfer theory is a conceptual and quantitative solution for computing the transfer of radiation energy through medium, including absorption, scattering and emission (LIOU, 2002). A simple way to describe this complex process is use Beer-Lambert-Boguer Law to represents beam attenuation. Here, radiant flux density ($W.m^{-2}$), is called intensity I_o, without definition of its directional distribution. Note that radiant flux density actually is known as irradiance, but we adopt the I_o for simplicity. Consider a monochromatic beam of intensity $I_{o,\lambda}$ moving through a homogenous medium in the direction (Ω), see **Figure 2.8**. The scattering and absorption processes attenuate an intensity $I_{o,\lambda} + dI_\lambda$ (Ω, d_s) inside the infinitesimal thickness (d_s) between the starting position (s_1) and the ending position (s_2). This homogeneous medium contains radiative active gas. According to the radiative transfer theory, dI_λ (Ω, d_s) is defined by Equation 2.1 (LIOU, 2002):

$$dI_\lambda(\Omega, d_s) = -I_{o,\lambda}(\Omega, s_1) \times \sigma_\lambda^{ext} \times d_s \qquad (2.1)$$

Where, σ_e is the extinction coefficient of medium (m^{-1}). Therefore, the reduction of the intensity is a function of optical properties and pathlength in the medium, for example, columnar atmosphere. The cumulative extinction of σ_λ^{ext} is generally defined by sum of

the scattering coefficient (σ_λ^{sca}) and absorption coefficient (σ_λ^{abs}), and the fractional contribution of scattering to the total extinction is given by the single-scattering albedo (ω_λ) (LIOU, 2002):

$$\sigma_\lambda^{ext} = \sigma_\lambda^{sca} + \sigma_\lambda^{abs} \tag{2.2}$$

$$\omega_\lambda = \sigma_\lambda^{sca}/\sigma_\lambda^{ext} \tag{2.3}$$

If the medium emits energy, an extra term must be added to the right hand side of equation (2.1), but it is not considered here.

Figure 2.8. Definition of extinction in homogeneous medium.

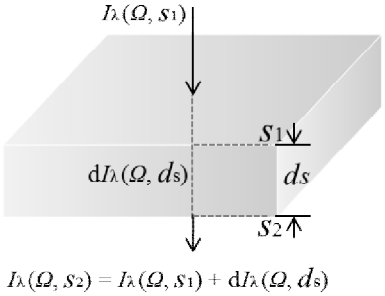

For a finite-thickness layer, the integration of Equation 2.1 between s_1 and s_2 position yields known as *Beer–Lambert law* (Equation 2.4):

$$I_\lambda(s) = I_{o,\lambda} \times e^{-\tau_\lambda^{ext}} \tag{2.4}$$

Where, the total optical depth (τ_λ^{ext}) is expressed by integral form of extinction coefficient in the trajectory path (s) (Equation 2.5) (IQBAL, 1983):

$$\tau_\lambda^{ext} = \int_{s_1}^{s_2} \sigma_\lambda^{ext}(s) \times d_s \tag{2.5}$$

In the atmosphere, the path (or distance) of beam is actually dependent of relative zenith direction along a vertical path of the atmosphere (d_z). The solar zenital angle (θ_0) is

defined between perpendicular at parallel plane and solar beam direction, where both d_s e d_z are related to Equation 2.6 (IQBAL, 1983):

$$d_s = \frac{d_z}{\cos\theta_0} \tag{2.6}$$

Consider the relative path in Equation 2.4, we can rewrite the Equation 2.7 to get:

$$I_\lambda(s) = I_{o,\lambda} \times e^{-\tau_\lambda^{ext} \times m_r} \tag{2.7}$$

Where m_r is optical relative mass, $m_r = \sec(\theta_0)$. This approximation using $\sec(\theta_0)$ has an error lower than 0.25% when $\theta_0 \leq 60°$ with homogenous atmosphere (IQBAL, 1983). Since atmosphere density varies according to regions and constituents types, KASTEN (1965) developed a model of m_r as function of atmospheric pressure (P) and θ_z applied to homogeneous atmosphere up to 8 km of altitude (Equation 2.8).

$$m_r = \frac{P_r}{P_{r_o}} \times \left[\frac{1}{\cos\theta_0 + 0{,}15 \times (93{,}885 - \theta_0)^{-1{,}253}}\right] \tag{2.8}$$

Where, P_r is the atmopsheric pressure at local (hPa), P_{r_o} is the atmospheric pressure at sea level (1032 hPa). The total optical depth τe is a sum of optical depth from each atmospheric constituent, such as molecular components, aerosols and water vapor. Thus, τ_λ^{ext} describes a potential attenuation of those constituents as Equation 2.9:

$$\tau_\lambda^{ext} = \tau_\lambda^{aer} + \tau_\lambda^{ray} + \tau_\lambda^{O_3} + \tau_\lambda^{H_2O} \ldots + \tau_\lambda^{i} \tag{1.9}$$

Where, the τ_λ^{aer}, τ_λ^{ray}, $\tau_\lambda^{O_3}$, $\tau_\lambda^{H_2O}$ and τ_λ^{i} are optical depth from aerosol, air molecular, ozone, water vapor, and other constituents, respectively. BODHAINE et al. (1999) presented several models to estimate the molecular optical depth. In this context, the model of τ_r is provided as function of wavelength and atmospheric pressure (HANSEN and TRAVIS, 1974):

$$\tau^{ray}(\lambda, P_r) = \frac{P_r}{P_{r_o}} \times \left[0{,}008569 \times \lambda^{-4} \times \left(1 + 0{,}0113\,\lambda^{-2} \times 0{,}00013 \times \lambda^{-4}\right)\right] \quad (2.10)$$

Where, λ is the wavelength in μm. Since the other constituents are most variable, such as aerosol and water vapor, local measurements using solar photometers are required to estimate their optical depth. The atmospheric transmittance (T) is defined as the attenuation factor that a beam of radiation suffers as it crosses the atmosphere. Thus, transmittance is expressed by (IQBAL, 1983):

$$T_\lambda = \frac{I_\lambda(s)}{I_{o,\lambda}} = e^{-\tau_\lambda^{ext} \times m_r} \quad (2.11)$$

In general, Rayleigh optical depth is relatively simple to estimate using atmospheric pressure. In contrast, aerosol effects and distribution are more complicate due to high variability of aerosol properties and complex ensemble in environmental. As mentioned, sun photometers are a feasible option to derive AOD at specific spectral regions. ÅNGSTRÖM(1929) proposed an empirical approximation to describe spectral dependence of aerosol optical depth:

$$\tau(\lambda) = \beta(\lambda)^{-\alpha} \quad (2.12)$$

Where, β is the coefficient of Ångström turbidity, α is the Ångström exponent. The α and β coefficients are also used to relate particle size and atmospheric turbidity (SCHUSTER et al., 2006). The typical values of α are 0.5 and 2.5, with natural emissions are around 1.3 ± 0.5. The interpretation of Ångstrom exponent suggests particle-size, where low α represents particles with high diameter (desert particles) and high α is mostly associated to fine-mode particles (ECK, 1999).

2.1.4. Atmospheric constituents from space: multi-angle MODIS products

Earth's atmosphere presents a wide variety of physical processes that provide climate services and change weather conditions (WALLACE; HOBBS, 2006). Satellite-based remote sensing measurements allow systematic retrieval of atmospheric constituents,

such as aerosol, water vapor and ozone content, on both local and global scales (KING et al., 2003). Over the last decade, satellite sensors have used to investigate the atmosphere properties, such as the MODIS, the Multiangle Imaging Spectroradiometer (MISR), the Ozone Monitoring Instrument (OMI), and the Cloud Aerosol-Lidar and Infrared Pathfinder Satellite Observations (CALIPSO) instrument (KAUFMAN et al., 1997b; MARTONCHIK et al., 1998). Particularly, Earth Observing System (EOS) provide a rich data source to the Earth science studies with MODIS sensor on board of the Terra (launched on December 1999) and Aqua (launched on May 2002) satellites. In MODIS Atmosphere Collection, the "Dark Target" algorithm (KAUFMAN et al., 1997b) complemented by the "Deep Blue" algorithms (HSU et al., 2004) provides AOD retrieval over dark and bright surfaces. The Dark Target approach uses typical dark surfaces, such as dense dark vegetation (DDV), to decouple aerosol and surface contributions. Since the aerosol scattering is almost insignificant in the SWIR region, the empirical relationships developed over vegetated surfaces are used to estimate the surface reflectance at 0.47 μm and at 0.66 μm from the measurements at 2.1 μm ($\rho_{0.47\ \mu m} = 0.25\ \rho_{2.1\ \mu m}$ and $\rho_{0.66\ \mu m} = 0.5\ \rho_{2.1\ \mu m}$) (KAUFMAN *et al.*, 1997a; REMER *et al.*, 2005). Although the surface reflectance parameterization was modified by LEVY *et al.* (2007b), this approach has some limitations over arid regions with bright surfaces, relatively sparse or no vegetation (GILLINGHAM et al., 2012). The continuous efforts have been made to enhance quality of atmospheric retrievals from MODIS data. In this context, MAIAC is a new MODIS algorithm developed to derive surface bidirectional reflectance factor (BRF) and a suite of atmospheric products at high 1 km resolution (LYASPUTIN et al., 2011). The atmospheric products include internal cloud mask and snow detection, aerosol optical depth at 0.47 and 0.55 μm, fine mode fraction and column water vapor based on near infrared (NIR) bands. This algorithm integrates the time series analysis and advanced pixel- and image-based approach processing over both dark and bright surfaces and it has an internal cloud mask and snow detection. The basic scheme of the MAIAC cloud-mask algorithm is a background information of the clear sky image as a reference to dynamically detecting the spectral variability over the accumulate MODIS measurements based on covariance analysis (LYASPUTIN et al., 2008). In addition to AOD retrievals and cloud mask,

MAIAC applies three MODIS near-IR bands (0.905 μm, 0.936 μm, 940 μm) to derive column water vapor, or total precipitable water (TPW), based on two-channel ratio algorithm with version modified from GAO and KAUFMAN (2003). These atmospheric products improve our ability in understand the seasonal patterns of atmospheric constituents and support as auxiliary data for atmospheric correction. In next section, we present principles of radiometric conversion and atmospheric correction required to spectral surface reflectance retrievals from remote sensing data.

2.2. Optical remote sensing: radiometric conversion and atmospheric correction

In general, satellite remote sensing consists of a data acquisition system involving sensor, platform, and ground receiving stations (acquire, archive, and process data) (JENSEN, 2009). The remote sensing system provides systematic measurements of reflected radiation from Earth-atmosphere system. To achieve consistent physical measurements, radiometric calibration is necessary to convert the sensor signal (or digital numbers) to an absolute scale of physical quantities, such as radiance or reflectance at top-of-atmosphere (CHANDER et al., 2009). Calibration procedures include three stages: Pre-flight, In-flight and Post-launch calibration. In the pre-flight calibration, it is performed the Relative Spectral Response (RSR) characterization, the regression of radiance and electronic signal in lab, evaluation of spectral uniformity of detectors and computation of signal-noise ratio (SNR) (BARSI, 2011; IRONS et al., 2012). The post-launch calibration characterizes the sensor degradation and changes on radiometric sensitivity, and can be conducted using intern lamps and diffuse panels on in-flight calibration (IRONS et al., 2012; REN et al., 2014), cross-calibration between satellite sensors (HELDER et al., 2013; PAHLEVAN et al., 2014), and vicarious calibration using ground-measurements (CZAPLA-MYERS et al., 2015).

The radiometric conversion of digital number (ND) to spectral radiance at top-of-atmosphere (L^{TOA}) is a fundamental procedure to produce a common radiometric scale amongst spectral bands. The digital number values (Q^{cal}) are scaled according to radiometric resolution of sensor (e.g. Q^{cal} = 255 (2^8 bits) for TM/Landsat-5). The conversion of Q^{cal} to L_λ requires vicarious calibration coefficient with maximum (L_λ^{max})

and minimum (L_λ^{min}) spectral radiance correspondent to superior (Q^{calmax}) and inferior (Q^{calmin}) limits of digital numbers. Equation 2.13 presents the conversion of Q^{cal} to L_λ in satellite images (CHANDER et al, 2009).

$$L_\lambda^{TOA} = \left(\frac{L_\lambda^{max} - L_\lambda^{min}}{Q^{calmax} - Q^{calmin}} \right) \times (Q^{cal} - Q^{calmin}) + L_\lambda^{min} \quad (2.13)$$

Where, L_λ^{TOA} is the spectral radiance at TOA ($W \times m^{-2} \times sr^{-1} \times \mu m^{-1}$) and Q^{cal} is digital number in the image.

Although conversion to L_{TOA} gives the same radiometric scale for spectral bands, the distribution of solar radiation varies according to spectral region, inducing different quantities of incident solar irradiance ($W \times m^{-2}$). Therefore, it is necessary an additional conversion of spectral L_λ^{TOA} to TOA reflectance (ρ_λ^{TOA}) in order to consider the distinction of solar radiation amongst spectral bands, variation of earth-sun distance (d^2, astronomical units) and solar zenith angle (θ_0). Assuming the viewing target as an uniform Lambertian surface**,** conversion to ρ_λ^{TOA} (unitless) is given by Equation 2.14 (MARKHAM; BARKER, 1986; CHANDER et al., 2009):

$$\rho_\lambda^{TOA} = \frac{\pi \times L_\lambda^{TOA} \times d^2}{E_\lambda^{SUN} \times cos\,\theta_0} \quad (2.14)$$

Where, E_λ^{SUN} is the solar exoatmospheric spectral irradiances ($W \times m^{-2} \times \mu m^{-1}$) and generally is provided in image metadata or can be calculated using RSR and solar spectrum. Note that MSI/Sentinel-2A is already distributed at ρ_λ^{TOA} and OLI/Landsat-8 provides the radiometric rescaling in image metadata to simplify the radiometric conversion.

In section 2.1.2, we discussed the attenuation of solar radiation caused by key atmospheric constituents according to optical properties. In this context, surface monitoring by satellite images requires consistent removal of atmospheric absorption and scattering effects (FENG et al., 2013). The atmospheric correction of satellite images is an essential procedure to convert apparent radiance measured by the sensors

to surface reflectance. The seasonal variability of atmospheric conditions distorts the TOA reflectance distinctly, and consequently, quality of surface reflectance derived from atmospheric correction is highly dependent on the atmospheric condition (clean or turbid) at the time of image acquisition, surface characteristics (dark or bright surface), and sensor design (OKIN; GU, 2015). Moreover, historical records of multispectral imagery are now available from time-series datasets, which contribute to increase the importance of surface retrievals for long-term evaluations (ROY et al., 2014). There are several approaches for atmospheric correction: empirical image-based, radiative transfer (RT) models and relative correction or normalization (HADJIMITSIS et al., 2004). Amongst these alternatives, RT models provide a detailed calculation of atmospheric scattering and absorption to be applied to atmospheric correction of satellite images. A vector version of 6S (Second Simulation of a Satellite Signal in the Solar Spectrum) is recognized RT model used to simulate the atmospheric reflectance and transmissions for various sensors and environmental conditions (VERMOTE et al., 1997b). Assuming a lambertian homogeneous target, TOA reflectance can be estimated following Equation 2.15 (SOBOLEV, 1975; VERMOTE et al., 1997b):

$$\rho_\lambda^{TOA}(\theta_v, \theta_0, \varphi_0 - \varphi_v) = \left[\rho_\lambda^{ATM}(\theta_v, \varphi_v, \theta_0, \varphi_0) + t_\lambda^d(\theta_0) \times t_\lambda^u(\theta_v) \times \frac{\rho_\lambda^{SUP}}{1 - S_\lambda \times \rho_\lambda^{SUP}}\right] \times T_g(\theta_v, \theta_0) \quad (2.15)$$

Where, T_g refers to gases transmission of the principal absorbing constituents (O_2,O_3,CO_2, H_2O); ρ_λ^{ATM} is the atmospheric intrinsic reflectance by molecular and aerosol scattering; t_λ^d and t_λ^u represent the atmospheric transmittance of aerosol and molecular from sun to target (d) and target to sensor (u), respectively; S is the atmosphere spherical albedo of the atmosphere, θ_v, φ_v, φ_0 are the view zenith, view azimuth and solar azimuth angles, respectively. Solving Equation 2.15 for surface reflectance (ρ_λ^{SUP}) and simplifying the notations:

$$\rho_\lambda^{SUP} = \left(\rho_\lambda^{TOA}/T_g - \rho_\lambda^{ATM}\right)/\left[t_\lambda^d \times t_\lambda^u + S_\lambda \times \left(\rho_\lambda^{TOA}/T_g - \rho_\lambda^{ATM}\right)\right] \quad (2.16)$$

The atmospheric intrinsic reflectance (ρ_λ^{ATM}) is given as function of single- and multiple-scattering (first and second term on the right side of equation 2.17, respectively) from aerosol and molecular in successive orders of radiation interaction (HANSEN and TRAVIS, 1974):

$$\rho_\lambda^{ATM}(\theta_v, \varphi_v, \theta_0, \varphi_0) = \overbrace{\frac{\omega_\lambda \times P_\lambda(\Theta)}{4(\mu_o + \mu_v)} \times \left(1 - e^{-\tau_\lambda^{scat} \times \left[\frac{1}{\mu_o} + \frac{1}{\mu_v}\right]}\right)}^{1^{st}\ term} + \overbrace{\rho_\lambda^{mSCA}}^{2^{nd}\ term} \quad (2.17)$$

Where, τ_λ^{scat} is the sum of τ_λ^{aer} and τ_λ^{ray}, ρ_λ^{mSCA} is multiple-scattering, $\mu_o = \cos\theta_0$ and $\mu_v = \cos\theta_v$, and scattering phase function ($P_\lambda(\Theta)$) is:

$$P_\lambda(\Theta) = \frac{P_\lambda^{aer}(\Theta) \times \tau_\lambda^{aer} + P_\lambda^{ray}(\Theta) \times \tau_\lambda^{ray}}{\tau_\lambda^{scat}} \quad (2.18)$$

Where, Θ is the scattering angle in forward (+) and backward (-) directions:

$$\Theta = \arccos\left[\pm \mu_0 \mu_v + \cos(\varphi_0 - \varphi_v)\sqrt{(1 - \mu_0^2) \times (1 - \mu_v^2)}\right] \quad (2.19)$$

The first term on the right side of equation 2.17 accounts for scattering atmosphere directly into sensor viewing (single-scattering), while the multiple scattering regime is more complex to represent successive orders of radiation interactions within the coupled surface-atmosphere system. Note that we neglect the adjacency effects, so called environmental function. The atmospheric intrinsic reflectance varies with single scattering albedo (aerosol type), scattering phase function, sun-viewing geometry, aerosol and molecular optical depth. Aerosol model describes the micro-physical and optical properties used in the RT models, and common models are continental, urban, dust desert, biomass burning and maritime. Illustrating the aerosol properties, maritime aerosol type has ω_{550nm} of 0.989 while the urban ω_{550nm} is of 0.630 (D'ALMEIDA, 1991), which suggested that urban aerosols absorbs more when compared with continental.

Although RT models are sufficiently robust and can be used for routine image processing, this application requires parametrization with atmospheric information, mainly about aerosol loading in the atmosphere due to strong scattering effect in TOA signal. Particularly, the aerosol information is scarce across the South America, with routine measurements from AERONET sites in specific regions (Holben et al., 1998). As mentioned, satellite atmospheric products have capability to gap filling this required information with operational and routine products. At last, it is important to highlight that quantitative analysis is more sensible to larger error in surface retrievals than those applications focused in land-use classification or change detection by satellite images (SONG et al., 2001). Therefore, some applications do not require further image processing and atmospheric correction. Beside the atmospheric correction and radiometric calibration, we emphasize that remote sensing data has inherent uncertainties and need to be addressed, such as sensor degradation and effects of sun-view geometries (WANG et al., 2012; GALVÃO et al., 2009).

3 VALIDATION OF MAIAC AOD RETRIEVALS USING GROUND-TRUTH AERONET DATA OVER SOUTH AMERICA[1]

3.1. Introduction

Aerosols are suspended solid and liquid particles in the atmosphere derived from natural and anthropogenic sources. Common natural sources are desert dust, volcanoes, wildfire, sea salt and biogenic compounds from vegetation, while anthropogenic sources include biomass burning from logging and agricultural areas, fossil-fuel combustion and industrial pollution (LENOBLE et al., 2013). South America has a seasonal variability of aerosol burden in the atmosphere caused by industrial emissions in megacities, dust plumes across Patagonia and Atacama deserts and interannual biomass burning in Cerrado (Brazilian savanna) (VIDELA et al., 2013) and biogenic aerosol from Amazon rainforest (ARTAXO; HANSSON, 1995). These particles perform a complex function in climate system (IPCC, 2013) and bring large uncertainties on aerosol climate forcing (CARSLAW et al., 2013). Thus, many efforts have been made to understand the aerosol physical, chemical and optical properties (YU et al., 2006), as well as, aerosol-cloud interaction (WANG et al., 2016) and impacts on hydrologic cycle (ROSENFELD et al., 2014).

The AERONET (AErosol RObotic NETwork) program fills the knowledge gap of aerosol optical properties (HOLBEN et al., 1998). The program has an extensive network of sun photometers at global-scale that provides long-term database of solar and sky radiance measurements. Direct sun measurements provide spectral Aerosol Optical Depth (AOD or τ) and Ångström exponent (AE or α) at 340-1020 nm (HOLBEN et al., 2001). The AOD characterizes aerosol loading in the column of atmosphere, and α gives the spectral dependence of AOD, commonly related to the aerosol particle size (ECK et al., 2010). Thus, this reliable database allows insight on

[1] This chapter is an adapted version of the paper: MARTINS, V.S.; LYAPUSTIN, A; CARVALHO, L.A.S.; BARBOSA, C.C.F.; NOVO, E.M.L.M.. Validation of high-resolution MAIAC aerosol product over South America. **Journal Geophysical Research: Atmospheres**. (Under review).

aerosol optical and microphysical properties. However, the limited number of operational ground stations restricts some large-scale applications, where the spatial variability of aerosol is required. In contrast, satellite remote sensing provides global spatial coverage of aerosol with daily resolution, therefore being a useful data source to understanding aerosol patterns in the atmosphere (KAUFMAN et al., 2002).

Since the beginning of the twenty-first century, Earth Observation System (EOS) has provided valuable global data from Moderate Resolution Imaging Spectroradiometer (MODIS), enhancing monitoring, modeling and forecasting of global climate. In MODIS Atmosphere Collection, the "Dark Target" (KAUFMAN et al., 1997) and the "Deep Blue" algorithms (HSU et al., 2004) were applied to AOD retrieval over the dark surface and bright surfaces, respectively. Historical improvements in MODIS aerosol algorithms reveal the efforts for more accuracy and higher quality in satellite aerosol products (REMER et al., 2005; LEVY et al., 2007; 2013). Multiangle Implementation of Atmospheric Correction (MAIAC) is a recent MODIS algorithm designed to retrieve surface bidirectional reflectance factor (BRF), internal cloud mask, column water vapor (CWV) and AOD over land (LYAPUSTIN et al., 2011). In general, MAIAC applies time series approach to dynamically derive surface spectral ratios between MODIS blue at 0.47 μm and shortwave infrared (SWIR) bands at 2.1 μm used for 1 km AOD retrievals over dark and bright surfaces, with exceptions for bright salt pans and snow areas. The multi-angle observations from four or more cloud-free measurements are used to derive spectral surface bidirectional reflectance distribution function (BRDF), knowledge of which helps MAIAC smoke/dust detection and improves the accuracy of atmospheric correction. Particularly, it offers an advantage of prior knowledge of surface properties to overcome empirical assumptions from previous standard algorithms. Furthermore, AOD retrievals at 1 km resolution provides fine scale variability required for many applications, as smoke plume detection (LYAPUSTIN et al., 2012) and air pollution studies (KLOOG et al., 2015).

In this context, continuous validation efforts are vital to consolidate the confidence of aerosol products and their applications (CHU, 2002; ICHOKU et al., 2002; LEVY et al., 2010; SAYER et al., 2013). While accuracy of MAIAC surface reflectance was

thoroughly evaluated over the Amazon basin (e.g. HILKER et al., (2012)), a critical assessment of MAIAC AOD over South America is missing. Our objective is to perform an extensive validation of MAIAC AOD retrievals with AERONET measurements at continental scale as a function of land cover types, which range from the Atacama Desert to the Amazon forest in South America. This chapter-analysis is structured as follows: Section 2 provides a brief overview of the MAIAC and AERONET data, and Section 3 gives a complete description of the validation approach. In Section 4, we present a comparison for overall match-ups, and then, for each land cover type. Next, we discuss MAIAC performance according to AOD magnitude and seasonal aerosol distribution in South America. Finally, Section 5 presents the conclusions.

3.2. Data Description

3.2.1. AERONET data

The AERONET (AErosol RObotic NETwork) is a global network of automatic radiometers that performs measurements of direct solar and sky radiance in several channels at every 15 minute-interval (HOLBEN et al., 1998). These measurements are used to compute columnar AOD at interval from 350 to 1,020 nm based on Beer-Lambert-Bouguer law with expected uncertainties of ~ 0.01 to 0.021 (ECK et al., 1999). AERONET data is available in three categories: level 1.0 (unscreened), level 1.5 (cloud-screened), and level 2.0 (cloud-screened and quality-assured). In this study, we selected 19 AERONET sites with at least one year of quality assured data (level 2.0) within 2000-2015 (**Table 3.1**). These sites are geographically distributed over the continent (**Figure 3.1**), and are sensitive to several main aerosol types, such as biomass burning, urban pollution and dust plumes (HOLBEN et al., 2001). As AERONET does not provides measurements at 550 nm, AERONET level 2.0 data were interpolated to 550 nm using quadratic fits on a log-log scale (**Equation 3.1**) (ECK et al., 1999) .

$$\ln \mathrm{AOD} = \beta_2 (\ln \lambda)^2 + \beta_1 (\ln \lambda) + \beta_0 \qquad (3.1)$$

Where, $\beta_2, \beta_1, \beta_0$ are coefficients derived from multi-spectral AODλ values typically measured at 380, 440, 500, 675, 870, 1020 nm, and they can be used to interpolate the AOD measurement to 550 nm by Equation 3.1. The curvature β_2 is a reliable proxy of aerosol particle size, where the negative values represent fine-mode particles (radius <<1.0 μm) and the positive values are indicative of the coarse mode (radius >1.0 μm) (SCHUSTER et al., 2006). Second order interpolation has a satisfactory agreement with AERONET AODλ within ~ 0.01-0.02 (ECK et al., 1999).

Table 3.1. Over-Land AERONET sites used in this study. The ID number in parentheses is a reference to site location in Figure 1.

AERONET sites	LAT	LONG	Elevation (m)	Period	Available AOD days
Abraços Hill, Brazil (**1**)	10.76° S	62.35° W	200	1999-2005	1125
Alta floresta, Brazil (**2**)	9.87° S	56.1° W	277	1993-2016	3122
Arica, Chile (**3**)	18.47° S	70.31° W	25	1993-2016	3208
Balbina, Brazil (**4**)	1.91° S	59.48° W	80	1993-2003	558
Belterra, Brazil (**5**)	2.64° S	54.95° W	70	1996-2005	856
Campo Grande-SONDA, Brazil (**6**)	20.43° S	54.59° W	677	2003-2016	1547
Casleo, Argentina (**7**)	31.79° S	69.30° W	2552	2011-2014	1101
Ceilap BA, Argentina (**8**)	34.56° S	58.50° W	10	1995-2016	2637
Ceilap RG, Argentina (**9**)	51.60° S	69.32° W	15	2005-2016	838
Cordoba-CETT, Argentina (**10**)	31.52° S	64.46° W	730	1994-2010	1667
Cuiabá-Miranda, Brazil (**11**)	15.72° S	56.02° W	210	2001-2016	2331
Ji Paraná-SE, Brazil (**12**)	10.93° S	61.85° W	218	2000-2016	995
La Paz, Bolivia (**13**)	16.53° S	68.06° W	3439	2005-2016	1467
Manaus Embrapa, Brazil (**14**)	2.89° S	59.96° W	115	2011-2016	511
Rio Branco, Brazil (**15**)	9.95° S	67.86° W	212	1994-2016	2140
Santa Cruz, Bolivia (**16**)	17.80° S	63.17° W	442	1993-2016	1170
São Martinho Sonda, Brazil (**17**)	29.44° S	53.82° W	489	2003-2016	746
São Paulo, Brazil (**18**)	23.56° S	46.73° W	865	2000-2016	1373
Trelew, Argentina (**19**)	43.24° S	65.31° W	15	2000-2016	1927

Figure 3.1. Geographical distribution of the AERONET sites. The code numbers identify AERONET sites described in Table 3.1. Background of Global Land Cover product (BROXTON et al., 2014) reclassified to seven land cover types.

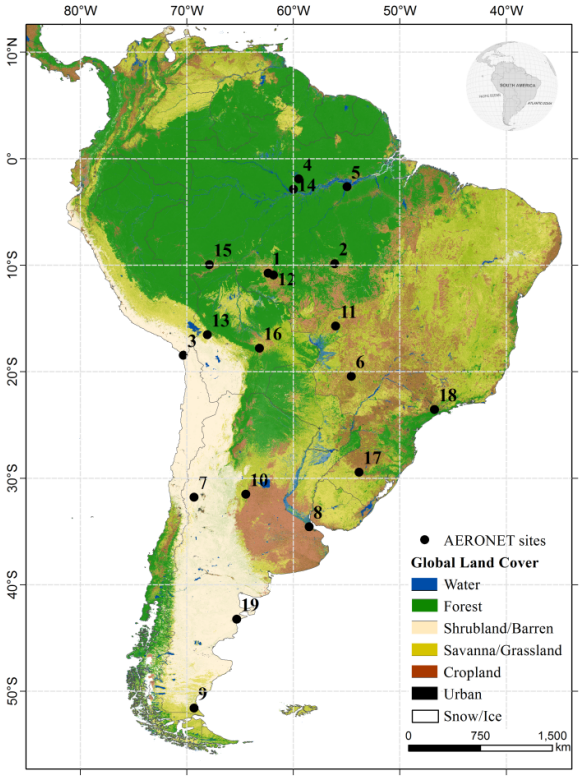

3.2.2. MAIAC

MAIAC products have been available since 2000 for Terra and 2002 for Aqua and delivered in Hierarchical Data Format (.HDF). The suite of atmospheric products includes cloud mask, AOD at 0.47 and 0.55 µm gridded at high-resolution (1 km), and column water vapor from MODIS NIR bands at 0.940 µm. Since the publication of Lyapustin et al. (2011), MAIAC algorithm has added capability for smoke (dust) detection (LYAPUSTIN et al., 2012), improved aerosol retrieval over bright deserts, improved cloud and snow mask, added aerosol retrievals and atmospheric correction over inland, coastal and open ocean water, and has undergone considerable changes for global application. Storing multi-day records from MODIS, the algorithm adds the knowledge of time series to decouple surface and aerosol information using the following assumption: aerosol events are extremely variable during the daytime and homogeneous at small areas (~30 km²), while the land surface is typically stable over a short timescale and heterogeneous spatially. A publication, describing MAIAC Collection 6 algorithm, is under preparation and will be available shortly. This study applies MAIAC AOD_{550} (2000-2015) from MODIS C6 Terra and Aqua data collocated

with ground-based measurements in the validation approach. **Figure 3.2** shows an example of true-color image of (a) MODIS Terra and (b) MAIAC AOD retrievals acquired on September 8, 2007 over South America. This figure gives an example of MAIAC aerosol retrievals in clear-sky pixels under partly cloudy and clear conditions during biomass burning season.

Figure 3.2. Example of MAIAC aerosol loading on 08 September 2017 (dry season). (a) MODIS True-color image; (b) MAIAC AOD under partly cloudy (top-panel) and clear condition (bottom-panel).

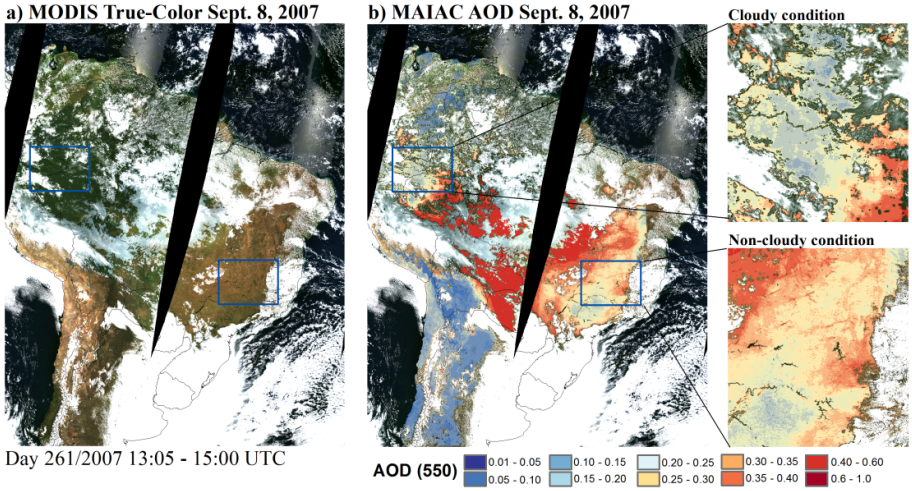

3.3. Validation approach

3.3.1. General

Validation requires spatial and temporal collocation for MAIAC and AERONET AOD_{550} comparison. Section 3.3.2 shows our spatiotemporal evaluation (topics i and ii), and Section 3.3.3 defines the land cover groups (topic iv). In general, the validation approach is based on the following procedures (**Figure 3.3**):

(i) Ground-based measurements consist of at least one AERONET AOD_{550} value within ±60 minutes interval from MODIS Terra/Aqua overpass with average of two or more values within the interval.

(ii) MAIAC values were averaged within a 25 x 25 km² centered at each site. This average value is acceptable if at least 40% of the total cells are valid values within a window (ICHOKU et al., 2005).

(iii) The valid data is filtered between $0.01 < AOD_{550} < 4.0$ (XIE et al., 2011). This filter removes unexpected high AOD values from cloud residual and extreme low values that exceed the uncertainty of AERONET measurements (~0.01-0.02). This range contains typical AOD values for comparison between ground-based and satellite observations (ICHOKU et al., 2005).

(iv) AERONET sites were grouped into six classes according to the major land cover type within 25 x 25 km². These groups allow evaluation of the algorithm dependence with surface properties and discussion as function of land cover type.

(v) Statistical analysis (Section 3.3.4) includes linear regression and error metrics from MAIAC and AERONET AOD_{550} correlation.

Figure 3.3. Flow-chart of validation approach.

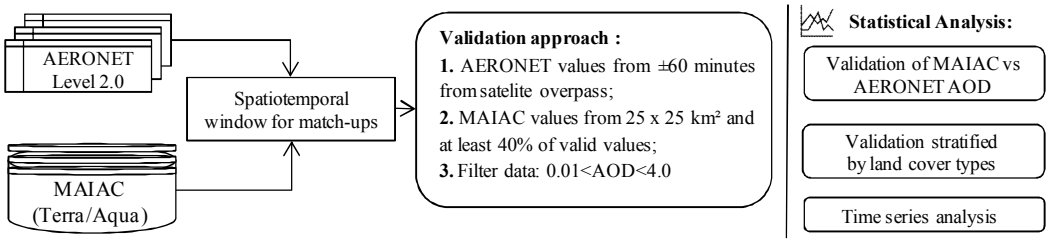

3.3.2. Spatio-temporal window

Ground-based measurements provide a high sampling rate (~15 min) at the local point, while satellite images have large spatial coverage at a short time interval. Direct comparison using only one pixel value located over ground stations or ground measurements obtained at the exact time of satellite overpass restricts the probability for matchup data, due to cloud cover or time delay between satellite and ground-based measurements. Assuming that aerosol plume is relatively homogeneous within a certain time-space boundary (ANDERSON; CHARLSON, 2003), it is pertinent to use the AOD retrievals within some spatial window and time interval have been used for validation (e.g., Ichoku et al., (2002)). For this reason, we perform an average of AERONET measurements for four time intervals (t) from 30 to 120 min centered at satellite overpass to compare it with the average of MAIAC retrievals for five spatial windows

(d) from 3 km to 125 km centered at each site-point. The selected spatial and temporal window is committed to a better balance between correlation quality and sample size.

Indeed, the highest correlations are expected for the minimum time lag and the smallest window-size. From overall statistics for Terra and Aqua products in **Table 3.2**, results show little variability in agreement over time lag and window-size. The sample size tends to increase with both time and space windows, despite the fact that the case of d < 75 km shows fewer match-up pairs than that of d < 25 km for MODIS Aqua as result of the average filter that requires at least 40% of valid points. For window of 25 km, the comparisons reveal an increase of match-ups and correlations compared to those of the 3 km window for both products, although results remain very close in most cases. Therefore, we selected the 25 x 25 km² as one of the balanced window with reasonable sample size and correlation quality. Additionally, this spatial window is within mesoscale aerosol homogeneity ~50-60 km² (ANDERSON; CHARLSON, 2003), rather similar to 20 x 20 km² used in a previous MAIAC validation (LYAPUSTIN et al., 2011) and close to 25 km radius used for the global validation of MODIS Deep Blue AOD (SAYER et al., 2013).

As observed in **Table 3.2**, the time interval has a small impact in the overall agreement for both products, mostly because the average over delta time also includes AOD_{550} values from a previous time threshold. Thus, we selected an interval of ± 60 min as a reasonable match-up period, due to sample size increases from 8136 (± 30 min) to 8575 (± 60 min) for Terra using 25 x 25 km² and this interval is close to one used for MISR validation (KAHN et al., 2005). Therefore, the validation approach applies the average MAIAC retrievals within 25 x 25 km² centered at each site compared to an average of AERONET measurements within ± 60 minutes around the time of the satellite overpass.

Table 3.2. Match-up analysis applied to various spatial (d) and temporal (t) window for Terra (a) and Aqua (b). First line: number of match-ups/correlation coefficient, second line: RMSE/Bias. The selected time-space threshold is presented in bold.

(a) **TERRA**	t ≤ 30 min	**t ≤ 60 min**	t ≤ 90 min	t ≤ 120 min
d < 3 km	7642 / 0.956 0.071 / -0.016	8136/0.952 0.075/-0.015	8372 / 0.950 0.077 / -0.015	8568 / 0.948 0.078 / -0.015
d < 15 km	7916 / 0.957 0.069 / -0.020	8443 / 0.955 0.072 / -0.019	8681 / 0.953 0.074 / -0.019	8877 / 0.952 0.078 / -0.015
d < 25 km	8017 / 0.958 0.068 / -0.024	**8575 / 0.956** **0.071 / -0.023**	8813 / 0.954 0.072 / -0.023	9017 / 0.953 0.074 / -0.023
d < 75 km	7981 / 0.953 0.072 / -0.032	8615 / 0.952 0.075 / -0.032	8889 / 0.951 0.076 / -0.032	9104 / 0.950 0.076 / -0.032
d < 125 km	8232 / 0.949 0.074 / -0.030	8998 / 0.946 0.077 / -0.031	9376 / 0.944 0.078 / -0.032	9627 / 0.943 0.079 / -0.032
(b) **AQUA**	t ≤ 30 min	**t ≤ 60 min**	t ≤ 90 min	t ≤ 120 min
d < 3 km	6060 / 0.949 0.076 / -0.005	6459 / 0.945 0.078 / -0.006	6653 / 0.943 0.079 / -0.006	6799 / 0.941 0.081 / -0.006
d < 15 km	6341 / 0.954 0.071 / -0.014	6733 / 0.949 0.075 / -0.015	6919 / 0.947 0.076 / -0.015	7076 / 0.946 0.077 / -0.016
d < 25 km	6340 / 0.954 0.071 / -0.019	**6740 / 0.949** **0.075 / -0.020**	6931 / 0.947 0.075 / -0.021	7083 / 0.946 0.076 / -0.021
d < 75 km	6182 / 0.948 0.072 / -0.029	6602 / 0.944 0.0741 / -0.029	6802 / 0.943 0.074 / -0.030	6965 / 0.942 0.074 / -0.031
d < 125 km	6259 / 0.942 0.075 / -0.029	6716 / 0.939 0.077 / -0.030	6932 / 0.938 0.077 / -0.031	7099 / 0.938 0.077 / -0.031

3.4. Land cover around AERONET sites

Since satellite algorithms rely on surface spectral properties to decouple atmosphere and surface contributions, the land cover introduces background context to understand the limitations of MAIAC AOD_{550} retrievals. Global Land Cover (GLC) is a MODIS product at 0.5 km spatial resolution that supports our analysis with land cover information around each AERONET site (BROXTON et al., 2014).

As expected, the global product often presents undesirable classification errors, due to inherent difficulties to distinguish surfaces with similar spectral properties, inter annual variability and limited spatial resolution. In GLC product over Brazil, cropland is often confused with savanna. In particular, cropland areas are significant aerosol sources due to biomass burning and soil particles suspended from tillage practices. For instance, Ji Parana-SE site shows the mean AOD_{550}~ 0.338 with wide variation from 0.018 to 4.76 as influenced by the biomass burning during the winter season (HOELZEMANN et al.,

2009). Once the importance of these areas was recognized, we refined the GLC information over savanna areas using the agricultural areas classified by the Brazilian Institute of Geography and Statistics (IBGE). The IBGE is an official institute that provides the classification of land cover and land use based on MODIS time-series, OLI/Landsat-8 and Rapid-Eye images, and field information (IBGE, 2016). Here, the savanna and pasture of GLC product were overlaid by agricultural areas from IBGE classification.

The first level of GLC types was reclassified into seven generic land covers (see Figure 3.1). From these classes, we extracted the cover types within 25 x 25 km² window around each AERONET to group these sites as function of major land cover (at least 50%) (**Table 3.3**). The mixed group includes all AERONET sites without a predominant land cover type (less than 50%). **Table 3.3** shows the similarity between AERONET AOD mean and standard deviation stratified by land cover types. Indeed, a quite similar AOD regimes is expected when particles are driven by the same aerosol sources, although boundary conditions, such as elevation, topography, surface features, and wind transport, might change the aerosol distribution and patterns.

The AERONET program clearly concentrates efforts on exploring aerosol dynamic under several environmental conditions (HOLBEN et al., 2001). **Table 3.4** shows land cover distribution around the selected AERONET sites. This distribution reveals aerosol monitoring efforts near land features susceptible to wildfire and biomass burning events, such as savanna, grassland, and cropland, over South America.

Table 3.3. Basic statistics of AERONET sites grouped according to major land cover type.

Land cover	AERONET sites	Major land cover (%)	AOD_{550} (mean ± std)
Forest	Balbina	58.95	0.179 ± 0.110
	Manaus Embrapa	76.68	0.192 ± 0.151
Shrubland/Barren	Casleo	100	0.024 ± 0.018
	Trelew	86.78	0.035 ± 0.028
Savanna/Grassland	Ceilap RG	66.34	0.022 ± 0.013
	Cordoba CETT	56.03	0.080 ± 0.065
	Santa Cruz	50.84	0.183 ± 0.173
Cropland	Abraços Hill	62.84	0.338 ± 0.369
	Alta Floresta	64.68	0.253 ± 0.392
	Cuiabá Miranda	71.36	0.233 ± 0.334
	Ji Paraná SE	71.68	0.338 ± 0.494
	Rio Branco	62.89	0.248 ± 0.304
Urban	Ceilap BA	76.78	0.089 ± 0.075
	São Paulo	90.77	0.214 ± 0.150
Mixed	Arica	*	0.219 ± 0.107
	Belterra	*	0.209 ± 0.171
	Campo Grande	*	0.127 ± 0.198
	La Paz	*	0.084 ± 0.045
	São Martinho	*	0.071 ± 0.078

Table 3.4. Land cover distribution around AERONET sites.

Land Cover type	AERONET sites (%)
Water bodies	7.80
Forests	9.84
Shrubland/Barren	16.25
Savanna/Grassland	22.96
Croplands	25.91
Urban	17.34

Since the aerosol type depends on origin and transport, these particles are directly related to the surface type and its typical sources (LENOBLE et al., 2013). Note that although local aerosol sources influence on aerosol regimes, long-range transport can also change the background aerosol in remote areas (ANDREAE et al., 2008) – for example, Saharan dust and biomass burning smoke transported by trade wind from Africa reach the Amazon basin (BAARS et al., 2011). To explore the relation of AOD and ångström exponent for each land cover type, **Figure 3.4** presents a scatter plot for AOD and the ångström exponent with distinct patterns among land covers. The coarse-mode particles (median radius > 0.6 μm and $\alpha_{440-670}$<0.5) observed over barren and

sparse vegetation is also common in desert regions (BASART et al., 2009). The fine-mode particles (median radius < 0.6 μm and $\alpha_{440-670}$~ 1.2-1.5) are most frequent for continental sources, as urban pollution with AOD ~ 0.2 to 1.0. For the cropland group, the biomass burning season changes the aerosol burden that increases to high AOD values (~ 1.5 - 3.5) and small particle size ($\alpha_{440-670}$ ~ 1.5-2.0). Therefore, a validation scheme using land cover groups introduces surface background and aerosol context, wherein the typical AOD range varies according to aerosol sources located in each cover type.

Figure 3.4. Scatter points of AOD_{550} versus Ångström exponent (440-670 nm) for land cover types. The scatter provides 5000 random pair-points from AERONET site per land cover type: Ji-Paraná SE (Cropland; Brown); São Paulo (Urban; Black); Manaus Embrapa (Forest; Green); Casleo (Shrubland/Barren; Gray); Ceilap RG (Savanna/grassland; Yellow).

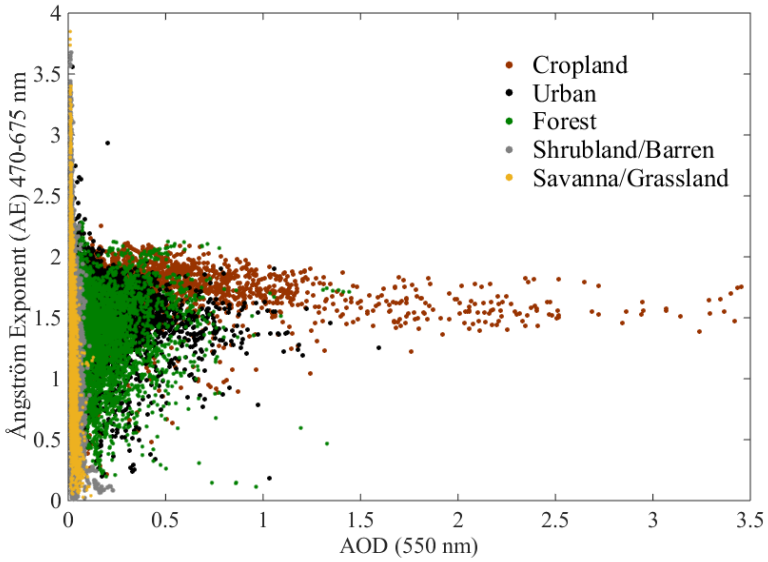

3.5. Statistical analysis

The linear regression is used to evaluate the MAIAC and AERONET AOD_{550} correlation (**Equation 3.2**):

$$AOD_{MAIAC} = \beta_1 \, x \, AOD_{AERONET} + \beta_0 \qquad (3.2)$$

The slope (β_1) and intercept (β_0) coefficients denote the linearity of the relationship between MAIAC and AERONET measurements. Even for accurate approaches, bias is

expected for both coefficients (β_1 and β_0), due to inherent uncertainties of satellite retrievals, as sensor calibration, aerosol model assumption, residual cloud, surface effects or topographic variations (LI et al., 2009). The quality of satellite aerosol products from MODIS Collections using DT and DB algorithms were well-documented and globally validated (REMER et al., 2005; LEVY et al., 2010; LEVY et al., 2013; SAYER et al., 2013). The historical application of these products is consequence of rigorous validation and evaluation of uncertainties in retrieval process. For DT algorithm, the expected error (EE) envelope was defined as ± (0.05 + 0.15*AOD) over land, containing 2/3 of retrievals (66% or approximately one standard deviation σ) falling within the EE limits (REMER et al., 2005; LEVY et al., 2010). The EE envelope includes the absolute (0.05) and relative (0.15) uncertainties of AOD retrievals, such as surface properties, sensor calibration, aerosol models, and empirical thresholds (LEVY et al., 2010). Although EE limits are a benchmark to evaluate the standard MODIS aerosol product, the performance level of MAIAC algorithm expects to overcome empirical assumptions due to dynamic spectral regression coefficient (SRC) characterization and knowledge of surface spectral BRDF. Thus, we will evaluate the target accuracy of EE envelope assuming the relative error of 0.05 as consequence of MAIAC advances from MODIS Collection 6 (Equation 3.3) and fraction of retrievals falling within EE envelope calculated by Equation 3.4:

$$EE = \pm (0.05 + 0.05 \times AOD) \tag{3.3}$$

$$AOD - |EE| \leq AOD_{MAIAC} \leq AOD + |EE| \tag{3.4}$$

Additionally, this validation analysis makes extensive use of the Root Mean Square Error (RMSE), normalized RMSE (NRMSE), and mean bias (Bias) calculated by Equations 3.5, 3.6 and 3.7, respectively.

$$RMSE = \sqrt{\left(\frac{1}{n} \sum_{i=1}^{n} \left(AOD_{MAIAC} - AOD_{AERONET}\right)^2\right)} \tag{3.5}$$

$$NRMSE = \frac{RMSE}{\overline{AOD}_{AERONET}} \tag{3.6}$$

$$Bias = \frac{1}{n} \sum_{i=1}^{n} AOD_{MAIAC} - AOD_{AERONET} \tag{3.7}$$

The $\overline{AOD}$ is the mean value and n is the number of match-ups.

3.6. Results and Discussion

3.6.1. Overall MAIAC and AERONET AOD_{550} comparison

Figure 3.5 shows the scatter plots for MAIAC Terra and Aqua retrievals against simultaneous AERONET measurements. The linear regressions were fitted with 8575 (Terra) and 6740 (Aqua) match-ups from MAIAC products at 19 AERONET sites. The results showed suitable MAIAC retrievals for both Terra and Aqua products, with slope of linear regression and R close to unity ($Slope_{Terra/Aqua}$: 0.863/0.839 and $R_{Terra/Aqua}$: 0.956/0.949). Both Remer et al. (2005) and Levy et al. (2010) suggested that aerosol product reaches a satisfactory accuracy when more than 66% of retrievals (2/3 or ~ one sigma) falling within EE limits. Using this approach for MAIAC AOD product, our evaluation showed confident retrievals for both MAIAC products with the fraction of retrievals within EE (Equation 3) of 67.9% for Terra and 66.7% for Aqua. For comparison, both MODIS collections 5 (C5) and 6 (C6) had quite similar accuracy to our results, since the slope/R are 0.936/0.840 for C5 and 0.949/0.860 for C6 (LEVY et al., 2013) The quality of MAIAC AOD products is rather similar to the previous MODIS collections, but present substantial advances for retrievals at 1 km resolution and lower relative error in EE (0.15 to 0.05). Our results also show comparable quality retrievals between MODIS instruments that allow fine-scale applications using combined Terra and Aqua retrievals. Figure 3.5a-ii and Figure 3.5b-ii show the bias (y-axis) versus AOD values (x-axis) for Terra and Aqua, respectively. The results present distinct bias trend: i) positive bias up to AOD = 0.1 values, and ii) a low albeit systematic negative bias for AOD values > 0.1. At low AOD (< 0.1), the surface-related errors lead to a small positive bias, while at high AOD, representing biomass burning, a constrained negative bias indicates the need to refine the regional aerosol model (in particular, by increasing aerosol absorption).

Figure 3.5. Scatter plots of MAIAC Terra (a) and Aqua (b) against AERONET AOD_{550}. The line 1:1 and MAIAC expected error (EE = ± 0.05 ± 0.05×AOD) are shown in solid blue and shaded gray area, respectively. In top-left text: regression equation, correlation coefficient (R), number of match-ups (n), and fraction of retrievals within EE. In bottom-right text: statistics binned by AOD intervals.

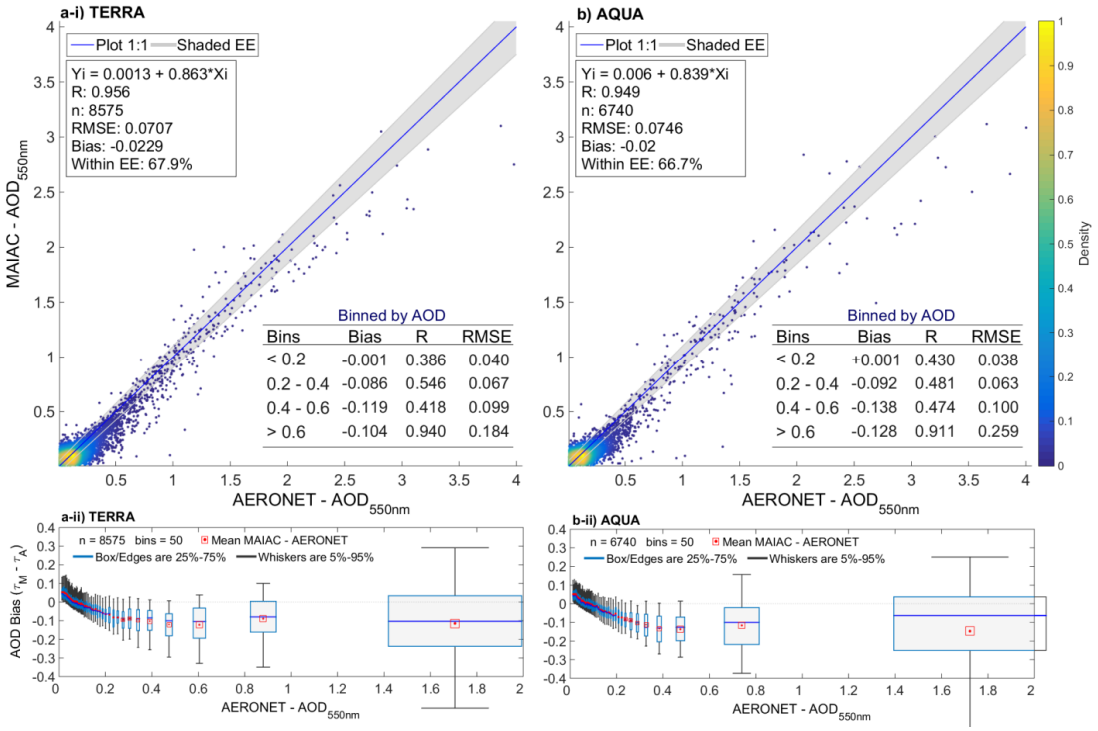

As discussed in Section 3.3.2, the AE acts as a proxy for particle size and bias analysis versus AE is rather instructive to understand aerosol type impacts on AOD retrievals. **Figure 3.6a** presents the AOD bias (τM – τA) as a function of the AERONET AE470-670nm (x-axis) colored by AERONET AOD retrieved. The match-ups were sorted by AE values and then grouped into 50 bins for each statistic box. Figure 3.6b and 3.6c represent the bias statistics versus AE values for lower (< 0.4) and higher AOD (>0.4), respectively, with box edge of 25-75% and whiskers of 5-95% in each bin. In lower AOD than 0.4 (Figure 3.6b), MAIAC retrievals have an absolute bias lower than 0.03 regardless of the AE value (0 < AE < 3.0). In turn, MAIAC retrievals for AOD higher than 0.4 present a systematic negative bias within AE interval (0.75 < AE < 2.0), with negative bias near -0.24 (AE < 1.6), and then, decrease to – 0.15 (AE > 1.6). In particular, bias is generally close to zero (up to ± 0.05) for coarse-dominated aerosol (AE < 0.6). Similarly, Superczynski et al. (2017) reported high AOD bias at coarse or mixed particle sizes (AE 0.5 < AE < 1.75) with slight negative trend (See Figure 6 therein). Therefore, our main results are slight negative bias trend for low AOD

regardless of particle size (to better than 0.03, Figure 3.6b) and higher negative bias in coarse-dominated conditions (Figure 3.6c).

Figure 3.6. MAIAC-AERONET AOD bias (τM – τA) at 550 nm (y-axis) versus Ångström exponent (AE) from AERONET (x-axis). (a) AOD bias using all match-ups from both Terra and Aqua colored by binned AOD from AERONET retrieval. Match-ups are sorted by the AE and grouped into 50 equal bins for (b) lower and (c) higher than 0.4. Each box edge and whiskers represent the 25-75% and 5-95% of data with median (black line) and mean (red point).

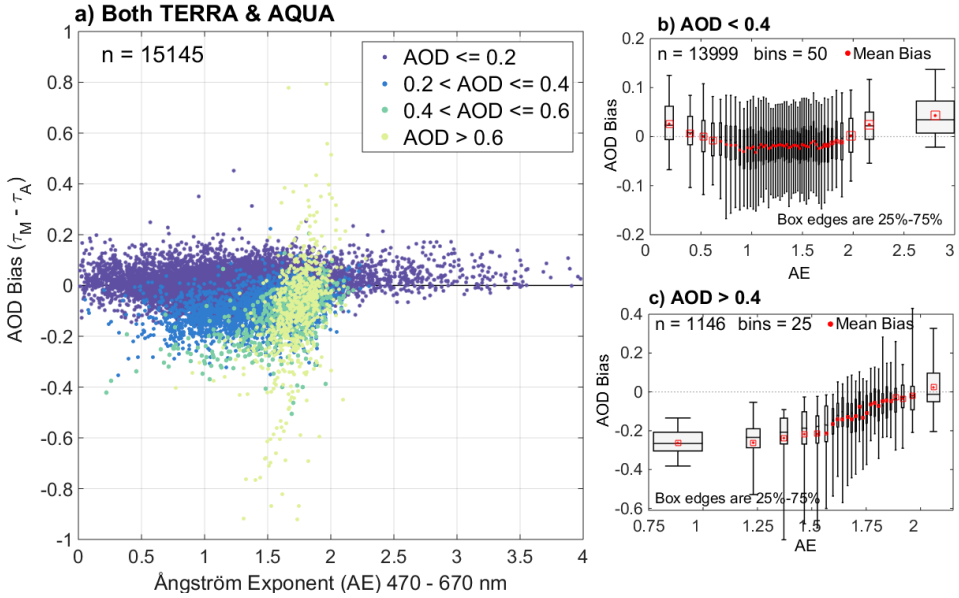

Figure 3.7 shows that the asymmetric distribution of AOD_{550} dataset concentrates more than 98% of values between 0.01- 1.0. The extreme high AOD_{550} (>1.0) represents less than 1.8 % of aerosol events that are most driven by agriculture practices, as seen in Figure 3.3. In general, frequency distribution of both Terra and Aqua products showed significant differences between satellite and ground-based retrievals at low AOD (0.01 - 0.2) and it decreased exponentially for moderate-high (~ 0.4 - 1.0) and extreme high (>1.0) AOD values. The highest difference in frequency distribution occurred for low AOD values caused by surface noise on clear atmospheric days. As observed for MOD04 C5, high surface reflectance contributions at low AOD reduce the AOD sensitivity in TOA reflectance (LEVY et al., 2010), however the absolute error of MAIAC AOD remains small.

Figure 3.7. Frequency distribution of MAIAC and AERONET AOD_{550}. Text box: number of AOD_{550} values within interval, bias and number of match-ups (n).

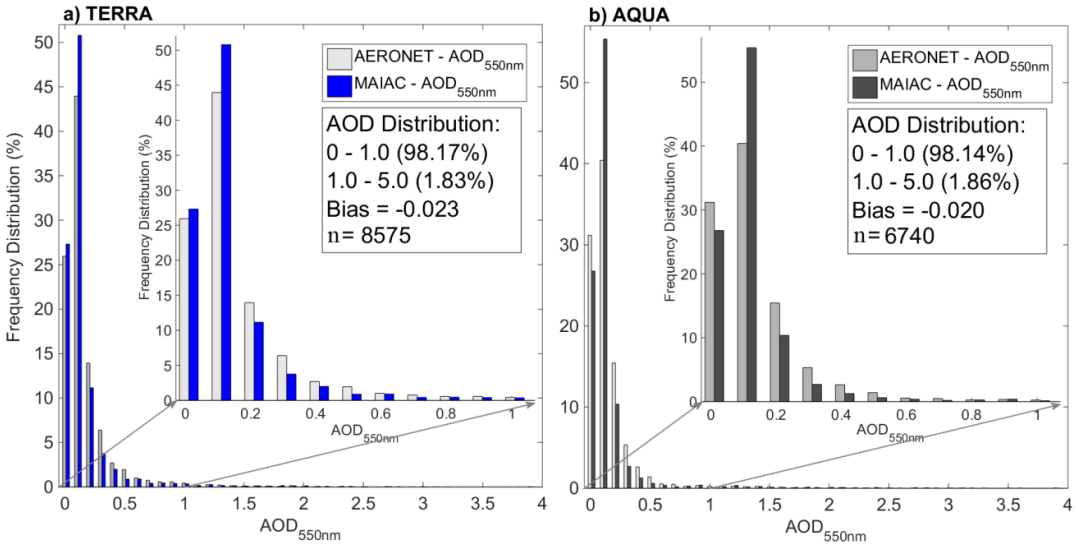

3.6.2. MAIAC and AERONET AOD_{550} comparison over land cover types

MAIAC algorithm integrates time series analysis and image processing to decouple surface reflectance and atmosphere properties. Thus, the performance of MAIAC aerosol depends on two key factors: surface type and aerosol properties. The TOA reflectance is clearly more sensitive to aerosol effects over dark surfaces than over bright surfaces (SEIDEL; POPP, 2012). Since the background surface properties are essential to aerosol retrievals, the validation of MAIAC is performed considering the land cover types.

Figure 3.8 shows the MAIAC and AERONET AOD_{550} comparison for individual land cover types. As described, the major land cover type within 25 x 25 km² around AERONET site defines the cover group, while the mixed areas include the sites without representative land cover (Table 3.3). At least 15 match-ups were used to binned-AOD analysis in each sub-plot. The sample size ranges from 170 (forest) to 3232 (cropland) match-ups for Terra and from 20 (forest) to 2250 (mixed) for Aqua product. Note that AOD range varies for each land cover analysis, due to distinct aerosol sources for each land use and cover type. Our results showed that the AOD retrievals are sensitive to land cover types, where surface properties and AOD magnitude become a key factor to MAIAC performance. Benas et al. (2013) evaluated the aerosol products from MODIS and MERIS/AATSR synergy algorithm considering land cover types and also identified the dependence on surface albedo and aerosol microphysics. In summary, MAIAC retrievals were more accurate and better correlated with AERONET measurements over forest, cropland, mixed, savanna and grassland than those of urban, shrubland and

barren areas. For comparison, the highest overall correlation was for retrievals over cropland areas, with R near to unity (R_{Terra}: 0.981 and R_{Aqua}: 0.977), and the lowest correlation over shrubland and barren areas– positive bias (+0.062) and low R (R_{Terra}:0.221 and R_{Aqua}: 0.24).

In forest areas (**Figure 3.8a**), MAIAC and AERONET AOD_{550} comparison showed a good correlation for both products, where slope of linear regression ($Slope_{Terra}$: 0.783 and $Slope_{Aqua}$: 0.817) and R were close to unity (R_{Terra}: 0.878 and R_{Aqua}:0.891). Comparing the two products, MAIAC Aqua had a better EE (75.9%) than that of Terra (66.5%) over forest areas, although both products presented fair accuracy that exceeded the 66% threshold. This difference of EE might be related to delta in sample size ($\Delta n = 170 - 29 = 141$) or cloud cover contrast between the morning and the afternoon orbits (HILKER et al., 2015). This evergreen surface provides temporal stability and strong SRC retrievals that enhance the confidence of surface BDRF at the blue band and aerosol retrieval, as benefits of dense dark vegetation areas (KAUFMAN et al, 1997). Petrenko and Ichoku (2013) also confirmed the suitability of forest surfaces to AOD retrievals and found correlation coefficient higher than 0.84 for multiple sensors (MODIS, MISR, and POLDER) compared with AERONET measurements. In our case, the dense Amazon rainforest around Manaus-Embrapa and Balbina sites explains the algorithm success, as these dark vegetated surfaces increase the sensibility of aerosol dynamics in TOA reflectance. Nevertheless, moderate scattering might be related to the ensemble of aerosol types and cloud residual. Artaxo et al. (2013) showed a high variability of aerosol properties in the Amazon region caused by the mixture of biomass burned and organic fine-mode particles, wherein the single scattering albedo (SSA) changes from 0.84 in the wet season to 0.91 in the dry season. In general, forest areas provide feasible surface condition to accurate AOD retrievals and MAIAC products exhibited acceptable retrievals (to lower than absolute error of 0.05) with biases of -0.045 and -0.006 for Terra and Aqua, respectively.

The shrubland and barren areas are arid climate regions with sparse vegetation coverage (~10-20%) of perennial and drought-resistant plants, gravels and sandy soil. We found the poorest agreement between MAIAC and AERONET AOD_{550} measurements for these arid areas compared to all other land covers (**Figure 3.8b**). For Patagonia and Atacama deserts, the bright surfaces and typical low AOD introduce challenging boundary conditions for satellite aerosol retrievals. As seen in Figure 8b, the high biases ($bias_{terra}$: 0.063 and $bias_{Aqua}$: 0.049) at low AOD and the non-zero intercept of linear regression (~ 0.1) might be explained by SRC underestimation and inherent difficulty to decouple atmosphere-surface signal over bright surfaces. Consequently, satellite AOD may show a high noise and a positive bias over these areas, for instance as observed in one extreme case with MAIAC AOD_{550} of 0.29 compared to AERONET of 0.04. The

typical low AOD regimes across Patagonia and Atacama regions, as seen in Trelew (0.082 ±0.058) and Casleo (0.028 ±0.018) sites, clearly illustrate the sensitivity limits of MAIAC retrievals over barren and bright land surfaces at high spatial resolution.

Figure 3.8c shows meaningful MAIAC retrievals over savanna and grassland areas, where scatter of points was closer to the 1:1 line with slight negative bias and R exceeding 0.85 for both sensor products. There is a quite similar fraction of AOD retrievals within EE (Terra: 77.6% and Aqua: 75.3%) and mean bias of -0.012 and -0.014 for Terra and Aqua, respectively. The savanna biome in the central Brazil faces intensive land use change and local fire practices during the dry season (CHEN et al., 2013).Thus, MAIAC time series benefits aerosol retrievals over these regions with seasonal surface changes. Furthermore, since savanna and grassland surfaces cover more than one-quarter (~28%) of South America, reliability of MAIAC retrieval allows routine monitoring of the smoke plumes.

During the dry season, agriculture and pasture areas are hot spots for natural and human-induced fires over South America and satellite AOD retrievals have been used in biomass burning monitoring over these areas (HOELZEMANN et al., 2009). **Figure 3.8d** shows that MAIAC retrievals over cropland areas had a better agreement with AERONET measurements than that of all other cover types, with R close to unity (Terra: 0.981 and Aqua: 0.977) and higher fraction of retrievals within EE (Terra: 72.9% and Aqua: 75.2%) than 66% for both products. In comparison, the overall correlation of MAIAC Terra was slightly better than that of Aqua. Benas et al. (2013) also showed good AOD retrievals for MERIS/AATSR synergy algorithm (Slope: 0.835 and R: 0.68) and MOD04 C5 (Slope: 0.762 and R: 0.81) over cropland areas. These managed areas experience a dramatic surface change throughout the agricultural cycle, with distinct surface conditions during soil preparation, crop planting and harvest periods. Since MAIAC approach partly relies on stable surface condition, the rapid change of surface properties still represents a certain challenge for unbiased aerosol retrievals over agricultural areas - although our results do not show any systematic issue.

MAIAC and AERONET AOD_{550} comparison over urban areas are shown in **Figure 3.8e**. Note that these retrievals had spread scatter points at low AOD values and a slight tendency to underestimate values ($bias_{terra}$: -0.042 and $bias_{Aqua}$: -0.048). MAIAC performed better over urban areas than over shrubland and barren areas, but not as well than over vegetated areas. The fraction of retrievals within EE from Aqua (57.7%) was better than that of Terra (54.7%) and quite similar to fraction from shrubland and barren areas (56.1%). This difference suggests that Aqua product is more appropriate for urban retrievals. In general, urban features impose many challenges for satellite aerosol retrievals at high resolutions, such as (i) multiple anthropogenic sources and a high

ensemble of aerosol optical properties and (ii) bright surfaces with a mixture of concrete building and roads. In our study case, the urban retrievals used two AERONET sites located in big cities of South America: Buenos Aires, and Sao Paulo. These complex urban areas produce a high contribution in TOA reflectance that reduces sensitivity of measurements to aerosols. For comparison, MOD04 AOD retrievals historically present an overestimation over bright surfaces due to poor surface characterization (OO et al., 2010). Furthermore, the multiple pollutant sources also contribute to the ensemble of aerosol microphysics which represents a difficulty for aerosol models used in satellite retrievals. Castanho et al. (2008) showed the seasonal variation of SSA_{550} (0.75 – 0.96) over Sao Paulo and performed a sensitivity analysis showing that the uncertainties of 0.1 in SSA_{550} lead to at least 20% of error in AOD retrievals. Therefore, the spread scatter of points for urban retrievals might be explained by the discrepancy between the model and the actual aerosol microphysical properties. In contrast with our results, Lyapustin et al. (2011) validated MAIAC retrievals with UCLA AERONET site located in Los Angeles/EUA and showed the satisfactory correlation with slope and R of 0.822 and 0.873, respectively. This contrast with our results might be related to a large ensemble of urban aerosol types and limitation of a fixed aerosol model in MAIAC.

Figure 3.8. Scatter plots of MAIAC and AERONET AOD_{550} comparisons for land cover types: Forest (a); shrubland and barren (b); savanna and grassland (c); cropland (d); urban (e); and mixed areas (f). The MAIAC Terra (i) and Aqua (ii) are presented for each land cover. The line 1:1 and MAIAC expected error (EE = ± (0.05 + 0.05×AOD)) are shown in solid blue and shaded gray area, respectively. In top-left text: regression equation, correlation coefficient (R), number of match-ups (n), and fraction within EE. In bottom-right text: statistics binned by AOD intervals. At least 15 match-ups were required to analysis binned by AOD.

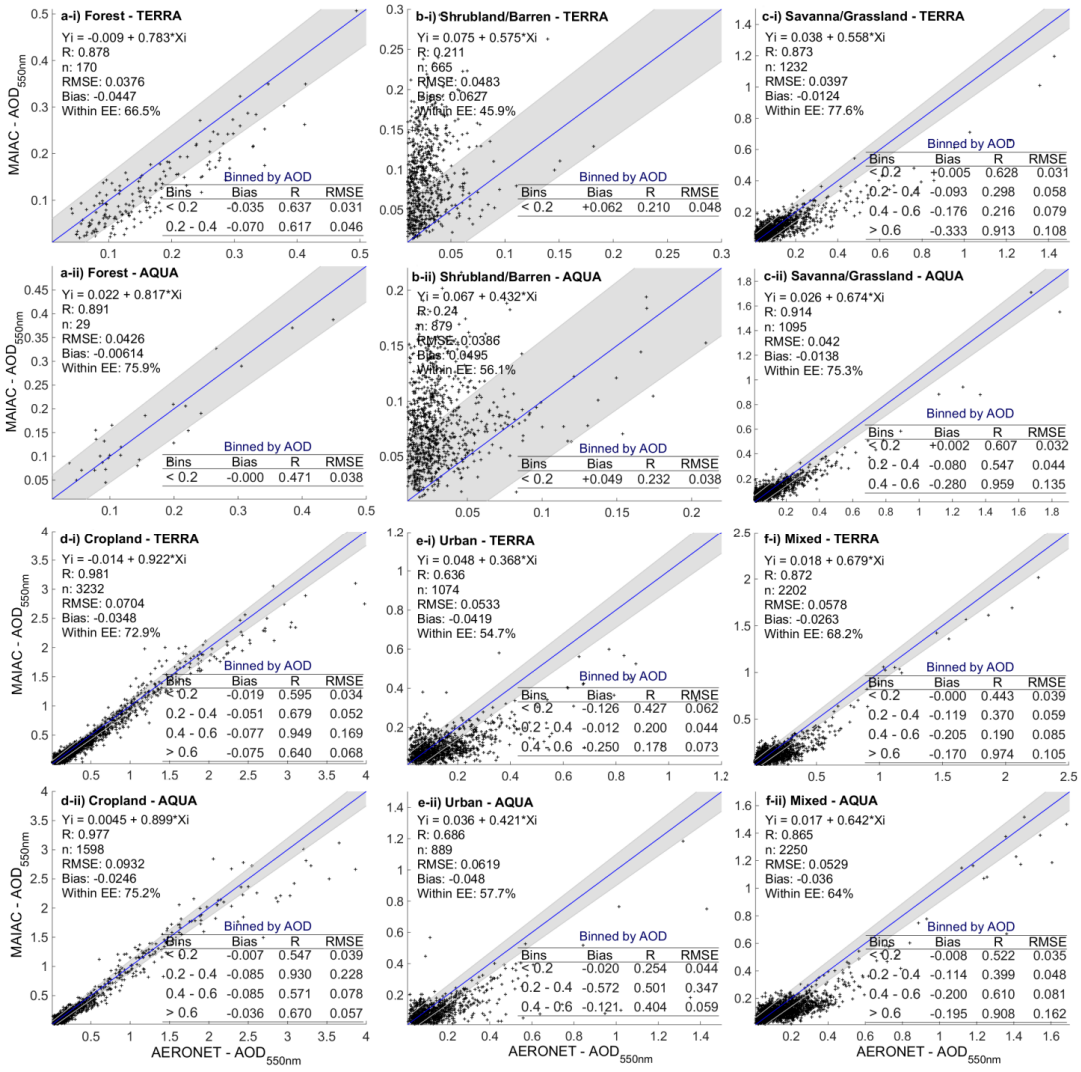

Mixed areas represent all sites without one major land cover type within 25 x 25 km². **Figure 3.8f** shows that MAIAC and AERONET measurements agree well over mixed areas, with the R exceeded 0.85 and mean bias was close to unity ($Bias_{terra}$: -0.026 and $Bias_{Aqua}$: -0.036). The fraction of retrievals within EE_{Terra} of 68.2% and within EE_{Aqua}

of 64% shows that the algorithm succeeded in obtaining satisfactory retrievals (2/3 or 66%) for MAIAC Terra. To understand if a particular mixture of cover types directly influences AOD retrievals, we performed a correlation analysis for each AERONET site with mixed land cover types, as shown in Table 3.5. The results showed an agreement between MAIAC and AERONET measurements with R higher than 0.612 for all sites. Comparing retrievals between sites, Campo Grande and São Martinho showed higher quality retrievals over a mixture of cropland, savanna and grassland covers, with slope and R exceeding 0.72 and fraction of retrievals higher than of 77% within EE for both sensor products. In particular, Belterra site had insufficient number of match-ups due to high cloud cover in the Amazon region, which compromises the consistency of the correlation results. Note that correlation analysis for Arica and La Paz sites showed fair agreement between MAIAC and AERONET AOD_{550}, where the spatial window had more than 30% area covered by shrubland and barren covers. Therefore, AOD retrievals were not directly affected by bright surfaces when the spatial window included other land cover types, especially, dark surfaces. This reasonable accuracy over mixed areas suggests that SRC algorithm is quite efficient for heterogeneous surfaces, even over transition areas, e.g. land and ocean transition over Arica site. Therefore, coastal regions without routine aerosol observations, such as the East Coast of Brazil, benefit with quality MAIAC retrievals.

Table 3.5. Basic statistics of MAIAC retrievals from Terra (first line) and Aqua (second line) compared to AERONET measurements from mixed group.

Mixed group	Sensor	Regression model	R	Within EE (%)	Land Cover (%)					
					Water	Forest	Shrubland /Barren	Savanna/ Grassland	Cropland	Urban
Arica	TERRA	Y = 0.01 + 0.45*X	0.708	20.0	44.15	----	47.33	0.68	0.10	7.74
	AQUA	Y = 0.04 + 0.38*X	0.648	32.7						
Belterra	TERRA	--------	----	----	33.85	39.68	----	2.61	23.87	----
	AQUA	--------	----	----						
Campo Grande	TERRA	Y = 0.02 + 0.84*X	0.980	85.7	----	0.45	----	32.81	37.23	29.50
	AQUA	Y = 0.02 + 0.81*X	0.971	83.2						
La Paz	TERRA	Y = 0.03 + 0.66*X	0.561	83.4	----	----	32.69	42.73	----	24.58
	AQUA	Y = 0.04 + 0.62*X	0.612	86.77						
São Martinho	TERRA	Y = 0.04 + 0.72*X	0.783	77.3	0.29	4.63	0.03	47.27	47.48	0.29
	AQUA	Y = 0.03 + 0.78*X	0.873	86.9						

3.6.3. Impacts of AOD magnitude

The satellite aerosol retrieval improves with higher aerosol contribution to TOA reflectance. Hence, AOD magnitude is a key factor in the confidence and quality of the retrievals. Figure 9 shows the assessment of MAIAC retrievals according to AOD intervals using the correlation coefficient and NRMSE. These two metrics are sufficient to express the agreement and relative error, where the best retrievals are close to R ~1

and NRMSE ~ 0. Our analysis used the aerosol regimes broken down into AOD intervals: low (0.01 - 0.2), moderate (0.2 - 0.4), moderate-high (0.4 - 0.6) and high (>0.6) AOD values.

In general, our results pointed out that MAIAC and AERONET AOD_{550} correlation decreases when the AOD values decline for the same land cover. On clear days (AOD<0.2), we found the critical correlation (<0.3) and high NRMSE (>1.2) over shrubland and barren areas, due to inherent difficulty in decouple surface and aerosol contributions at low AOD. Thus, two reasons emerge from our results: (i) TOA reflectance is less sensitive to aerosol loading over a bright surface, and (ii) satellite retrievals at low AOD values are more susceptible to background surface noises. Fraser and Kaufman (1985) introduced the implications of surface reflectance and aerosol absorption to satellite AOD retrievals. The authors described surface reflectance with no variation in TOA reflectance to AOD changes, as critical surface reflectance (CSR). Based on that, aerosol loading has distinct effects in TOA reflectance according to surface reflectance, where the aerosol effects increase TOA reflectance over the dark surface and decrease over the bright surface. In the same way, Hsu et al. (2004) demonstrated that the TOA reflectance is not sensitive to AOD changes over bright surfaces due to the predominance of aerosol absorption. Therefore, the land cover areas with surface reflectance close to CSR, as urban and desert areas, imply less or no sensitivity to aerosol effects in TOA reflectance. Moreover, Seidel and Popp (2012) also showed significant errors of AOD retrievals when the surface reflectance is close to CSR, when 0.01 uncertainty of surface reflectance introduces at least 0.1 error in AOD retrieval. In our study, the poorest results over urban and desert areas might be associated with inaccuracies of surface characterization, and consequently, background effects in AOD retrievals. Conversely, dark surfaces increase aerosol sensitivity due to lower reflectance than CSR. Thus, both products presented better correlation over vegetated areas than that over bright surfaces at low AOD values, and Terra retrievals showed a slightly better correlation than that of Aqua over forest and cropland areas.

Next, the moderate/moderate-high AOD interval (0.2–0.6) led to higher correlations for all covers compared to low AOD results. The agreement for moderate AOD values benefit MAIAC applications over distinct regions, since almost all AERONET sites showed average AOD close to 0.2 (Table 3.3). At high AOD values, correlation analysis showed the clustering of land cover results in low NRMSE (< 0.2), and high R (>0.9), with exception for urban retrievals. The multiple scattering regimes of high AOD increase aerosol contribution to TOA reflectance and, consequently, reduce the impacts of surface background. In summary, MAIAC retrievals presented satisfactory correlations for moderate and high AOD (> 0.2) over forest, cropland, savanna and grassland areas. For comparison of Terra and Aqua products, the accuracy of both MAIAC products was quite similar over all AOD range. In applications at low AOD

values, a caution should be exercised over bright surfaces, as presented for shrubland and barren areas.

Figure 3.9. Correlation analysis of AOD intervals using normalized RMSE versus correlation coefficient. Note the discontinuity in NRMSE-axis. At least 15 match-ups were required to perform this correlation analysis.

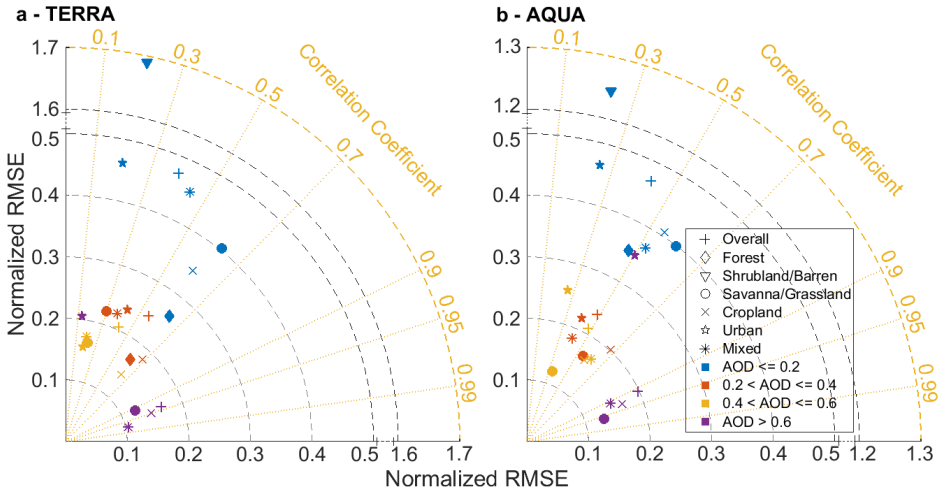

3.6.4. Impacts of seasonal variability on AOD retrievals

Seasonal analysis of aerosol distribution over South America supports temporal evaluation of MAIAC retrievals. Figure 3.10 shows the spatial distribution of mean AOD_{550} from $MAIAC_{Terra}$ (2000-2015) for seasonal timescales: DJF (December, January and February), MAM (March, April and May), JJA (June, July and August) and SON (September, October and November). In general, South America has the aerosol patterns driven by three main continental aerosol types: biomass burning, mineral dust and urban pollution.

During the austral winter season (SON), the emissions from local fires increase atmospheric turbidity and contribute to strong aerosol seasonality over South America. In the March-April-May season, fire practices are regularly used to open landscapes for agriculture and pasture areas in Colombia, Ecuador, and Venezuela (VIDELA et al., 2013). The dry season is the critical aerosol period for biomass burning emissions in central-western Brazil. From Abraços Hill and Alta Floresta sites (Table 3.1), it is observed that seasonal aerosol changes from low AOD during MAM season (0.084±0.05 and 0.076±0.037, respectively) to ~ 6 times higher in the SON season (0.551±0.414 and 0.571±0.525, respectively). Particularly, September is a dry peak and the most critical month for air quality in central South America, where the maximum AOD reaches 3.1 in the Abraços Hill and 4.72 in the Alta Floresta site. Furthermore,

later dry season in northwestern South America delays the onset of the burning season, with drastically change of aerosol loading in DJF season (SCHAFER et al., 2008).

In the desert and arid regions, mineral particles are suspended and transported into the atmosphere due to dust and sand storms, as observed in Atacama and Patagonia deserts (GINOUX et al., 2012). In the first half of the year, Casleo site records typical low AOD_{550} (0.023±0.014) and high mixture of fine and coarse-mode particles ($\alpha_{440\text{-}670}$: 1.3 ± 0.9, see Figure 3.4) during windblown dust in the central region of Patagonia desert. In the DJF period, high amounts of mineral particles are transported from Sahara desert to the Caribbean region and the Northeastern Brazil, which annually changes the atmosphere burden in these regions (KAUFMAN et al., 2005).

Figure 3.10. Spatial distribution of average MAIAC AOD_{550} within 2000-2015 for seasonal timescales: DJF (December-January–February), MAM (March-April–May), JJA (June-July–August) and SON (September-October–November). At least 15 match-ups of MAIAC vs. AERONET measurements were used to compute correlation coefficient per season.

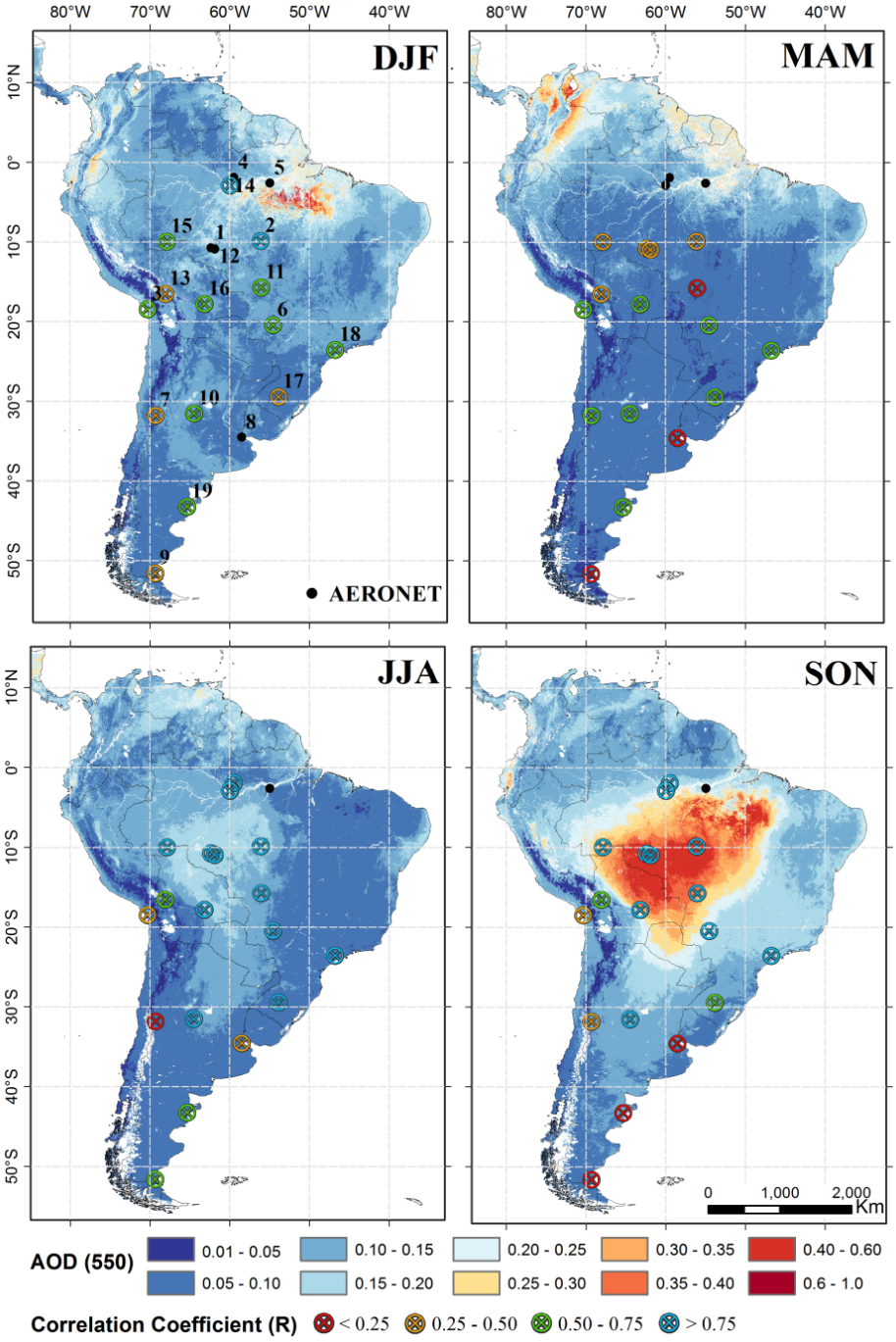

Air pollution is a health issue over most populated cities in South America, such as São Paulo, Buenos Aires and Santiago (BELL et al., 2006). The industrial pollution and fossil fuel combustion influence the local climate and atmospheric turbidity over these cities. In Sao Paulo site, the smoke plumes increased AOD_{550} by about 1.6 times from the first half of the year (0.167±0.099) to the austral spring (0.268±0.185). Air quality control for these big cities demands routine observation of fine particulate matter emissions that are potentially predicted by satellite AOD products (CHUDNOVSKY et al., 2013).

Since sun photometer measurements are the primary benchmark for evaluating satellite aerosol retrievals, an extensive coverage is useful for quality assurance. Figure 3.10 showed that the Northwestern and Eastern regions still lack the long-term monitoring by AERONET sites, and aerosol microphysical assumptions may be an issue over these regions. Furthermore, the complex topography of the Andes Mountains, located in West South America, represents a challenge surface feature for AOD retrievals and also limits the establishing of continuous aerosol observations. Shi et al. (2011) identified high AOD biases between MODIS and MISR products over complex surface features, as the Andes Mountains and the West Coast of the US. Although some regions have scarce ground-based observations, the selected AERONET sites are located in regions sensitive to seasonal aerosol records, and validation of MAIAC retrievals using those measurements allowed a critical assessment over different aerosol sources and surface context.

Table 3.6 presents the statistical indicators (bias, R and fraction within EE) of MAIAC vs. AERONET AOD_{550} for quarter seasons (DJF, MAM, JJA, SON). In general, MAIAC retrievals were sensitive to seasonal aerosol loading over South America and the overall correlation was higher for the second half of the year (JJA and SON) than that for the first half of the year (Table 3.6a). In comparison, both sensor products showed a quite similar correlation throughout the seasons, although it is rather instructive to consider the quality difference between Terra and Aqua products. As discussed by Hoelzemann et al. [2009] and observed in Figure 3.10, the austral winter (SON) is a critical period to burning events and accurate retrievals in the second half of

the year enable fine-scale monitoring of smoke plumes over cropland, savanna and grassland areas (Table 3.6d and 3.6e). So, our results show that a good performance of MAIAC retrievals benefit the biomass burning studies related to extreme aerosol regimes over South America, with R close to unity for both product (R of ~0.975 over cropland); although the fraction of retrievals within EE was lower than 66% in the SON season for both sensors. Similarly, MAIAC retrievals over urban areas showed a relative high R (Terra: 0.779 and Aqua: 0.814) during the winter season (Table 3.6f) and absolute bias lower than 0.1 for all seasons. Furthermore, Aqua retrievals have a higher EE than those of Terra in the urban area, and aerosol applications might consider to use this sensor product in urban air pollution studies. In shrubland and barren areas,

Table 3.6c shows that correlation parameters also vary seasonally and retrievals during the first half of the year had a better agreement than those of the second half. However, variability of aerosol regime over these areas does not provide an increase in MAIAC accuracy, since Atacama and Patagonia deserts have a typical low AOD patterns throughout the year (Table 3.3). In particular for forest areas (Table 3.6b), the high cloud cover on the Amazon rainforest region during the first semester limited the number of match-ups, and does not guarantee the consistency of the analysis. For the austral winter, MAIAC retrievals showed relative high confidence level over forest areas with R close to unity (R ~ 0.92). In summary, although overall validation in Figure 5 reported the satisfactory accuracy of AOD retrievals following new expected error (Eq. 3.3), this temporal analysis stratified by land cover type shows that level of algorithm performance also varies with timescale seasons.

Table 3.6. Temporal assessment of MAIAC products for seasons: DJF (December–February), MAM (March–May), JJA (June–August) and SON (September–November). For each season, first line is of Terra retrievals (shaded gray) and second line is of Aqua retrievals.

		(a) Overall			(b) Forest			(c) Shrubland/Barren		
Period		Bias	R	EE (%)	Bias	R	EE (%)	Bias	R	EE (%)
DJF	TERRA	-0.01	0.580	62.17	-0.033	0.927	81.25	0.063	0.250	47.03
	AQUA	0.004	0.598	61.39	n*	n*	n*	0.057	0.231	54.76
MAM	TERRA	-0.016	0.528	71.16	n*	n*	n*	0.050	0.248	52.97
	AQUA	-0.008	0.579	72.61	n*	n*	n*	0.040	0.165	67.70
JJA	TERRA	-0.024	0.960	75.2	-0.040	0.913	75.29	0.056	0.035	49.18
	AQUA	-0.029	0.932	70.82	-0.001	0.930	88.23	0.041	0.142	58.02
SON	TERRA	-0.034	0.971	57.39	-0.061	0.799	46.55	0.081	0.096	34.68
	AQUA	-0.028	0.968	58.52	n*	n*	n*	0.059	0.136	41.83

		(d) Savanna/Grassland			(e) Cropland			(f) Urban		
Period		Bias	R	EE (%)	Bias	R	EE (%)	Bias	R	EE (%)
DJF	TERRA	-0.012	0.688	77.78	0.003	0.715	78.81	-0.016	0.200	58.72
	AQUA	-0.003	0.639	74.24	0.027	0.494	65.00	-0.018	0.117	58.47
MAM	TERRA	-0.001	0.684	87.07	-0.015	0.183	77.67	-0.03	0.539	66.79
	AQUA	-0.006	0.679	82.24	-0.006	0.112	75.86	-0.034	0.299	68.91
JJA	TERRA	-0.006	0.914	75.91	-0.03	0.981	78.52	-0.059	0.572	47.33
	AQUA	-0.015	0.930	76.69	-0.02	0.977	83.04	-0.073	0.694	52.16
SON	TERRA	-0.027	0.882	71.23	-0.065	0.979	56.34	-0.055	0.779	47.52
	AQUA	-0.025	0.932	69.59	-0.055	0.973	57.10	-0.041	0.814	55.90

n*: Insufficient number of match-ups.

3.6.5. Time series validation

As MODIS missions exceed their designed lifetime of 6-year, MODIS Characterization Support Team (MCST) have been sustaining efforts to monitor the instrument performance and maintain well-calibrated MODIS data throughout the entire mission (XIONG et al., 2016). The calibration issues, spacecraft operation, solar diffuser degradation, and non-functional detectors are revised constantly to guarantee the stable calibration and consistence of data records (TOLLER et al., 2013). Due to calibration updates, Collection 6 MODIS L1B data record promises overcome the long-term calibration artifacts in both MODIS Terra and Aqua (XIONG et al., 2016; LYAPUSTIN et al., 2014a). So, regarding the concerns with temporal MODIS residual drift in AOD retrievals (e.g. see Section 6.3 in Levy et al. (2015)), we provide an annual bias analysis to assess the harmonization of two MODIS instruments during mission lifetime. **Figure 3.11** presents the time series validation of Terra and Aqua retrievals within 2002-2015. To reduce the aerosol diurnal variations and surface change properties, we selected only

match-ups of MAIAC and AERONET measurements acquired on the same day for both sensors (Table 3.7).

Our results show that AOD bias per year remains quite similar between Terra and Aqua in 15-year period (offset of ~0.006) with minimal temporal dependence in its trend (MAE lower than 0.027). Note that the minimum offset was expected for AOD retrievals from twin MODIS sensors, while AOD biases vary according to surface-atmosphere condition in time series. For example, Aragão et al. (2014) shows that fire events and their intensity increase during drought years (e.g. El Nino years), such as 2007, 2010 and 2015. On these years of high AOD, MAIAC shows a negative bias, consistently with our analysis above, and no trend. On the regular years, the statistics is dominated by lower AOD and the surface-related contribution with lower cloudiness, where MAIAC shows a positive bias. A small apparent increase in AOD bias during 2011-2014 may be an artifact caused by reduced biomass burning in regular years, both moving MAIAC AOD bias in the positive direction. As a conclusion, this analysis shows a good cross-calibration between MODIS Terra and Aqua (LYAPUSTIN et al., 2014a), resulting in consistent AOD products, and general lack of trend over 14-year period. If any residual calibration trend exists, it should not exceed ~0.03 AOD over 14 years. Sayer et al. (2013) compared the performance of Deep Blue algorithm between C5 and C6 and also reported improvements in AOD retrievals using C6 calibration.

Table 3.7. Long-term AERONET sites used in time series validation.

AERONET sites	LAT	LONG	Match-ups*	Period
Alta Floresta, Brazil	9.87° S	56.1° W	448	1993-2016
Campo Grande Sonda, Brazil	20.43° S	54.59° W	491	2003-2016
Casleo, Argentina	31.79° S	69.30° W	548	2011-2014
Ceilap BA, Argentina	34.56° S	58.50° W	600	1995-2016
Cordoba CETT, Argentina	31.52° S	64.46° W	752	1994-2010
Cuiaba Miranda, Brazil	15.72° S	56.02° W	763	2001-2016
Rio Branco, Brazil	9.95° S	67.86° W	201	1994-2016
São Paulo	23.56° S	46.73° W	399	2000-2016

*Only match-ups from the same day for both MODIS sensors.

Figure 3.11. Intercomparison of MAIAC Terra vs Aqua AOD retrievals in time series validation. The sample size (n) per year used to bias calculation and MAE is the mean absolute error (MAE).

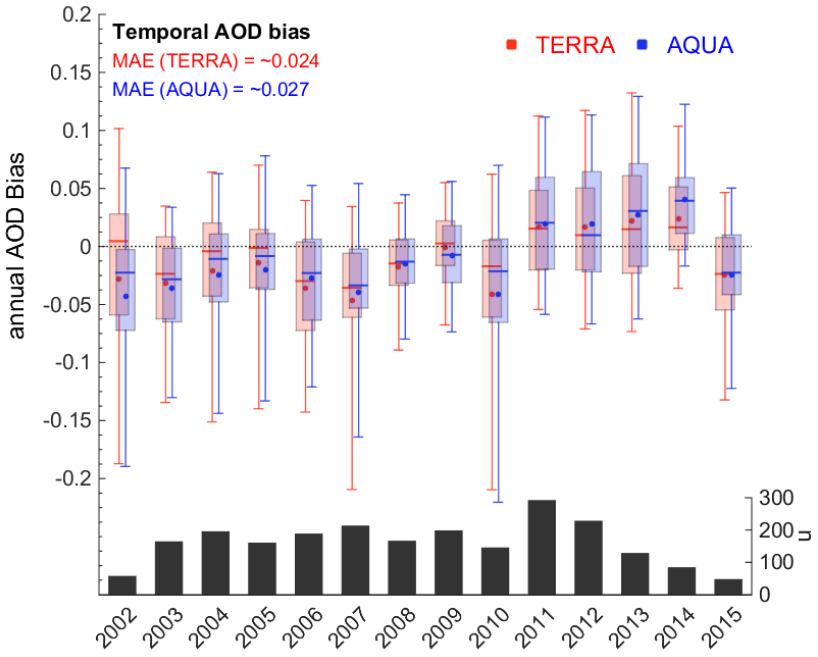

3.7. Conclusion

In the present study, we compared the AOD_{550} retrievals from MAIAC and 19 AERONET sites over South America within a 15-year period (2000-2015). The validation dataset includes a typical interval of AOD between 0.01 and 4.0, with average of 0.177. This dataset presented AOD records from multiple aerosol sources, such as biomass burning, desert dust, and urban pollution. The MAIAC AOD product from Terra and Aqua presented similar quality retrieval and the overall comparison with ground-based measurements showed a good correlation for both products, with bias up to -0.023 and R close to unity (~0.95). For comparison, these results slightly improve on MOD04 Collection 6 dataset, however the lower relative error in EE envelope (EE= ±(0.05*AOD +0.05)) and high 1 km resolution represent an advantage to fine-scale applications compared to MOD04 resolution (DT-land at 3 and 10 km [Remer et al., 2013]).

Algorithm performance was analyzed as a function of the land cover type. MAIAC retrievals showed better agreements with AERONET measurements over forest, savanna, grassland, cropland and mixed areas, with fraction of AOD retrieval within EE varying from 64 to 77.6%, and R exceeding 0.86 for both products. In contrast, MAIAC retrievals over bright surfaces were poorer than those over vegetated areas, with fraction within EE varying from 45.9 to 57.7% and R between 0.21 and 0.686. Indeed, these results are expected due to inherent difficulty to decouple surface-atmosphere signals at high surface reflectance and low AOD regimes. Additional correlation analysis over mixed areas showed a satisfactory accuracy for MAIAC retrievals (R: 0.561 - 0.980), even with bright surface contributions around the sites (e.g. Arica and La Paz sites). Thus, our results suggest that MAIAC algorithm performed well over heterogeneous surfaces and the mixture of cover types attenuates the impact of bright surface contributions. Besides land cover types, AOD magnitude influences on quality of MAIAC retrievals. Our analysis showed better confidence for AOD higher than 0.2 values, while the low AOD (<0.2) requires an operational filter to remove some high AOD values, particularly, over bright surfaces. Seasonal aerosol distribution defines distinctive periods over South America and reasonable MAIAC retrievals in the second half of the year benefit several aerosol applications during critical biomass burning season. In the time series validation, the low offset (~0.006) between Terra and Aqua retrievals shows a temporal stability of MAIAC C6 products. If there is any residual trend from calibration (after major MODIS C6 trends were removed), it is not expected to exceed approximately 0.03 error in 14 years.

Finally, MAIAC algorithm offers a new perspective for consistent AOD retrieval at 1 km resolution using explicit surface characterization in terms of spectral BRDF and spectral reflectance ratios. A prior information of surface properties from MODIS time series promises overcome constraints imposed by empirical assumptions used by standard aerosol algorithms. A Comprehensive validation of new multi-angle MODIS product supports aerosol studies over South America and we recommend an extensive MAIAC validation over other regions in the world.

4 SEASONAL PATTERN OF CLOUD COVER AND ATMOSPHERIC CONSTITUENTS AND ITS IMPLICATIONS FOR OPTICAL REMOTE SENSING

4.1. Introdution

The Amazon rainforest plays a fundamental role in the Earth's climate functioning. In the last decades, several studies provide insights of Amazon processes and their feedback on the regional and Earth system: climate change in the Amazon ecosystem (MALHI et al., 2008; NOBRE et al., 2016), vegetation function and traits (HILKER et al., 2015), Amazon transition of land-use (DAVIDSON et al., 2012), the role of deforestation and fire events in the carbon budget (BACCINI et al., 2012; ARAGÃO et al., 2014), and hydrological processes (MARENGO; ESPINOZA, 2016). Advances of remote sensing contribute on viable means to large-scale coverage and continuous monitoring of the tropical ecosystems (CHAMBERS et al., 2007). The current free availability of satellite imagery allows integration of multi-sensors and time-series analysis from local to global scales. However, although the remote sensing data offers a synoptic view of the surface dynamics (BARBOSA et al., 2015), the top-of-atmosphere (TOA) signal measured by satellite sensors is not only dependent of the surface properties but is often distorted by the atmospheric effects (VERMOTE; KOTCHENOVA, 2008; OKIN and GU, 2015).

The atmospheric scattering and absorption of solar radiation impose constraints on the quality of surface reflectance retrieval and require an accurate correction to maintain the consistence of scientific data (FENG et al., 2013). Since most of high-resolution satellite sensors was not designed with useful spectral bands to atmospheric data retrieval, information input for atmospheric correction is often derived from local ground-measurements or from moderate and course-resolution satellite products, such as the MODIS and MISR sensors (PETRENKO et al., 2012). While the ground-data is often scarce in the Amazon region, such satellite products have the potential for filling the gap with information needed for carrying out physically based atmospheric

correction, enhancing our understanding of the spatiotemporal dynamics of key atmospheric constituents.

In the Amazon ecosystem, seasonal variability of key atmospheric constituents, such as cloud cover, aerosols, water vapor, and ozone, represents a challenge factor for passive remote sensing: high cloud cover and atmospheric bias. Asner (2001) studied the probability of cloud-free images using the Landsat archive (1984 – 1997) and reported the severe limitation imposed by cloud cover to monthly surface observations, especially, in the northern Amazon. While cloudiness extension reduces the frequency of cloud-free pixels, annual and inter-annual variability of atmospheric constituents modifies multispectral data seasonally. Recently, Hilker et al. (2012) reported that uncertainties in the atmospheric correction procedures and cloud screening have notable effects on the current MODIS surface reflectance product. The authors also reported that wet season (high cloud cover) and dry season (aerosol dependence) increase noise levels of the Normalized Difference Vegetation Index (NDVI), factor of up to 10, due to data processing technique and atmospheric bias. In this context, Amazon monitoring requires further comprehension of the atmospheric feedback and their implications for optical remote sensing applications, such as cloudy seasons, atmospheric condition (clean and turbid), and typical concentration range of atmospheric constituents.

In this chapter, we evaluate the annual and inter-annual variability of cloud cover fraction and key atmospheric constituents, such as aerosol, water vapor, and ozone content, using a 15-year MODIS atmospheric products in the Amazon basin. The implications for remote sensing applications are discussed for various satellite sensors using sensitivity analysis of the atmospheric scattering and gaseous transmittance. Below, we review the mechanisms of atmospheric dynamic in the Amazon basin and as they affect atmospheric correction.

4.2. Background

Tropical atmosphere presents particular features that include intense convective activity, strong heating gradient and global climate forces controlling the regional circulation (EMCK, 2007; NOBRE et al., 2009). Rainforest's evapotranspiration and moisture

inflow from the Atlantic Ocean are significant drivers for water recycling in the region (BOERS et al., 2017). The easterly moisture-laden air is blocked in the eastern slope of central Andes Mountains (0° – 10° S) (GARREAUD, 2009), originating the South America low-level jet (SALLJ) that transports moisture content towards the subtropical latitudes (VERA et al., 2006). In the austral summer (DJF), South American Summer Monsoon (SASM) causes an intense precipitation regime and its extension into the South Atlantic Convergence Zone (SACZ) intensifies the transient moisture flux from southwestern Amazon toward western subtropical Atlantic Ocean (CARVALHO et al., 2004; VUILLE et al., 2012). Nonetheless, monsoon systems are extremely sensitive to mesoscale convective forces and ocean-atmosphere system. For instance, Pacific sea surface temperature (SST) variation controls the so-called El Niño–Southern Oscillation (ENSO) events (Niño 3.4 at 5°N to 5°S latitude and 120° to 170°W longitude) (GRIMM; TEDESCHI, 2009; GRIMM, 2011). In most recent 2015 drought, warming eastern Pacific episode (El Niño) suppressed convection patterns in northern and eastern Amazonia and produced a severe drought and warming over most part of Amazon (JIMÉNEZ-MUÑOZ et al., 2016).

Although extreme phases of ENSO modulate weather conditions and hydrology processes in the region, it is not a single mechanism controlling the inter-annual variability of precipitation regimes. The tropical Atlantic SST gradient exerts a strong regional influence on drought episodes: the warming of the tropical North Atlantic shifts the Intertropical convergence zone (ITCZ) to northward position and reduces moisture transport into Amazon, mostly in the northern and central regions (GRODSKY; CARTON, 2003; SIERRA et al., 2015). For instance, the 2005 Amazon drought was only associated with warm tropical North Atlantic that affected part of southwestern Amazonia (MARENGO et al., 2008). Therefore, extreme droughts in Amazon region are linked with (i) occurrence of El Niño episodes; (ii) strong warm of SST in tropical North Atlantic; or (iii) both events (MARENGO; ESPINOZA, 2016), see references therein).

Precipitation regimes can be directly linked to cloudiness extension, and consequently, spatiotemporal variability of cloud cover in satellite images. Persistent cloud cover

limits the surface observation blocking the solar radiation reflected from the Earth's surface and so makes optical remote sensing useless. In addition, adjacency effects near cloud boundaries or undetectable cirrus cloud distort target reflectance (KOREN et al., 2007; MARSHAK et al., 2008). Gomis-Cebolla et al. (2016) emphasized the importance of cloud mask schemes to minimize cloud contamination and increase the number of cloud-free pixels in MODIS data over Amazon rainforest. In this sense, regional dry-season might be a reasonable period to avoid high cloud cover and cloud screening in the satellite images. However, fire emissions increase drastically the atmosphere burden with extensive smoke plume across southern Amazon during dry-season (HOELZEMANN et al., 2009). The spread pattern of fires induced by human activities and wildfire co-occurs in the extreme drought episodes, mostly over forest edges and deforested areas (ARAGÃO et al., 2008; WIEDINMYER, 2015). While forest fire degrades the primary forest structure with tree mortality (BARLOW; PERES, 2008), the atmospheric composition also suffers substantial alterations caused by co-emission of trace gases - including nitrogen oxides (NO_x), volatile organic compounds (VOCs), carbon dioxide (CO_2) and methane (CH_4) (ANDREAE; MERLET, 2001). These reactive trace gases are precursors of photochemical reactions in tropospheric ozone (O_3) formation (ROYAL SOCIETY, 2008; ZIEMKE et al., 2009; AKAGI et al., 2011; JAFFE; WIGDER, 2012). Beyond the large natural biogenic emission e.g. biogenic VOCs, the perturbation of these emissions causes the net increase of seasonal tropospheric O3 burden (KARL et al., 2007; PACIFICO et al., 2015). In summary, there is a clear atmospheric dynamic associated with the precipitation regime and land use processes. Due to light attenuation caused by atmospheric constituents (KONDRATYEV et al., 1992), the aerosol burden, atmospheric moisture, and columnar ozone content are key atmospheric information to optical remote sensing, and for this reason, their spatial and temporal dynamic is important for satellite applications.

Quantitative analysis of the Earth’s surface requires radiometric calibration to physical quantities, as spectral radiance or reflectance (CHANDER et al., 2009). Since biophysical analysis often applies the surface reflectance as primary information, the atmospheric effects on solar radiation need to be removed from TOA measurements

(VERMOTE; KOTCHENOVA, 2008). Atmospheric correction can be performed by radiative transfer (RT) models, such as 6SV, MODTRAN, LOWTRAN (Low Resolution Atmospheric Transmission Model). The RT models provide physical-optical description of atmospheric attenuation to compute the molecular and aerosols scattering, and gaseous absorption, such as water vapor, ozone, dioxide of carbon and oxygen (MISHCHENKO, 2008; KONDRATYEV et al., 1992). In this context, 6SV model is widely used RT model that provide atmospheric optical framework to propagate radiation through atmosphere and TOA reflectance can be estimated following the Equation 2.15 (see in Section 2) (VERMOTE et al., 1997b).

While some variables – sun-view geometry, scene location, acquisition date and surface elevation - can be easily accessed on ancillary data, high variable atmospheric constituents requires additional data source, such as meteorological station, sun photometers records, and/or satellite atmospheric products (HOLBEN et al., 1998). In Amazon region, the Amazon Tall Tower Observatory (ATTO) and AERONET sites are examples of scientific efforts to continuous monitoring climate variables. However, the network of these ground-based data remains limited over almost regions, and its dataset is not often synchronized to satellite overpass. Since traditional ground-based data lacks in either temporal and spatial scales, satellite products present an only viable means to offer repeatability and coverage for atmospheric correction applications. Therefore, this work provides an overview, regional and sub-basin analysis of Amazon atmospheric constituents, and then, discuss the implication of atmospheric effects in various satellite sensors.

4.3. Data and methods

4.3.1. MAIAC

MODIS instrument on board of Terra (10:30 am) and Aqua (1:30 pm) platforms delivers historical Earth observation data series from March 2000 and May 2002, respectively (SALOMONSON et al., 1989). These instruments have been fostering numerous scientific studies of the Amazon due to the long-term dataset, high-temporal revisit (near-daily), wide-swath (2300 km), and 36 spectral channels devoted to the

land-atmosphere monitoring. The success of the MODIS land-atmosphere products is most associated with the continuous efforts to provide high-quality data for scientific insights. In this sense, the generic MAIAC algorithm was developed for MODIS data using time series approach and image-based processing (LYAPUSTIN et al., 2011; 2012). The algorithm derives the surface BRF and suite of atmospheric products: internal cloud mask, AOD at 470 and 550 nm, column water vapor (or Total Precipitable Water, TPW). For more information, see Lyapustin et al. (2008; 2011; 2012).

This study uses 12 MAIAC tiles over the Amazon basin (6°N to 20°S latitude and 80°W to 49°W longitude) acquired from the Terra platform within 2000 - 2015 period. Our current MAIAC dataset contains ~96000 images with valuable atmospheric information: AOD at 550 nm (unitless), TPW ($g.cm^{-2}$), and 1 km resolution cloud mask. Image processing includes the mosaic and re-projection of all MAIAC tiles. Briefly, internal cloud scheme employs an integration of clear-sky image, as reference, and uses covariance analysis for change detection (LYAPUSTIN et al., 2008). MAIAC product has a quality assurance (QA) layer with internal cloud mask and Land-Water-Snow classification. MAIAC scheme has advantage of time series accumulation of sequential observations that provides prior information at multi-angle views and fine-scale atmospheric products. In this context, comparison of MAIAC atmospheric retrievals with ground-measurements provides useful evidence of reliability of this new dataset to support atmospheric studies and RT models.

AERONET (http://aeronet.gsfc.nasa.gov) is a global network of ground-based sun photometers for aerosol monitoring (HOLBEN et al., 1998). Direct solar measurements allow derivation of AOD at seven wavelengths within 340-1020 nm and accuracy of ± 0.02 (ECK et al., 1999). The TPW is also provided by AERONET measurements derived from the channel 940 nm (SCHMID et al., 1996). In this study, we compare MAIAC AOD and TPW retrievals with AERONET Level 2.0 measurements within 2010 - 2015: Manaus-Embrapa (2.89° S latitude, 59.96° W longitude) and Rio Branco (9.95° S latitude, 67.86° W longitude) (**Figure 4.1**). Here, AERONET AOD was interpolated to 550 nm using quadratic fits on a log-log scale (ECK et al., 1999). The

averaged MAIAC values within 25 x 25 km² box centered at site were compared with AERONET measurements taken within ±30 min of satellite overpass. The full validation of MAIAC AOD across the South America is reported by Martins et al. (2017).

Figure 4.1. The Amazon basin. AERONET sites used to validate MAIAC atmospheric observations: Manaus-Embrapa (2.89°S, 59.96°W) and Rio Branco (9.95°S, 67.86° W).

4.3.2. MOD08 ozone

MOD08 Level-3 is an atmospheric gridded product at 1° x 1° cells designed to derive statistics, e.g. mean, maximum, minimum and standard deviation, from Level-2 atmosphere products (MOD08 Terra and MYD08 Aqua). Therefore, the MOD08 is actually the subset statistics from the MOD04 (aerosol), MOD05 (precipitable water), MOD06 (cloud properties), MOD07 (atmospheric profiles) products (HUBANKS et al., 2015). This scientific data is available at three time intervals: D3 for daily, E3 for eight-day, and M3 for monthly. In this study, we used the Collection 6 MOD08 D3 product from 2000 to 2015 available at ftp://ladsweb.nascom.nasa.gov/allData/6/MOD08_D3/. The ozone content was extracted from (i) "Total_Ozone_Mean" layer; (ii) rescaled by 0.1 factor to Dobson units; and (iii) and resampled to 1 km resolution.

The algorithm of total-column ozone content (tropospheric and stratospheric) employs primary information of MODIS channel 30 (9.6 μm) to solve the radiative-transfer

equation and performs the statistical regression with vertical profiles of atmospheric (BORBAS et al., 2011; SEEMANN et al., 2003). Borbas et al. (2011) compared the MODIS total column ozone retrievals with surface Brewer measurements in 2007 at Budapest, Hungary, and reported RMSE of 31.6 DU and coefficient of determination (R^2) of 0.76 between satellite and ground data. More information on algorithm description is available at Algorithm Theoretical Basis Documents (available at https://modis.gsfc.nasa.gov/data/atbd/atbd_mod07.pdf).

4.3.3. Spatiotemporal Analysis

The historical and full spatial dataset over the Amazon basin allow image processing with different timescales and geographic coverage (**Figure 4.2**). We derived a time-series based on data averaged in all Amazon pixels at 1 km resolution. Calculating the frequency of cloud cover per pixel, we generated the fraction of cloud cover at different timescales (quarters and monthly). To consider the spatial heterogeneity of atmospheric feedback, two spatial-scales of observation were defined across the Amazon: (i) four regions, hereafter AMZ; and (ii) six sub-basins divided between North and South of the Amazon river. In addition to averaged data, seasonal pattern of constituents was extracted from BFAST (Breaks For Additive Season and Trend) (Verbesselt et al., 2010) and quarterly bias ($\Delta\delta_{qrt}$) calculated to evaluate changes in the mean pattern during the period 2000-2015 (Equation 4.1):

$$\Delta\delta_{qrt} = \mu_{qrt,year} - \langle\mu_{qrt}\rangle_{2000\text{-}2015} \quad (4.1)$$

Where, μ is the atmospheric variable, $\mu_{qrt,y}$ is the average of variable for each quarter (qrt = DJF, MAM, JJA, SON) in the year (y = 2000, 2001,…, 2014, 2015); $\langle\mu_{qrt}\rangle_{2000\text{-}2015}$ is the average of quarter (qrt) over the multi-year dataset (2000-2015), respectively. Since the $\Delta\delta_{qrt}$ suggests the variable oscillation from its mean pattern (**Table 4.2**), high and low $\Delta\delta$ values represent most critical variable peak.

Amazon regions (AMZs) incorporate a climatology context in the atmospheric constituent analysis. The location of AMZs regions was based on the average of annual cumulative rainfall from the Tropical Rainfall Measuring Mission (TRMM) 3B43 v7

monthly product at 0.25° spatial resolution (HUFFMAN et al. 2007). Thus, four equal-regions are located across the Amazon basin: Northwestern (AMZ1), Central (AMZ2), Northeastern (AMZ3) and Southern (AMZ4). In addition to these regions, six Amazon sub-basins were also selected regarding environmental context: Napo-Putumayo-Javari, Negro, Paru-Jari basin in the Northern; and High-Madeira, Low-Madeira and Tapajos basin in the Southern Amazon. Supplemental material includes the same seasonal analysis for all Amazon sub-basins (monthly average and standard deviation).

Figure 4.2. Block diagram of spatiotemporal analysis of 15-year MODIS atmospheric dataset: fraction of cloud cover (FCLOUD in percentage); aerosol optical depth at 550 nm ($AOD_{550\ nm}$ unitless); total precipitable water (TPW in $g.cm^{-2}$); total columnar ozone (TOZ in Dobson Units).

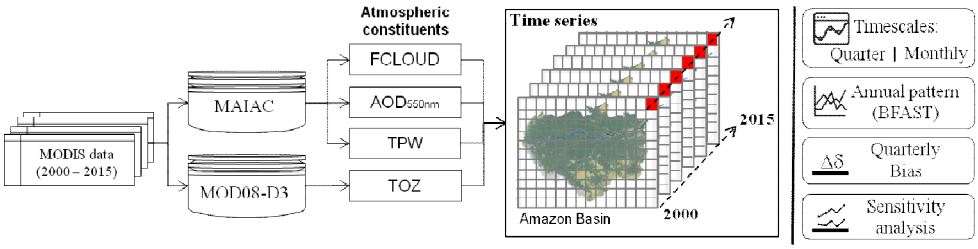

4.3.4. Sensitivity analysis to atmospheric constituents: Transmittance and Scattering effects

Satellite remote sensing is complex in nature and bounded by intrinsic uncertainties on measurements, such as sensor noise, radiometric calibration and atmospheric distortions (OKIN and GU, 2015). To investigate the atmospheric effects on optical remote sensing, we performed a sensitivity analysis using 6SV model to compute the gaseous transmittance (T) and atmospheric intrinsic reflectance (Rayleigh + Aerosol scattering) (VERMOTE et al., 1997b; KOTCHENOVA et al., 2006). Different concentrations of aerosol loading, water vapor, and ozone content were simulated in 6SV model for various satellite optical sensors (sensor/platform): MSI/Sentinel-2, OLI/Landsat-8, MUX/CBERS-4, WFI/CBERS-4, MODIS/Terra. At this point, we adapted 6SV model to the sensor's response functions, and then, run in a loop over those pre-defined concentrations (**Table 4.1**). Note that some parameters were kept constant in sensitivity analysis, e.g. sun-view geometry, atmospheric model

(US62), and aerosol type (Continental). While one atmospheric parameter is simulated in the loop of concentration, the other two constituents were changed to zero.

Table 4.1. Input parameters and their description of the simulation conditions.

Parameters	
Solar zenith angle (θ_0)	30°
Solar azimuth angle (φ_0)	180°
Atmospheric and Aerosol model	US62 and Continental
AOD at 550 nm	0.1, 0.2, 0.6, 1.0
Ozone (cm-atm)	0.24, 0.26, 0.28, 0.30
Water vapor (g/cm²)	3.0, 3.5, 4.0, 4.5
Sensor-, Target-level	TOA, Sea level

4.4. Results

4.4.1. Comparisons of MAIAC AOD and TPW at two AERONET sites

Figures 4.3 and **Figure 4.4** present the comparison of AOD and TPW measurement, respectively, from MAIAC versus sun-photometer measurements from (i) Manaus-Embrapa and (ii) Rio Branco sites (**Figure 4.1**). These two sites are monitoring distinct aerosol and water vapor context. Manaus-Embrapa site is near of the populated capital of Amazonas and dense and preserved forest as well, while Rio Branco site records seasonal biomass burning events from agricultural areas. The results in Fig. 4.3 and 4.4 are based on match-ups of satellite retrievals and ground-measurements between 2011 and 2015.

The AOD amplitude varies between climate seasons in the Rio Branco and AOD records achieve the 0.6 – 1.2 values during dry season (July to September) due to wildfire and human-induced fires in the region. Although the urban emissions and local fires events in the Manaus region influences the aerosol burden, AOD magnitudes are typically up to 0.4 values. Our results show that MAIAC AOD retrievals agree well with ground-measurements in both AERONET sites. The linear slope is close to unity and Root-Mean-Square-Error (RMSE) is of ~0.065, which suggested low bias at either clean or turbid atmosphere condition. The agreement in time series records illustrates

the feasibility of MAIAC retrievals to trend the seasonal variability of AOD values, with correlation coefficient (R) of 0.884 and 0.971, respectively, in Manaus and Rio Branco sites.

Figure 4.3. Temporal analysis of MAIAC AOD at 0.55 µm compared to AERONET measurements from Manaus (top panel) and Rio Branco (bottom panel) between 2011 and 2015. In the statistics text, n is the number of match-ups, S_o is the linear slope, correlation coefficient (R), root-mean-square-error (RMSE) between MAIAC and AERONET measurements.

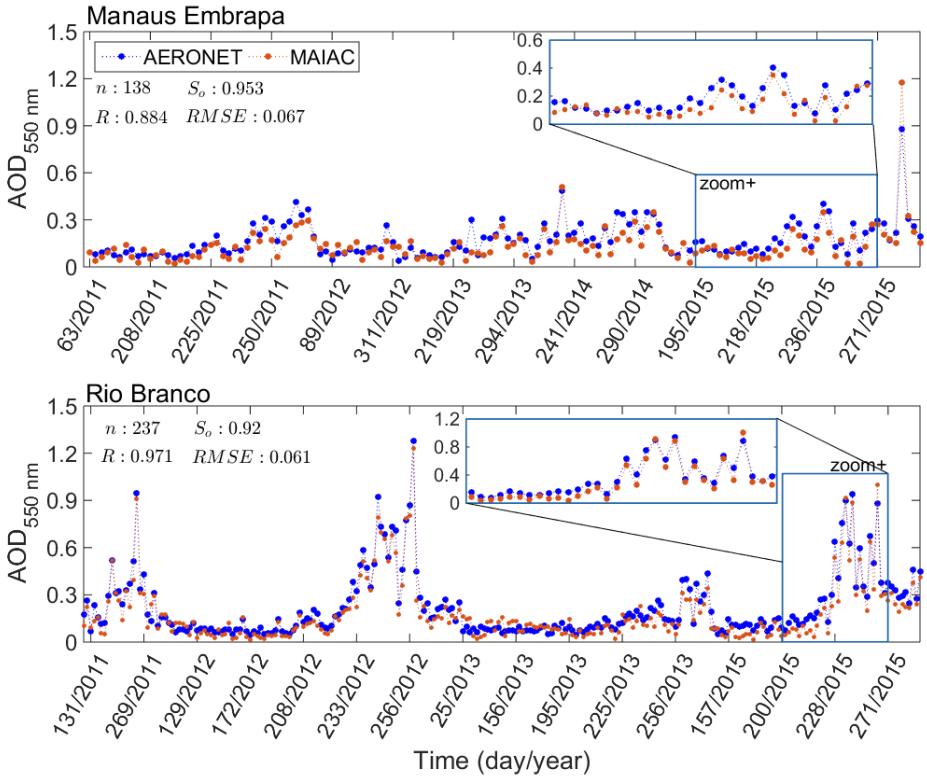

MAIAC and AERONET TPW comparisons are shown in the **Figure 4.4**. In general, TPW in Manaus site range from 3.0 to 4.5 g.cm^{-2} and Rio Branco site, however, shows the same range in first half of the year but lower during dry season (1.5 to 3.0 g.cm^{-2}). In Rio Branco site, TPW retrievals have a higher agreement with AERONET measurements (R: 0.917) than that of Manaus site (R: 0.813). The quality of MAIAC TPW retrievals is quite similar between these sites, with RMSE value of 0.488 (Manaus) and 0.451 (Rio Branco). Our results suggested that MAIAC TPW retrievals

are slightly overestimated, e.g. when MAIAC retrieval is of 3.94 g.cm^{-2}, AERONET is of 4.51 g.cm^{-2} in September 24, 2013. Although MAIAC retrievals present a slight positive bias, the temporal records clearly show a potential of data in reproducing the seasonality in water vapor.

Figure 4.4. Temporal analysis of MAIAC TPW (g.cm-2) compared to AERONET measurements from Manaus (top panel) and Rio Branco (bottom panel) between 2011 and 2015. In the statistics text, n is the number of match-ups, S_o is the linear slope, correlation coefficient (R), root-mean-square-error (RMSE) between MAIAC and AERONET measurements.

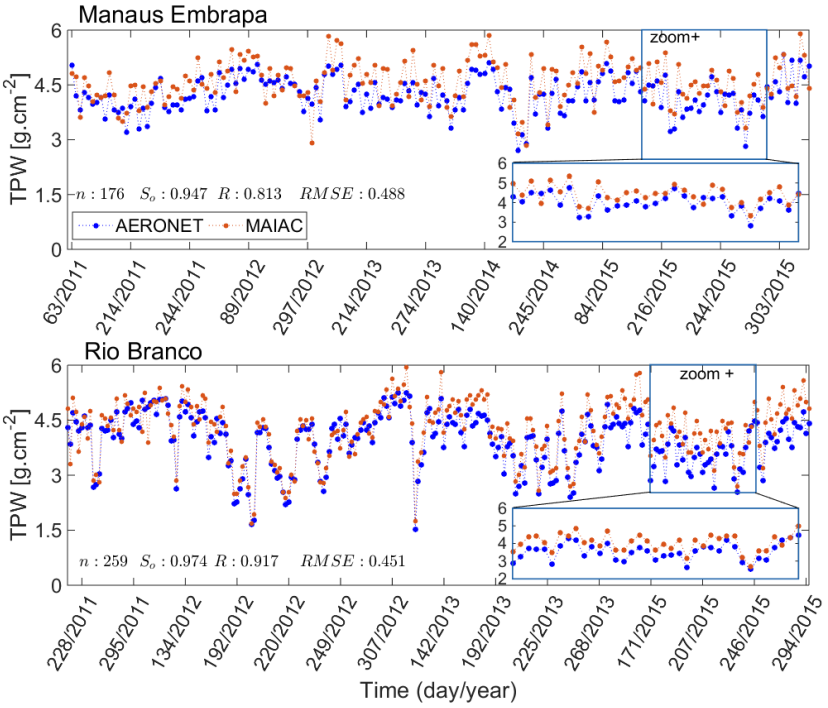

4.4.2. An overview of atmospheric constituents

This session will focus on the general overview of cloud cover fraction and three atmospheric constituents in the Amazon: aerosol loading, total precipitable water (or columnar water vapor) and columnar ozone content. Our results in the **Figure 4.5** show that constituents vary both in latitudinal and longitudinal gradients between quarters of the year. In general, cloud cover fraction and aerosol loading are the most variable components with high spatiotemporal gradients in the austral winter and spring season.

In terms of spatial coverage, a sharp transition pattern of variables is readily observed around 5°S latitude and 70°W longitude related to landscape features and regional climatology: intense land-use change in arc-of-deforestation (DAVIDSON et al., 2012), fire emissions (ARAGÃO et al., 2014) and intense rainfall in the SACZ during summertime (CARVALHO et al., 2004). Cloud cover fraction is a major obstacle for optical remote sensing across the Amazon region due to high coverage throughout the year. The distribution ranges between 70% and 90% near-equator over the northwestern Amazon, except in the Andes Mountains. While the quasi-permanent high cloud cover occurs in the northern Amazon, our results show strong seasonality over southeastern Amazon, spanning 5°S to 20°S in latitude and 65°W to 53°W in longitude, mostly likely of variation in SACZ extension between austral summer (DJF) and winter (JJA) seasons.

The regional background of biomass burning emission changes the atmosphere burden during spring season (SON), and our results demonstrate notably variability in AOD records, whereas relative high values are observed over the southwestern Amazon (**Figure 4.5**). While this biomass burning season have significant influence on seasonal trend of atmospheric burden, relative low AOD are typically observed in the northern Amazon (3S° to 10°N latitudes) with values ranging between 0.01 and 0.2 throughout the year. In addition to particles suspension, fire emissions contribute to large amount of precursor's gases of ozone formation in the troposphere. The maximum ozone content co-occurs coincident with relative high AOD events in the second half of the year, which varies from ~240 DU to ~260 DU between austral autumn and spring seasons in the most part of Amazon. In contrast, though the difference of ozone content is relative high between seasons, the latitudinal gradient was quite low throughout the year. Note that original MOD08 is gridded in the course-resolution (1° x 1° cell).

The annual TPW concentration is almost constant throughout the year (few exceptions in the Andes region and southernmost region), ranging from 3.0 to 4.5 $g.cm^{-2}$ between quarters in the year. However, landscape features, e.g. high elevation areas and savanna biome, and atmospheric circulation influence on spatial distribution of water vapor content. The results point out that TPW increases substantially from ~0.5 $g.cm^{-2}$ around

Andes region (80° to 77°W longitude) to ~4.0 g.cm^{-2} in the central and eastern part of the basin (75° to 50°W longitude). Although some regions have relative low concentration (1.0 – 2.0 g.cm^{-2}), moisture recycling into atmosphere keeps water vapor typically high in most of the Amazon. For example, central Amazon, spanning from 0° to 5°S latitude, presents the highest TPW concentration (~ 4.0 g.cm-2) influenced by moisture inflow from Atlantic Ocean and local evapotranspiration (EMCK, 2007).

Figure 4.5. Seasonal distribution of key atmospheric constituent in the Amazon basin: fraction of cloud cover (FCLOUD in percentage); aerosol optical depth at 550 nm (AOD550 nm unitless); total precipitable water (TPW in g.cm-2); total columnar ozone (TOZ in Dobson Units). The line profiles represent the latitudinal and longitudinal averaged data in the quarter year (December-January-February (DJF); March-April-May (MAM); June-July-August (JJA); and September-October-November (SON). For example, the AOD average from SON season is presented in the Top-Left panel. The land cover context from MODIS Global Land Cover product is addressed here in the Bottom-Left panel. Background of Global Land Cover product (Broxton et al., 2014) reclassified to five land cover types.

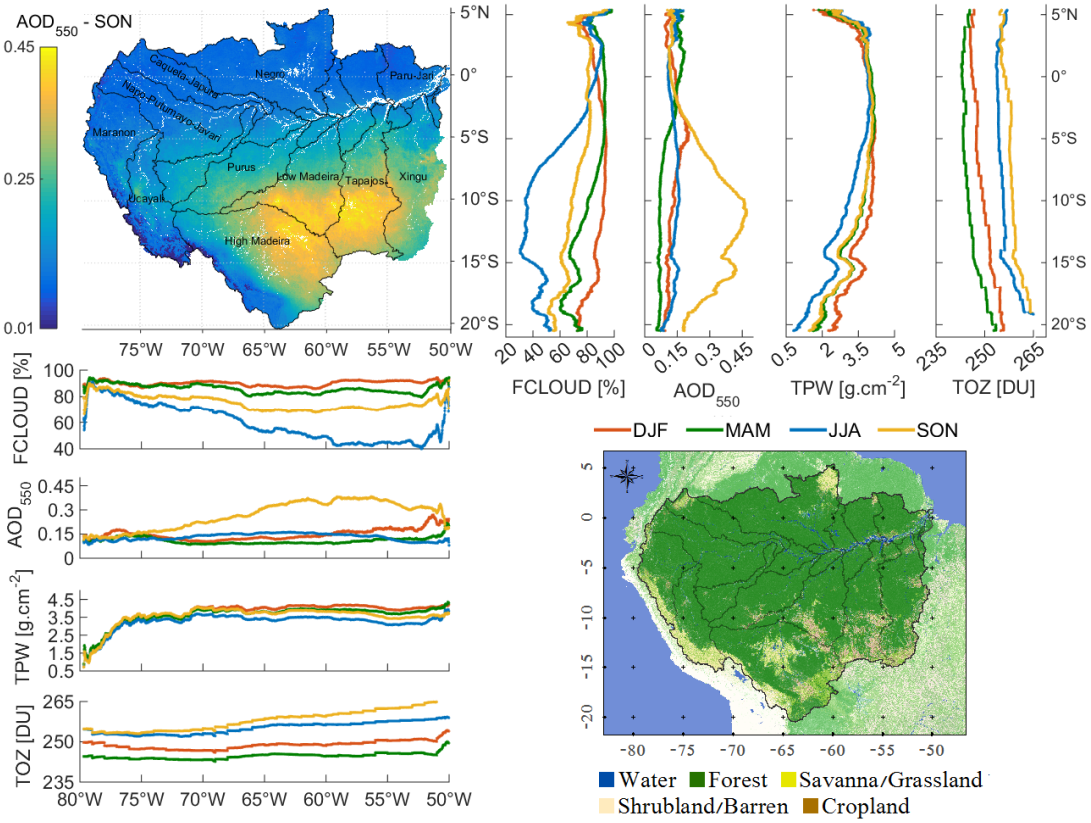

4.4.3. Regional Analysis

To investigate the atmosphere dynamic at regional scale, we performed a monthly analysis of four Amazon regions (**Figure 4.6a**, see rectangles). As observed in the **Figure 4.5**, tropical atmosphere is fairly heterogeneous and annual precipitation supports the definition of these regions based on climate regimes. **Figure 4.6** presents (a) the annual precipitation from $TRMM_{2000\text{-}2015}$ data, (b) monthly precipitation and (c) monthly atmospheric constituents in the four regions (AMZ) from MODIS products within Mar/2000 to Dec/2015 period. Note that y-axis in **Figure 4.6c** represents the number of pixels in particular concentration range. Therefore, rectangular box also expresses the spatial variability within the region, e.g. vertical direction of AMZ3 region shows different concentrations due to latitudinal gradient, see northeastern region in **Figure 4.6c$_i$**.

Results in the **Figure 4.6a** demonstrate the spatial distribution of annual precipitation and its seasonal variability using normalized coefficient of variation (annual CV_{norm}). Annual mean precipitation is typically around 1600 – 3000 mm for most part of the Amazon, with high cumulative rainfall of ~ 3375 mm in the Northwestern (AMZ1), and it changes gradually towards the Southeastern Amazon (AMZ4) with cumulative rainfall of ~1740 mm. In the AMZ1 region, the annual precipitation is well-distributed throughout the year (low CV_{norm}: 0.1-0.2) and rainy season takes place during March through June (**Figure 4.6b**). High rainfall rate in the eastern region is mostly associated to low-level easterly flow (trade winds) transporting large amount of water vapor from Atlantic Ocean and continent, which concentrates on eastern flanks of the Andes Mountains (EMCK, 2007; VILLAR et al., 2009). While AMZ1 region does not present an apparent dry season, other AMZ regions show strong seasonality: central Amazon presents a CV_{norm} of 0.4 – 0.6, which increases to 0.6 – 0.8 values towards southwestern and southern direction. In addition, precipitation regime of AMZ2 region shows that the percentage of annual rainfall is around 35.2 % in the austral summer (DJF) and 11.4 % in the winter season (JJA). The SACZ extends in the southern Amazon inducing the rainy season during summertime (~ 790 mm, 45.4 % of total rainfall in the region). In

the AMZ3 region, austral autumn (MAM) presents 40 % of annual rainfall (wet) compared to 9.4 % in the JAS season (dry).

In particular, precipitation regime is a proxy for the seasonal variability of cloudiness. For example, results shows that the rainy season in the AMZ2 region (6-month) is coincident with high fraction of cloud cover (See in **Figure 4.6b** and **Figure 4.6c$_{ii}$**). In the northwestern, cloud cover of ~ 60 – 100 % is also directly related to intense precipitation rates that restrict routine surface observation by satellite images. In turn, cloud cover fraction changes rapidly in other three regions during austral spring (SON). Among these regions, southern region (AMZ4) presents the relative low cloud cover between June and September (average of 17 to 38%), although it increases to ~ 91 % in the onset of wet season (DJF). In addition, northeastern region (AMZ3) shows the highest cloud cover during March through May, when ITCZ is in its southernmost position (FU et al., 2001; GRODSKY; CARTON, 2003). Therefore, climate regimes modulate the intensity, extension and timing of cloudiness in Amazon. **Figure 4.7** presents quarterly bias ($\Delta\delta_{qrt}$) from JJA/2000 to SON/2015 with drought and flood years (vertical shadows). Table 3 shows the quarterly averaged data for each constituent. In this time-scale, it is observed a reduction of cloud cover fraction during drought year ($\Delta\delta$ is up to -10 %) and opposite condition during flood years (up to - 8.5 %). In absence of exceptional climate oscillation, cloud cover biases range typically between -5 and 5%.

Our findings presented in **Figure 4.6c$_{i}$** indicate that changes of cloud coverage between July and September represent an outstanding period for Amazon remote sensing. However, caution is needed with monthly variability of key atmospheric constituents, especially, because the highest concentrations is readily observed during dry season (**Figure 4.6c**). **Figure 4.6c$_{ii}$** shows that aerosol burden increases from 0.01 - 0.2 values to 0.2 - 0.6 between seasons over AMZ2, AMZ3 and AMZ4 regions. Spatial pattern of fires varies in response to human-caused activities following regional climatology (ARAGÃO et al., 2008). Southern Amazon (AMZ4) undergoes wildfire and human-induced fires during SON season, and AOD peaks reach 0.6 – 1.0 in September (**Figure 4.6c$_{ii}$**). In other way, in the northeastern region (AMZ3), fire practices are common later

in the dry season, caused by the delay in the onset of wet season (DJF). Thus, relative high AOD events are observed at the end of year. In addition, drought years are clearly tipping points for aerosol burden, especially, 2005 and 2007, when $\Delta\delta_{SON}$ was higher than 0.25. In the last decades, Amazon ecosystem undergoes extreme weather episodes and direct human pressures in land-use change. Infrastructure progress and road network make viable the agriculture expansion, and consequently, more landscapes susceptible to fire (NOBRE et al., 2016).

Figure 4.6c shows a similar seasonal pattern of aerosol loading and ozone content over most regions, with changes in ozone content occurring from July through August, and minimum values from February to May. Our findings presented in **Figure 4.6c$_{iv}$** show seasonal distribution of ozone content between the first and second half of the year. The environmental factors, such as net radiation and trace gases (CO, NOx and VOCs), control variability between wet and dry season (ROYAL SOCIETY, 2008), although ozone gradient presents distinct amplitudes among these regions: southern (AMZ4) and northeastern (AMZ3) showed higher ozone seasonality compared to the other two regions (AMZ1 and AMZ2). In the late dry season, the ozone content decreases from ~ 265 DU to lower values (~ 245 DU) in the wet season. The maximum gradient is of 35 DU from austral autumn to spring season in the northeastern Amazon. The results in the Figure 7 show that maximum $\Delta\delta$ O_3 occurs typically in JJA season and highest records were observed during 2015 drought over the AMZ2 and AMZ3 regions followed by significant $\Delta\delta$ decline of cloud cover.

Tropical rainforest contributes to large amount of water vapor in the Amazon atmosphere (MARENGO, 2006). Our results show that northwestern (AMZ1) and central (AMZ2) regions have regular TPW concentration around ~ 4 g.cm^{-2}, in contrast, northeastern (AMZ3) and southern (AMZ4) present a drastic decrease of TPW with the onset of dry season (JJA) (from ~ 4 g.cm-2 to ~ 3 g.cm-2). However, the influence of net radiation increased during dry season changing the vegetation–atmosphere interaction and moisture maintenance in the later of dry season (COSTA et al., 2010; HARPER et al., 2014). In addition to annual season, **Figure 4.7b** shows a significant increase trend of $\Delta\delta$ TPW over all regions during the period 2000-2015. However,

Martins et al. (2017) shows that this water vapor is result of upward bias trend in Terra TPW retrievals. In this time scale, oscillation of Δδ TPW is more pronounced over the southern region. Particularly for 2010 drought, southern AMZ4 presented a $\Delta\delta_{JJA}$ TPW of -0.4 g.cm^{-2}, while other regions show quite similar $\Delta\delta_{JJA}$ between 0 to 0.1 g.cm^{-2}.

Figure 4.6. Average precipitation and atmospheric constituents using 15-year data from Tropical Rainfall Measuring Mission (TRMM) and Moderate Resolution Imaging Spectroradiometer (MODIS) Terra products in the four regions. (a) Annual precipitation at 0.25° x 0.25° resolution and normalized coefficient of variation (CVnorm) resampled to 2.5° x 2.5° resolution. (b) Monthly precipitation from average TRMM data within 2000-2015 period; (c) Monthly cloud cover fraction and atmospheric constituents from averaged data MODIS between Mar/2000 and Dec/2015. The y-axis of panels (c) shows the number of pixel for each concentration range: (ci) fraction of cloud cover, (cii) aerosol optical depth at 550 nm, (ciii) total precipitable water, (civ) total columnar ozone.

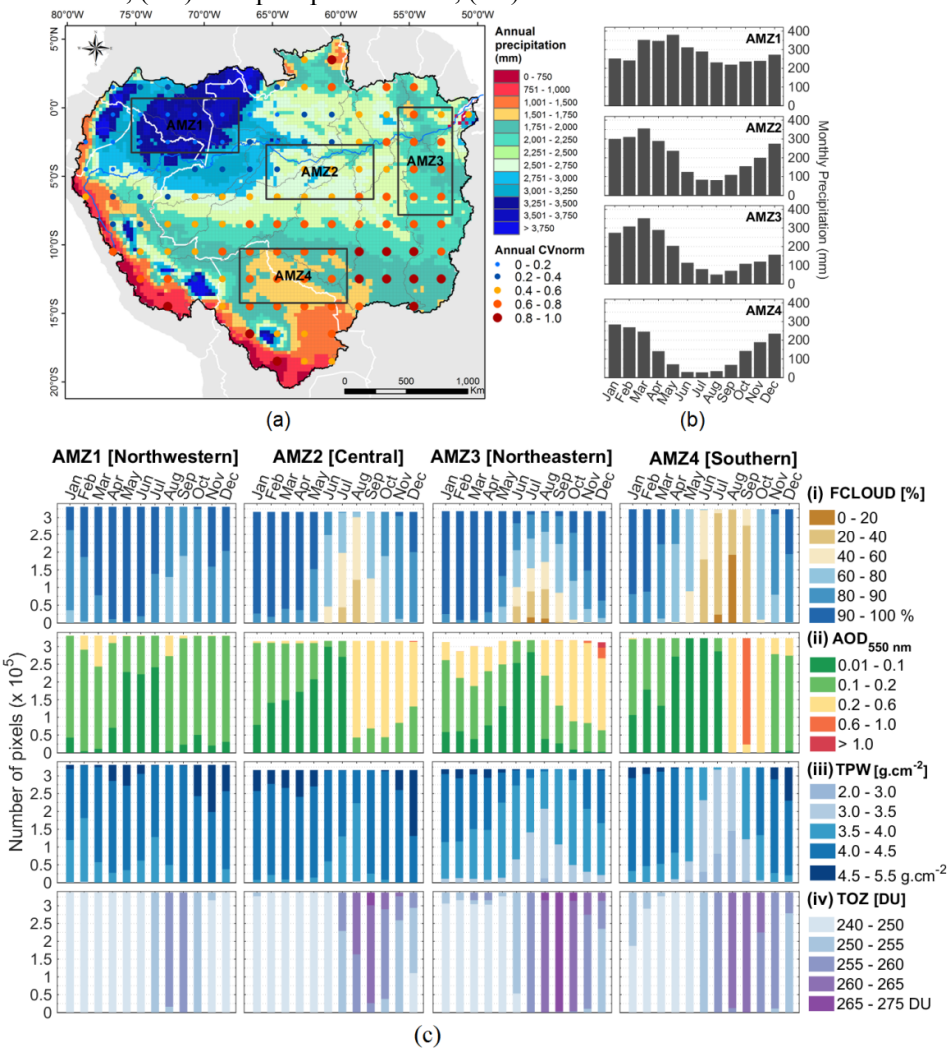

Figure 4.7. Time-series of quarterly bias (Δδ) for atmospheric constituents from Moderate Resolution Imaging Spectroradiometer (MODIS) Terra products in the four regions. (a) Fraction of cloud cover. (b) Aerosol optical depth at 550 nm. (c) Total precipitable water. (d) Total columnar ozone. The shaded vertical bar denotes the 2005, 2007, 2010, 2015 drought years (brown) and the 2009, 2012, 2014 flood years (blue) presented in Marengo and Espinoza (2016).

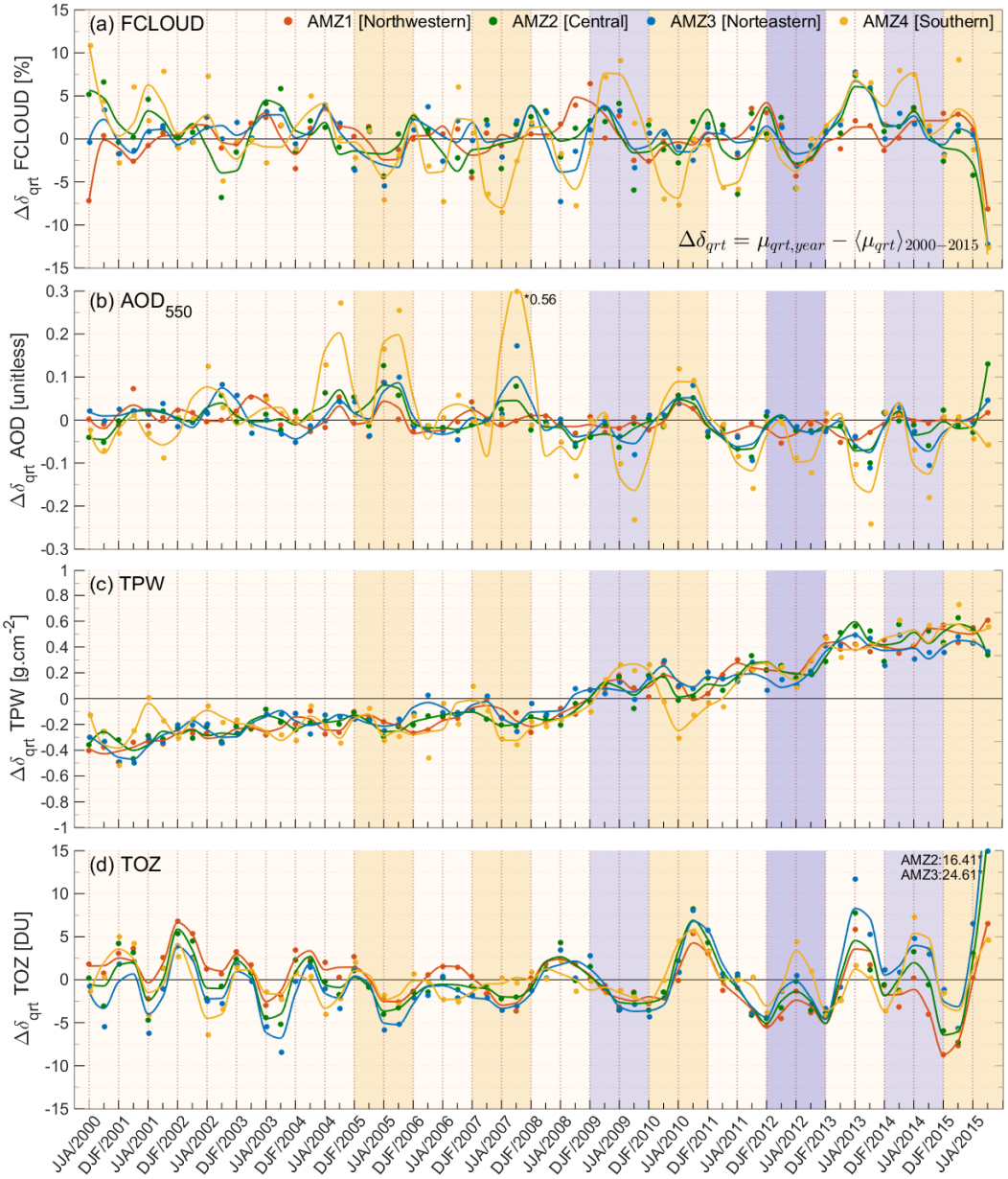

Table 4.2. Quarterly averaged and standard deviation data of cloud cover fraction and key atmospheric constituents in the four Amazon regions.

	AMZ1	AMZ2	AMZ3	AMZ4		AMZ1	AMZ2	AMZ3	AMZ4
	FCLOUD (%)					TPW ($g.cm^{-2}$)			
DJF	88.36±3.2	92.33±1.9	95.04±3.5	91.35±2.6	DJF	4.17±0.19	4.37±0.13	4.05±0.22	4.26±0.2
MAM	92.86±1.1	91.23±2.1	93.04±3.8	75.72±4.9	MAM	4.28±0.16	4.42±0.13	4.13±0.25	4.03±0.21
JJA	88.14±3.0	57.22±10.3	60.74±21.5	29.25±6.6	JJA	4.13±0.13	4.02±0.15	3.59±0.27	3.18±0.24
SON	85.11±2.0	75.56±3.4	80.30±9.4	62.06±3.1	SON	4.37±0.1	4.27±0.10	3.7±0.2	3.96±0.19
	AOD (unitless)					TOZ (DU)			
DJF	0.13±0.02	0.14±0.03	0.17±0.05	0.12±0.03	DJF	245.44±0.6	247.1±1.3	248.8±1.8	250.85±1.2
MAM	0.14±0.04	0.1±0.02	0.14±0.06	0.08±0.02	MAM	242.68±0.3	244.1±1.1	246.2±2.4	246.56±0.9
JJA	0.12±0.02	0.14±0.02	0.10±0.03	0.17±0.02	JJA	251.61±0.3	254.3±0.9	257.3±0.5	256.48±0.7
SON	0.13±0.02	0.25±0.04	0.27±0.11	0.42±0.05	SON	252.06±0.8	258.0±2.1	262.7±1.9	259.45±0.9

4.4.4. Sub-basin analysis

Additionally, evaluation of atmospheric constituents in six Amazon sub-basins explores monthly time series and its seasonality using multi-angle MODIS and MOD08 data (**Figure 4.8** and **Figure 4.9**). These six sub-basins were selected based on environmental context: Napo-Putumayo-Javari, Negro and Paru-Jari contain well-preserved and pristine forest areas; while High-Madeira, low-Madeira and Tapajos basins are under intense land-use changes and present fragmented forest (DAVIDSON et al., 2012). Monthly data were used in BFAST algorithm to compute seasonal pattern and inter-compare those values among sub-basins. Note that seasonality was normalized between 0 and 1, with location of sub-basin (colored line) represented by arrow orientation (north or south) using the Amazon River as reference.

In general, main atmospheric feature of northern basins is the low seasonality of almost all constituents, exception for ozone content, while the southern basins have significant gradient of atmospheric constituents between wet and dry season. Cloudiness regime persists mostly during 9-month (October to June) with high cloud cover fraction over all northern basins and without specific clear-sky period for optical remote sensing. In turn, southern basins present low cloud cover (up to 40%) during 4-month (June to September), which enhance the chances of surface observation. Similar to our previous results, monthly time series of AOD values show strong seasonality in the southern sub-basins and almost stable aerosol condition in the northern basins. In particular, Paru-Jari

in the northeastern Amazon presents AOD increase mostly in the first half of the year due to cross-Atlantic transport of Sahara dust desert and biomass burning emissions from Africa (JONQUILRES et al., 1998; KAUFMAN et al., 2005).

Monthly average of ozone content shows relative low concentrations in the first half of year, with values around 240-255 DU, and increases in ~20 – 30 DU in the second half of the year. In the dry season, net radiation and trace gases emissions might contribute to increase the tropospheric ozone content, mainly, over the southern Amazon (ZIEMKE et al., 2009). Actually, note that aerosol burden and ozone content present the same peak and length regime in the southern basins, but distinct patterns for the northern basins. Tropical forests are the dominant global source of atmospheric BVOCs (JARDINE; JARDINE, 2016), and this results in the northern Amazon suggested that natural VOCs and NOx emissions (+ net radiation) might control the O_3 production in region (KARL et al., 2007).

Influenced by equatorial trades and most covered by pristine forest, Napo-Javari, Negro and Paru-Jari show relative high TPW concentrations in both space and time (4.0 to 5.5 $g.cm^{-2}$). Particularly, High-Madeira presents low TPW concentrations (2.5 to 3.5 $g.cm^{-2}$) in JJA season compared to other sub-basins, which might be induced by regional moist circulation and intense land-use conversion in the recent decades. The beginning and length features of seasonal TPW patterns are clearly distinct between sub-basins; there is a significant gradient between austral summer and winter seasons. For example, Paru-Jari sub-basin (North) has minimum in August and September, in contrast, southern sub-basins presented minimum TPW values during June and July.

Figure 4.8. Time series of monthly cloud cover fraction and atmospheric constituents derived from Moderate Resolution Imaging Spectroradiometer (MODIS) Terra products in the six Amazon sub-basins. Centroid coordinates of sub-basins are presented in front of horizontal bar for each variable.

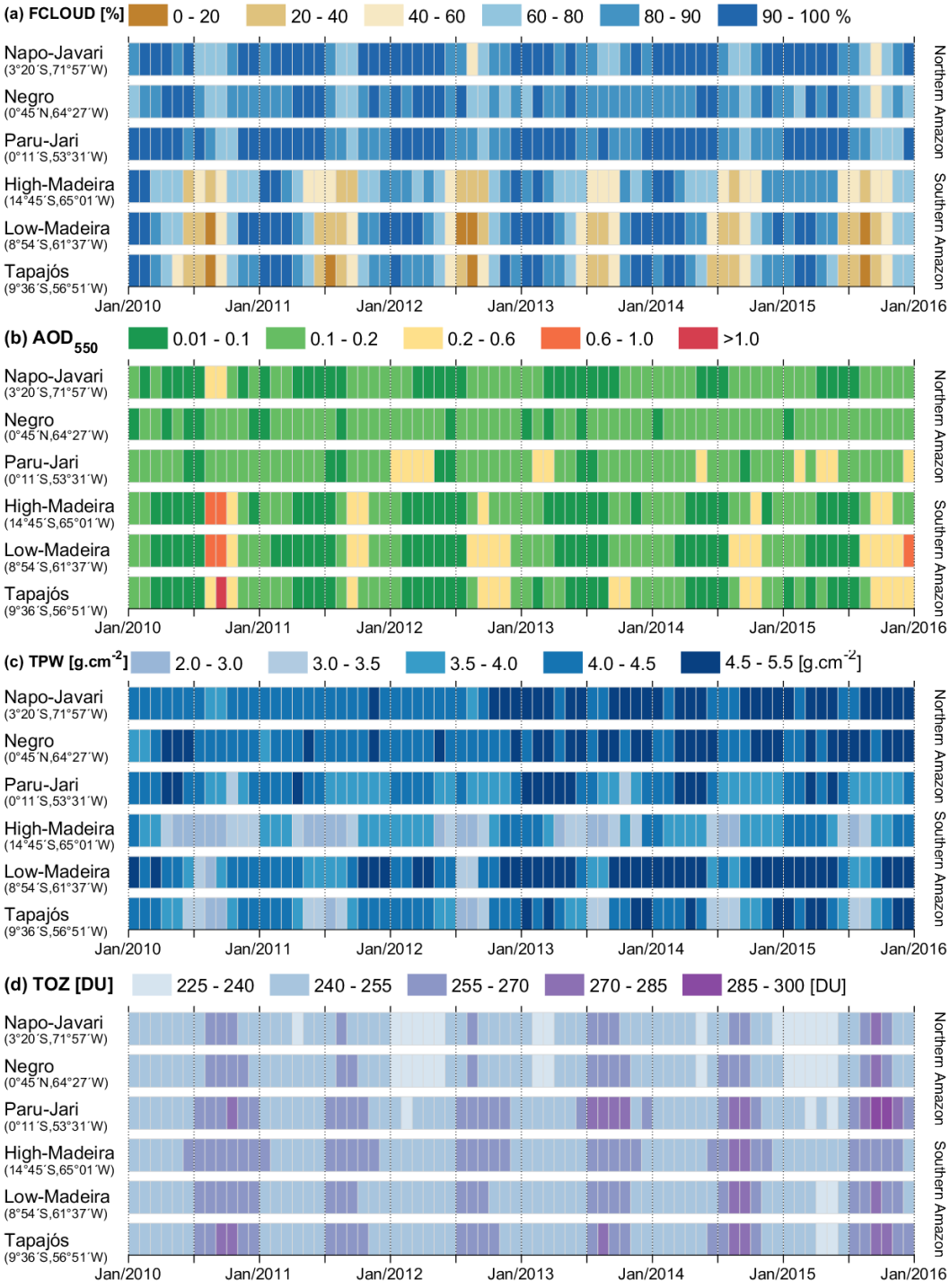

Figure 4.9. Seasonal pattern of atmospheric constituents in the six Amazon sub-basins: Napo-Putumayo-Javari, Negro and Paru-Jari basins (northern); and High-Madeira, low-Madeira and Tapajos basins (southern). Seasonality was normalized between 0 to 1 and arrow orientation indicates sub-basin location with northern (up arrow) and southern (down arrow).

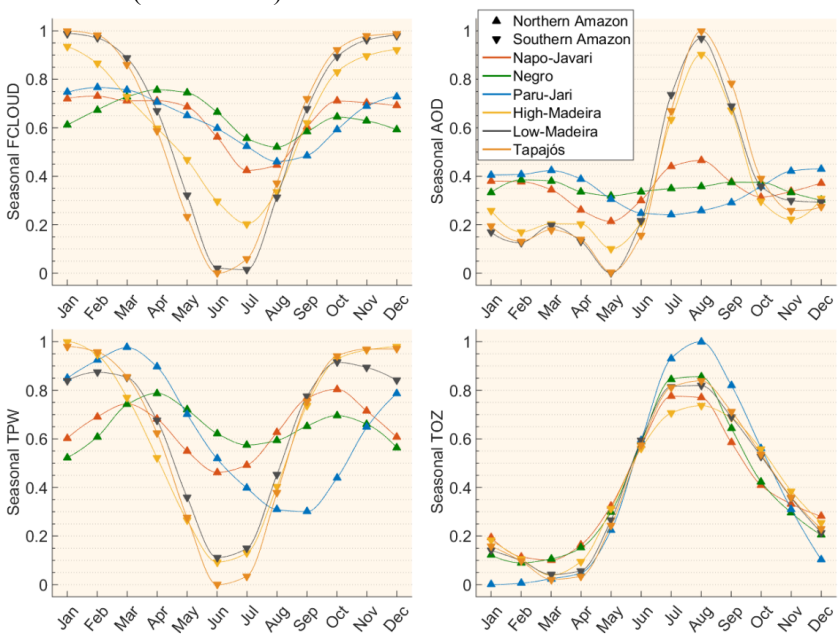

4.4.5. Implication of key atmospheric constituents on optical remote sensing

The radiative transfer simulation presented in **Figure 4.10**, **4.11** and **4.12** includes the calculation of atmospheric scattering and gaseous transmission for various satellite sensors, e.g. Multispectral Instrument (MSI) onboard of Sentinel-2 and Multispectral Camera (MUX) onboard of China-Brazil Earth Resources Satellite (CBERS). The simulation was based on common AOD (0.1, 0.2, 0.6 and 1.0), water vapor (3.0, 3.5, 4.0 and 4.5 $g.cm^{-2}$) and ozone (240, 260, 280 and 300 DU) values across the Amazon.

In **Figure 4.10**, scattering magnitude shows an exponential decrease with increasing wavelength, and consequently, affects shorter wavelengths more than longer. Although satellite sensors presented distinct response function and center band position, scattering effects are quite similar for spectral band in the same wavelength. In general, atmospheric bias is most severe in blue and green bands, for example, scattering reflectance in MSI blue band (495 nm) reaches 2.75 times higher than that observed in

the infrared band (840 nm) for AOD of 1.0. Our results also illustrated that aerosol and Rayleigh scattering could increase TOA reflectance in ~ 0.06 during severe AOD episodes (from 0.1 to 1.0) in MODIS 0.420 µm, as example for AOD events observed in southern Amazon. In contrast, northern basins present relatively low AOD values (0.1 to 0.2) and the sensitivity analysis using these AOD values (0.1 and 0.2) shows a slight similar scattering for all satellite sensors. This result suggests that in regions under relative low AOD regimes, the uncertainties in AOD parameter has less impact in atmospheric correction when compared to region with drastic change in atmosphere condition. Therefore, to minimize the uncertainties on surface reflectance retrievals, it is desirable to use satellite images acquired under clear atmosphere (no clouds or low aerosol loading). In this context, we illustrated in the **Figure 4.13** that under quite similar cloud cover fraction, it is possible to choose clear-sky image with relative low AOD values during July (AOD: 0.1-0.2), instead of satellite data in August due to relative high AOD values (0.2- 0.6) in most part of Amazon basin.

Figure 4.10. Rayleight and aerosol scattering reflectance (ρ) computed by different aerosol optical depth (AOD) for various satellite sensors: Wide Field Imager (WFI), CBERS-4; Operational Land Imager (OLI), Landsat-8; Moderate Resolution Imaging Spectroradiometer (MODIS), Terra; Multispectral camera (MUX), CBERS-4; MultiSpectral Instrument (MSI), Sentinel-2.

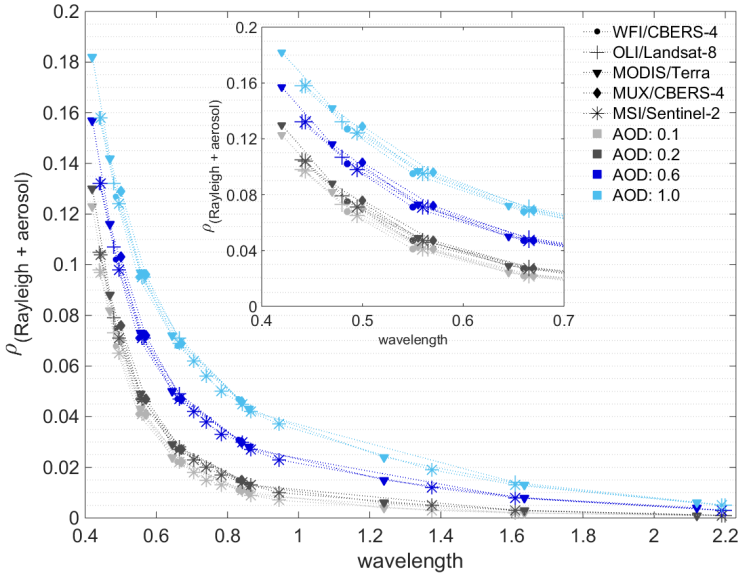

The findings presented in **Figure 4.11** and **4.12** show a strong spectral dependence of water vapor and ozone absorption, generally, with relative high (low) transmittance of water vapor (ozone) in the visible region and low (high) in the infrared region. Our results show that water vapor have strong absorption feature affecting spectral bands at 0.660, 0.710, 0.840 and 2.100 μm (**Figure 4.11**). The lower T_{H2O} was observed for MODIS band at 2.1 μm, where the T_{H2O} reaches 0.89 for 4.5 $g.cm^{-2}$. In addition, new MSI sensor onboard of Sentinel-2 includes useful red-edge bands that are also affected by water vapor absorption (T_{H2O} of 0.92 – 0.95). Note that some channels present a low or none water vapor effects, e.g. mostly in visible bands, and other bands show T_{H2O} changes drastically from 1.0 (none) to 0.890. Indeed, although T_{H2O} magnitude ranges from 0.89 to 1.0 according to spectral band, this sensitivity analysis shows that variation of concentration ranges causes small changes in T_{H2O} (up to 0.02). Furthermore, these results suggested that empirical atmospheric correction methods, such as dark-object subtraction (CHAVEZ, 1988), are inappropriate under abundant amount of water vapor conditions, due to strong influence of gaseous absorption in the red and infrared bands.

Figure 4.12 shows that ozone transmittance (T_{O3}) decreases rapidly in the green (~550 μm) and red (670 μm) bands, while infrared bands does not undergo ozone absorption (T_{O3} = 1.0). Vegetation indices commonly based on spectral contrast of red and NIR bands, such as Normalized Difference Vegetation Index (NDVI) or Enhanced Vegetation Index (EVI), might suffer an increase in their values when ozone effects are not included in the atmospheric correction. However, although ozone absorption affects transmittance in some spectral bands, the common range in Amazon basin (240-300 DU) produces only slight variation in T_{O3} (~0.95 - 0.97), what might reduce impacts of seasonal variation in this input parameter for atmospheric correction. Unlike channels designed to atmospheric retrieval, satellite sensors for land monitoring have spectral bands located in so-called atmospheric-windows in order to reduce the influence of most gaseous absorbers, such as CO_2, CH_4, O_2 and NO_2 (GAO et al., 2009).

Figure 4.11. Total water vapor transmittance (TH2O) simulated for various satellite sensors: (a) Wide Field Imager (WFI), CBERS-4; (b) Operational Land Imager (OLI), Landsat-8; (c) Moderate Resolution Imaging Spectroradiometer (MODIS), Terra; (d) Multispectral camera (MUX), CBERS-4; (e) MultiSpectral Instrument (MSI), Sentinel-2.

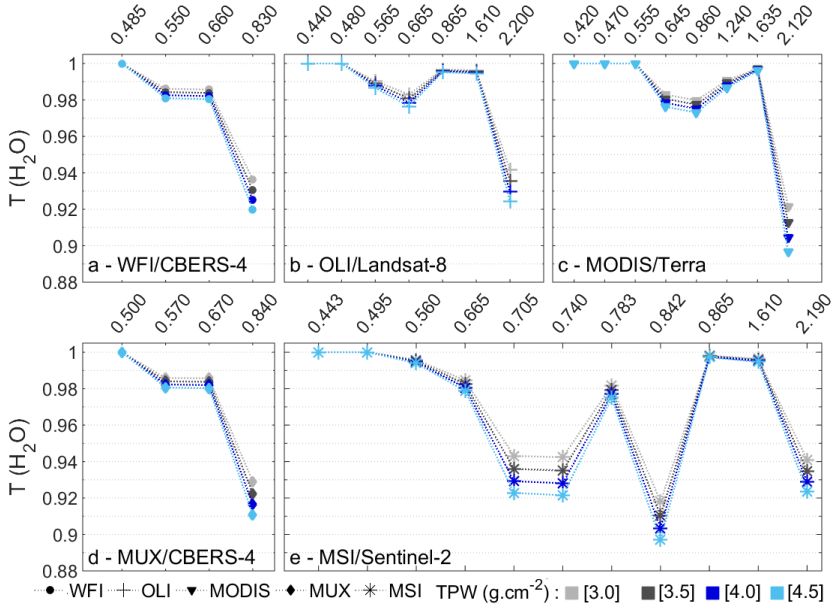

Figure 4.12. Total ozone transmittance (TO3) simulated for various satellite sensors: (a) Wide Field Imager (WFI), CBERS-4; (b) Operational Land Imager (OLI), Landsat-8; (c) Moderate Resolution Imaging Spectroradiometer (MODIS), Terra; (d) Multispectral camera (MUX), CBERS-4; (e) MultiSpectral Instrument (MSI), Sentinel-2.

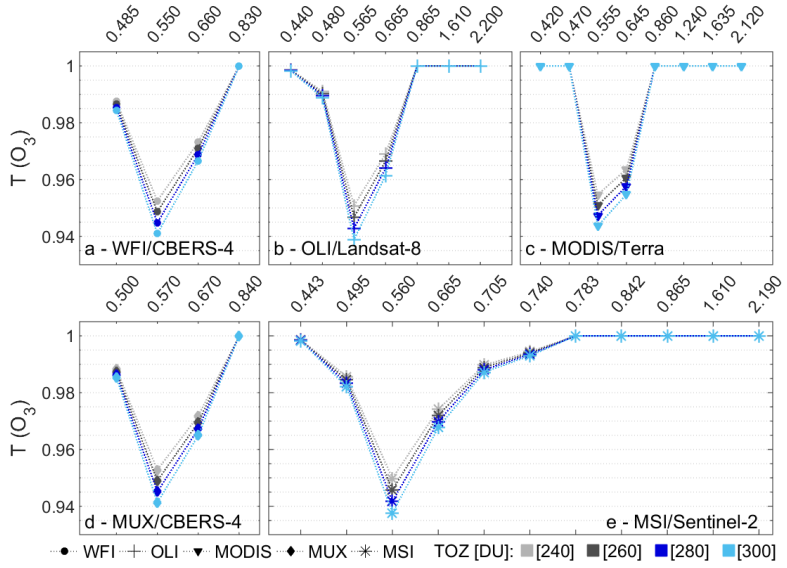

Figure 4.13. Cloud cover fraction (a, b) and aerosol optical depth (c, d) for July and August. Location of Landsat-8 scene grid is shown with path (vertical) and row (horizontal) information as one more reference for remote sensing users. Note the same cloud cover fraction but the distinct AOD condition between July and August.

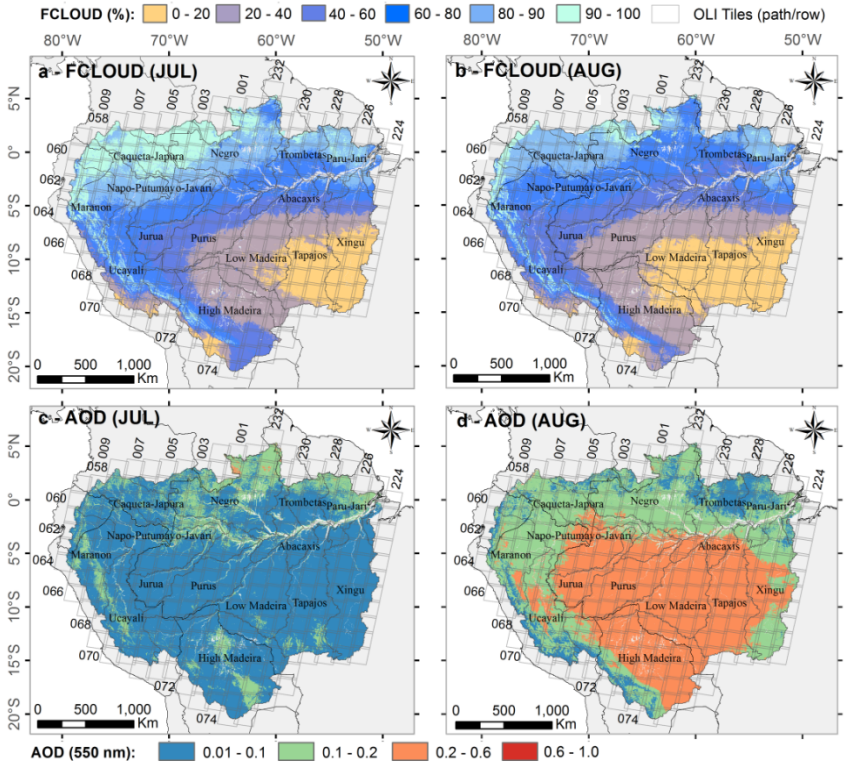

4.5. Discussion

Our work provides useful information about the seasonal patterns of atmosphere constituents using a historical dataset of new multi-angle MODIS (MAIAC) and standard MOD08 products. Due to the impact of atmospheric effects on satellite observations, this database contributes for a preliminary assessment of cloud cover and key atmospheric constituents, which has serious implication on the remote sensing applications in the Amazon region. The results presented in this work show a substantial contrast of cloud cover fraction across the Amazon (**Fig. 4.6**): northern Amazon present high and quasi-permanent cloud coverage (80-100%) throughout the year, while other regions show 3- to 5-month period with relative low cloud cover (0 – 40%). Previous studies reported similar findings (ASNER, 2001; HILKER et al., 2012). Cloudiness periods are strongly related to precipitation regimes (**Fig. 4.6b** and **4.6c**); high cloud

cover corresponds to the rainy season in all regions, however, months of highest cloudiness vary in both space and time. In the background section, we revised several climate features controlling monsoon system and moisture recycling, such as equatorial trades, easterly moisture flow, extreme weather events caused by ENSO and Atlantic SST oscillation, local evapotranspiration, influence of SACZ in summertime and displacement of the ITCZ position (see references in Section 2). Therefore, cloud cover fraction may be understood as the response of the regional climatology. This unique approach using 15-year dataset support future remote sensing application when presenting cloud cover distribution in both space and time.

In addition to cloud cover, aerosols contribute to drastic change of atmosphere composition, and their seasonality is strongly associated to climatic seasonality, air mass transport and emission sources (ANDREAE et al., 2015). During the wet season (DJF), clean atmospheric conditions (AOD 0.1-0.2) were observed across the Amazon (Figs. **4.5**, **4.6** and **4.8**), which can be explained by wet deposition and aerosol dominance by natural emissions from pristine forest regions (ARTAXO et al., 2013; MARTIN et al., 2010). In turn, biomass burning emissions change drastically the atmospheric composition in the dry season with AOD events exceeding 0.2 (**Fig. 4.8**). The highest AOD events occur during austral spring (SON) in most part of Amazon (**Table 4.2** and **Fig. 4.9**). Similarly, Hoelzemann et al. (2009) evaluated AOD events during biomass burning with peak records ranging 1.0 to 3.0. At intra-annual scale, the most critical AOD episodes were observed in the 2005 and 2007 droughts. Landscape fires have been used to land-use conversion, land clearing for cattle rising and agricultural activities (ARAGÃO et al., 2008; CHEN et al., 2013). Since 2004, annual deforestation rates have been reduced in the Amazon (ARAGÃO et al., 2014; REDDINGTON et al., 2015), but the fire incidences do not present the same trend, especially, during recent droughts years. Aragão and Shimabukuro (2010) reported a fire increase between 1998 and 2007, even as deforestation decreases in the same period. Additionally, Morton et al. (2008) quantified that 84% of fires incidence (2003-2007) was detected in active deforestation frontiers, such as Bolivia and Brazilian states of Mato Grosso, Pará, Rondônia. Therefore, anthropogenic emissions are the major

aerosol source in the dry season, while biogenic aerosols from pristine forest areas dominate during the wet season.

Biomass burning and biogenic emissions contribute to increase the trace gases source of O_3 precursors across the Amazon basin, such as NOx, VOCs and CO (ANDREAE and MERLET, 2001; AKAGI et al., 2011). In the troposphere, peak concentration of ozone occur when precursor emissions coincide with climate factors (net radiation and temperature) and produces feasible conditions for photochemical reactions in O_3 formation (ROYAL SOCIETY, 2008). The results presented in **Fig. 4.8** and **Table 4.2** show that ozone content usually ranges between 225 and 255 DU in the DJF season and increases to ~ 260 - 280 DU during JJA season. This ozone gradient can be a result of high amount of O_3 precursors coupled with a rise in air temperature and incoming net radiation between seasons (AINSWORTH et al., 2012). Rummel et al. (2007) reported that ozone mixing ratio over southwest Amazonia was about four times higher during dry season than that in the wet season. Due to O_3 damage on vegetation and human health impacts (MILLS et al., 2011), future studies are substantially important to quantify the impacts of climate change and intense land-use on ozone production. Pacifico et al. (2015) simulated a reduction of O_3 concentrations by about 15 ppb in absence of biomass burning emission over Amazon basin. In addition to fire emissions, changes of lighting NOx and BVOC emissions, natural ozone precursors, also present significant influence on ozone concentrations (KARL et al., 2007; MURRAY et al., 2013). Thus, biogenic emissions and air mass transport can be in part responsible for seasonal O_3 variation observed in **Fig. 4.9** for northern sub-basins (JACOB; WOFSY, 1988), while trace gases from biomass burning dominates in the southern Amazon. Although the study strong believe in these environmental factors, the small TOZ variation could influence the accuracy of this analysis, since the RMSE is 31.6 DU in previous study (Borbas et al., 2011).

Large-scale atmospheric circulation and local moisture recycling are major mechanisms that influence moisture feedback in the tropical rainforest region (ELTAHIR and BRAS, 1994; ENT et al., 2010). Our results in the **Figs. 4.5** and **4.6** show that high water vapor concentration takes place in the austral summer and autumn across the

Amazon basin. In northern sub-basins, TPW concentration of ~ 4.0 – 5.5 g.cm-2 persists throughout the year, while south sub-basins present seasonal changes from 4.0 – 5.5 $g.cm^{-2}$ to 2.0 – 3.5 $g.cm^{-2}$ between first and second half of the year (**Figure 4.8**). In the end of dry season (October and November), changes in water vapor content as response of forest's evapotranspiration contribute to dry-wet transition (FU and LI, 2004). Malhi et al. (2002) quantified energy and water dynamic near Manaus in central Amazon and reported that annual evapotranspiration (1123 mm) contributes with 54% of the rainfall using measurements from September 1995 to August 1996. Since evapotranspiration plays a significant role in maintaining atmospheric moisture (see references in Marengo et al., 2006), Amazonian deforestation in the past three decades (HANSEN et al., 2013) is expected to cause a reduction in evapotranspiration and so induce changes in moisture budget (SAMPAIO et al., 2007). However, our results show significant upward trend of TPW records over the period 2000-2015 (**Fig. 4.9**). Martins et al. (2017) suggested that this upward trend is typical calibration issue of MODIS 17-19 bands, due to upward trend of bias between 2000 and 2015. Although this result is probably associated with sensor calibration, Bordi et al. (2014) reported a rising trend of water content in the Amazon basin based on longer climate modelled and reanalysis data within 1900-2009. The authors suggested that local temperature changes combined with large-scale mechanisms, such as monsoon variability and moisture transport, might control this observed trend in the last decades. An additional analysis is needed, coupling field measurements (e.g. AERONET) with satellite observations, to clarify the temporal changes in water vapor and how surface-atmosphere system responds to future land-cover changes.

The ability to quantify surface parameters using satellite observations depends on the knowledge of the atmospheric effects (FRASER and KAUFMAN, 1985). Although satellite observations are susceptive of errors in sensor calibration, geometric correction and sun-view geometry (CHANDER et al., 2009; GALVÃO et al., 2012), recent studies in the Amazon pointed out uncertainties associated to cloud screening and atmospheric bias in surface reflectance retrievals (HILKER et al., 2012, 2015). In most part of Amazon, seasonal variation in cloud cover was in the order of 60 - 70 % between the

wet and dry seasons and atmospheric bias varies temporally due to strong absorption caused by high water vapor content and seasonal fire emissions (**Fig. 4.10** and **4.11**). The simulation of scattering reflectance and gaseous transmittance in the **Fig. 4.10** show that Rayleigh and AOD effects could increase TOA reflectance up to 18.5 % and 16.0 % in deep blue and blue bands, respectively. In turn, absorbers constituents have spectral dependence that attenuates solar radiance transmission in order of 0.92 – 0.95 depending on sensor bands (**Fig. 4.11** and **4.12**). Zelazowski et al. (2011) quantified atmospheric bias over high and low altitudes in Peruvian Amazon, and highlighted substantial uncertainty due to season pattern of key atmospheric constituents and elevation-dependent. Although sensitive analysis restricts viewing geometries and aerosol model, simulated concentrations are consistent for Amazon context and allow relative comparisons.

As atmospheric constituents are seasonally dependent, additional information of maximum and minimum month for each constituent are useful information for remote sensing users (**Figure 4.14**). Note that **Fig. 4.14** gives the relative maximum and minimum for each constituent, although magnitude varies drastically across the Amazon basin (**Figure 4.5**). Understanding seasonal pattern of cloud cover and concentration ranges of key atmospheric constituents enhance our capabilities in surface observation.

Figure 4.14. Maximum and minimum months of (a, b) cloud cover and key atmospheric constituents: (c, d) aerosol optical depth, AOD; (e, f) total precipitable water, TPW; and (g, h) total columnar ozone, TOZ. Location of Landsat-8 scene grid is shown as one more reference for remote sensing users; see path (vertical) and row (horizontal) information.

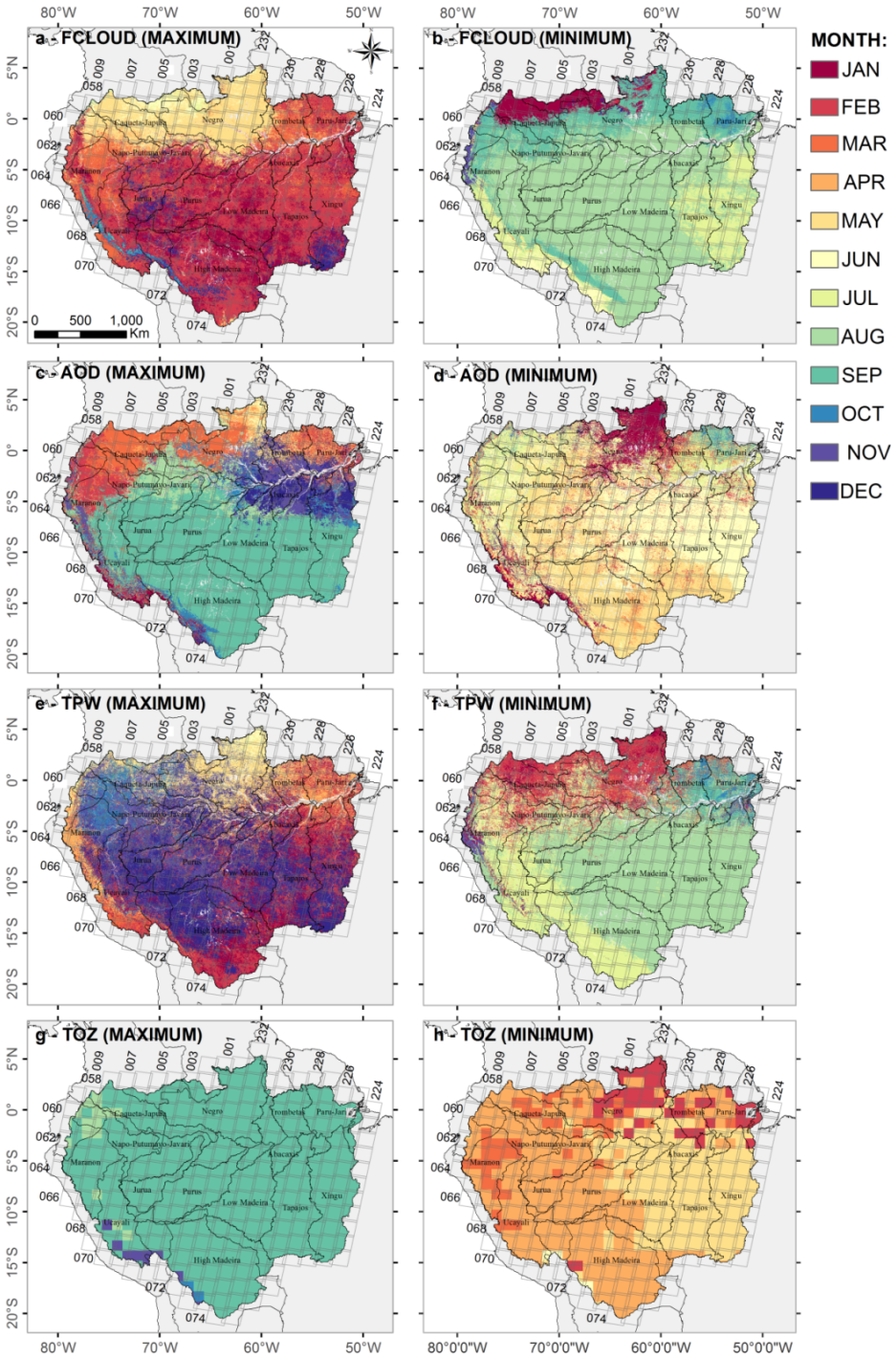

4.6. Summary and conclusion

This study presents an assessment of the cloud cover fraction and key atmospheric constituents in the Amazon basin. Validation of MAIAC AOD and TPW shows the feasibility of new multi-angle MODIS algorithm to retrieve quality data at high 1 km resolution. In the Amazon context, the results presented here give a detailed overview of key atmospheric features at regional and sub-basin scales:

Cloud cover: The findings of our regional analysis show a persistent cloudy condition in the northwestern Amazon, with 80 to 100 % over 10-month period. During the austral winter and spring season, cloud cover decay from 80 – 100% to 10 – 40% in most regions of Amazon and represents the most likely opportunity for optical remote sensing. The length of cloudless period varies according to sub-basins: northern sub-basins are under constant cloud coverage, even in the drought years, while the southern sub-basins show cloudiness regime during dry season (JJA).

Aerosol optical depth: AOD distribution is fairly homogeneous and relative low values (0.1 – 0.2) during first half of the year (0.01- 0.2) due to dominant natural aerosol emissions and weaker human-induced fires. In the dry season, drastic change in AOD events are observed in the northeastern and southern Amazon influenced by biomass burning emissions, with an increase of AOD values to higher than 0.2. The drought effect is evident during 2005 and 2007 year, when $\Delta\delta$ AOD exceeds 0.25 in the SON period.

C*olumnar water vapor*: As moisture-rich air masses are transported through this region, abundant amount of water vapor (3.0 to 5.0 $g.cm^{-2}$) was observed in the Amazon region. Regional analysis presented the highest water vapor of ~ 4.5 $g.cm^{-2}$ in the northwestern Amazon throughout the year, while the other regions show pronounced seasonally with common concentrations varying between 3.0 and 5.5 $g.cm^{-2}$, exception for Andes Mountains and savanna areas. Temporal variability of water vapor content presents a rising trend from 2000 through 2015; long-term increase of water content might be consequence of sensor calibration issue in MODIS 17-19 bands.

Total columnar ozone: Our results show seasonal ozone content between first and second half of the year, with slight latitudinal gradient most likely due to course-resolution of MOD08 ozone product. The relative low O_3 is observed over Amazon basin during first half of the year (~ 245 DU) and increase 5.7 % for second half (260 DU) due to trace gases emission and net radiation for O_3 formation. In times series scale, peak O_3 concentration ($\Delta\delta_{SON}$ TOZ of 24.61) was observed in 2015 drought year followed by negative (positive) $\Delta\delta_{SON}$ of cloud cover (AOD) values.

In conclusion, consistent information of atmospheric dynamic allows remote sensing insights about cloud-free periods and critical month of aerosol burden. The Amazon monitoring by satellite observation faces a several challenges regarding atmosphere dynamic, such as high aerosol loading from biomass burning events; lengthy cloudiness period (7- to 9-month); quasi-constant and high water vapor concentration; and ozone peak coincident with cloudless window in the dry season. Under severe atmospheric conditions, the quality of remote sensing surface retrievals need further consideration due to constituent concentrations induce significant changes on the atmospheric scattering and transmission, although temporal variability of absorbers gases causes slight difference in transmittance. At last, the role of remote sensing in the terrestrial monitoring have been change with open access satellite imagery. Understanding seasonal pattern of cloud cover and key atmospheric constituents enhance our ability in surface retrievals, especially, over tropical humid regions.

5 ASSESSMENT OF ATMOSPHERIC CORRECTION METHODS FOR SENTINEL-2 MSI IMAGES APPLIED TO AMAZON FLOODPLAIN LAKES[2]

5.1. Introduction

Inland waters are an essential resource for terrestrial life and ecosystem services (DUDGEON et al., 2006; VÖRÖSMARTY et al., 2010). The Amazon freshwater is an ecosystem bearing one of the highest biodiversities in the world (ABELL et al., 2008). Amazonian aquatic systems depend on satellite image applications to investigate bio-optical parameters due to the extent and limitations of in-situ measurements (MERTES et al., 1993; ESPINOZA VILLAR et al., 2012; LOBO et al., 2014; PARK and LATRUBESSE, 2014). Thus, remote sensing images have long been recognized as a potential data source for the continuous modelling and monitoring of the water quality (ODERMATT et al., 2012).

The new generation of orbital optical sensors, such as Sentinel-2 and Landsat-8, presents a scientific opportunity for inland water research (PALMER et al., 2015). The Multispectral Imager (MSI) on-board Sentinel-2A delivers images with high spatial (10–30 m), temporal (10 days) and radiometric (12 bits) resolutions (DRUSCH et al., 2012). These configurations offer capabilities for the mapping of small and irregular open-water systems, higher sensitivity to bio-optical variables and higher temporal observations enabling the monitoring of changes in the water composition over time. In addition, MSI has been designed with eight spectral bands in the visible and near-infrared (NIR) wavelengths that are feasible for water research of the main optically active components (OACs): chlorophyll-a (Chl-a), total suspended solids (TSS) and coloured dissolved organic matter (CDOM) (DÖRNHÖFER et al., 2016). In a preliminary assessment of the MSI application, Toming et al. (TOMING et al., 2016) reported reasonable retrievals of Chl-a and CDOM concentrations based on a historical

[2] This chapter is an adapted version of the paper: MARTINS, V.S.; BARBOSA, C.C.F.; CARVALHO, L. A.S.; JORGE, D.S.F.; LOBO, F.D.L.; and NOVO, E.M.L.M.. Assessment of Atmospheric Correction Methods for Sentinel-2 MSI Images Applied to Amazon Floodplain Lakes. **Remote Sensing**, *9*(4), 322. 2017. (Published).

dataset from Estonian lakes. Thus, Sentinel-2 MSI data represent a new perspective for inland and coastal waters (HEDLEY et al., 2012; MALENOVSKÝ et al., 2012; MALTHUS et al., 2012).

Atmospheric correction is a prerequisite to quantify biogeochemical properties based on surface reflectance, once it removes attenuation effects caused by active atmospheric constituents, such as molecular and aerosol scattering and absorption by water vapour, ozone, oxygen and carbon dioxide (GAO et al., 2009). In fact, due to the low reflectance, the accurate removal of atmospheric effects is paramount for water surfaces (IOCCG, 2010). The surface reflectance quality is highly dependent on the atmospheric correction method, atmospheric-surface characteristics, and sensor design (OKIN and GU, 2015).

Several atmospheric correction algorithms are available for multispectral sensors which can be divided in two main categories (HADJIMITSIS et al., 2004): (i) image-based approach; and (ii) atmospheric radiative transfer codes (RTCs). In the first category, the atmospheric effects are derived from the image itself and then removed from the TOA signal. For instance, ESA provides a Sentinel toolbox that includes a Sen2Cor processor to generate MSI land products (Level 2A). This processor is a semi-empirical algorithm that integrates image-based retrievals with Look-Up tables (LUTs) from the LibRadtran model to remove atmospheric effects from MSI images (MAIN-KNORN et al., 2015). In parallel, Vanhellemont and Ruddick (VANHELLEMONT and RUDDICK, 2016) developed an image-based processor, named ACOLITE, for the atmospheric correction of OLI and MSI images applied to marine and inland water studies. The ACOLITE computes aerosol scattering using Rayleigh-corrected reflectance from NIR bands for clear water and SWIR bands for moderate and turbid water; the water contribution measured in these bands can be negligible (SHI and WANG, 2009). Overall, both ACOLITE and Sen2Cor are image-based approaches available for MSI images and present an advantage in regions without external atmospheric information. In the second category, RTCs compute scattering and absorption of light through the atmosphere to remove them from the signal measured by satellite sensors. The 6SV is a well-established RTC that accounts for a wide variety of atmospheric conditions and sensor

characteristics (VERMOTE et al., 1997b). However, the main implication of using RTC is the prior knowledge about atmospheric parameters (e.g., AOD, water vapour and ozone) coinciding with the satellite overpass. In general, this information is available from climatological models (TAYLOR et al., 2015), sun photometer measurements (HOLBEN et al., 1998) or satellite atmospheric products (KING et al., 2003). Among the alternatives, recent MODIS algorithm, named Multi-angle implementation of atmospheric correction (MAIAC), provides a suite of atmospheric products (AOD, cloud mask and water vapour) at fine 1 km resolution (LYAPUSTIN et al., 2011), which is promising for enhanced quality information in regions with high cloud cover areas such as the Amazon region (HILKER et al., 2012).

In addition to atmospheric correction issues, the contribution of adjacency effects also demands correction (KISELEV et al., 2015; STERCKX et al., 2015). In the Amazon context, the presence of dense forest around water bodies contributes to modify the water spectrum measured by orbital sensors. Therefore, remote sensing of the Amazonian water system faces several challenges, such as: (i) dynamic system with optically complex water; (ii) logistical difficulties in collecting water samples and validation data; (iii) seasonal variability of aerosol loading from biomass burning plumes (iv); high cloud cover and cloud cirrus; and (v) forest adjacency effects. In view of these challenges, the critical assessment of atmospheric correction methods applied to new Sentinel 2 MSI image is required, which is still missing for Amazon lakes.

Therefore, our objective is to present an inter-comparison of three atmospheric correction algorithms (6SV based on MAIAC atmospheric product, ACOLITE and Sen2Cor) applied to new a Sentinel-2 MSI image in the case of Amazon floodplain lakes. Regarding atmospheric correction, we conducted a supplementary analysis to understand atmospheric components in the study area, and then, simulated the contribution of atmospheric and surface reflectance to MSI TOA bands. Finally, we developed an adjacency correction based on the Linear Spectral Unmixing (LSU) model for water surfaces, due to the strong forest adjacent effects on the water spectrum. All comparisons were conducted over four Amazon floodplain lakes using in-situ radiometric measurements concurrent to the MSI image overpass.

5.2. Materials

5.2.1. Site Description and Field Data

Our study area consists of four Amazon floodplain lakes located in the Mamirauá Sustainable Development Reserve (MSDR), close to the confluence of the Solimões and Japurá Rivers (~25 km) (**Figure 5.1**). The MSDR is a complex floodplain ecosystem that remains entirely flooded for 3–6 months due to seasonal water level variation. The annual average amplitude of the water level reaches ~10.6 m (RAMALHO et al., 2009). In the MSDR lakes, OACs concentrations change seasonally driven by exchange flow (in- and out-flowing) with large fluvial systems, such as the Japurá and Solimões rivers (AFFONSO et al., 2015). Few studies reported the bio-optical properties for this Amazon region (e.g. Affonso et al. 2011), since most efforts concentrated on multidisciplinary reports about the ecological management, fish communities and ecosystem disturbance (HENDERSON et al., 1998; MACCORD et al., 2007). In general, MSDR integrates a sustainable use of natural resources and preservation practices, where local communities are committed to rational resource exploitation, and biodiversity protection in the reserve (CASTELLO et al., 2009). Thus, the MSDR represents an ecological and sustainable model for human–environment relations, and becomes an attractive region for further studies of bio-optical patterns and natural conservation using remote sensing data.

Figure 5.1. Overview of study area and sample stations over four Amazon floodplain lakes: (**a**) Buá-Buá; (**b**) Mamirauá; (**c**) Panta-leão; and (**d**) Pirarara.

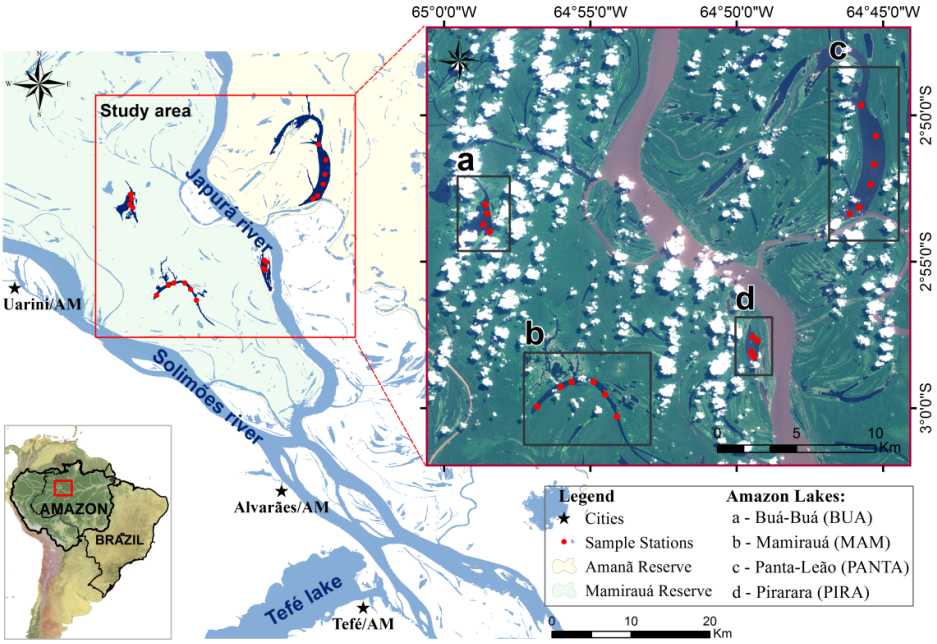

Radiometric measurements were carried out at twenty sample stations during 12–19 August 2016 (**Figure 5.1**). Inter-calibrated Trios-RAMSES radiometers were used to measure the above water upwelling radiance (L_w^{+0} [W [watt]·m^{-2}·sr^{-1}·nm^{-1}]), sky radiance (L_{sky}^{+0} [wW [watt]·m^{-2}·sr^{-1}·nm^{-1}]) and above surface downwelling irradiance (E_d^{+0} [W [watt]·m^{-2}·sr^{-1}·nm^{-1}]), within 350–900 wavelengths. The sensors view followed the framed description of Mobley (MOBLEY, 1999), whereas L_w^{+0} has a relative azimuth angle (φ_v) within 90°–135° from the sun and a zenith angle (θ_v) of 45° from the nadir, and L_{sky} has a zenith angle (θ'_v) of θ_v+ 90° from nadir. All radiometers operate simultaneously, and measurements were performed within a 3-h interval (10:00 a.m.–13:00 p.m.) to avoid potential impact of specular reflection (glint) at low sun angles. In the pre-processing, all spectroradiometric measurements were interpolated for 1 nm interval (originally ~3.3 nm) and were normalized by sky reference. The remote

sensing reflectance (R_{rs}) was calculated at each sampling station according to Mobley (MOBLEY, 1999):

$$R_{rs}(\theta_v,\varphi_v,\lambda) = \left(\frac{L_w^{+0}(\theta_v, \varphi_v, \lambda) - r_{sky}(\theta'_v, \varphi_v, \theta_0, W) \quad L_{sky}^{+0}(\theta'_v, \varphi_v, \lambda)}{E_d^{+0}(\lambda)} \right) \tag{5.1}$$

Afterwards, water reflectance (R_{w^*}) is calculated as:

$$R_{w^*} = \pi . R_{rs} \tag{5.2}$$

where, r_{sky} is the air-water interface reflection coefficient that minimizes skylight reflection effects, and can be obtained in Mobley (MOBLEY, 2015) as a function of a given view zenith and azimuth angles (θ_v; φ_v), sun zenith angle (θ_0) and wind speed W (m/s). In-situ R_{w^*} spectra were weighted by spectral response functions SRF(λ) of MSI bands, thus deriving a multi-spectral data comparable to atmospherically corrected MSI-reflectance from image.

$$R_{w,situ}(\lambda_i) = \frac{\int_k R_{w^*}(\lambda) \times SRF(\lambda)\, d\lambda}{\int_k SRF(\lambda)\, d\lambda} \tag{5.3}$$

where $R_{w,\,situ}(\lambda_i)$ is the MSI reflectance simulated from in-situ reflectance, k is bandwidth (nm), λ_i is the central wavelength of spectral band, and *i* is the number of MSI spectral band.

Figure 5.2 shows the magnitude contrast of the mean and standard deviation of R_{w^*} spectra among lakes. Although all lakes present a typical low spectral reflectance (<2%), Panta-Leão and Pirarara lakes have 2.5 times higher spectral R_{w^*} than those of Buá-Buá and Mamirauá lakes. Indeed, boundary conditions influence bio-optical differences between these lakes, and consequently, contribute to the shape and magnitude contrast of water reflectances. In this context, Mamirauá and Buá-Buá lakes, hereafter called dark lakes, receive a great amount of organic matter content due to the interaction with dense forest reaching heights of up to 40 m (WITTMANN et al. 2004). On the other hand, Panta-Leão and Pirarara lakes, hereafter called bright lakes, are

directly connected to the Japurá River and exchange a huge volume of water with high sediment loading. We therefore established all discussions based on these two distinct optical conditions; results are referred to as a function of dark and bright lakes.

Figure 5.2. Average (solid line) and standard deviation (shadow-coloured) of water reflectance measured on four Amazon lakes: Buá-Buá (BUA), Mamirauá (MAM), Panta-Leão (PANTA) and Pirarara (PIRA). The square markers and error bars are Multi-Spectral Instrument (MSI) reflectance simulated ($R_{w,situ}$) and their standard deviation, respectively.

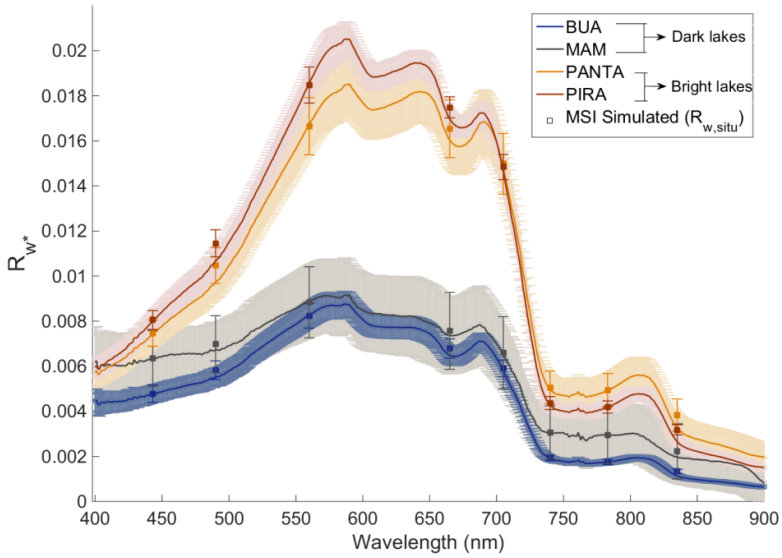

5.2.2. MSI/Sentinel-2 Data

The MSI sensor on board Sentinel-2 satellite is an optical pushbroom sensor that acquires multi-spectral data for Earth science (GASCON et al., 2014). The Sentinel-2 mission includes two identical satellites operating in sun-synchronous orbit, with operational Sentinel-2A satellite launched in June 2015, and Sentinel-2B planned for 2017. These twin polar-orbiting satellites allow a high 5-day revisit time of the equator (after the launch of Sentinel-2B), because they are phased at 180° to each other. The high-resolution MSI data include 13 spectral bands from Visible and Near-Infrared (VNIR) to Short Wave InfraRed (SWIR) region, fine spatial resolution (10, 20 and 60 m), and 12 bit quantization (**Table 5.1**) (DRUSCH et al., 2012). Additionally, the MSI sensor enhances spectral capabilities that include useful bands for land and atmospheric observations, such as the deep blue band (443 nm) for coastal and aerosol retrievals,

cirrus detection at 1375 nm and three red-edge bands for vegetation and water studies (CLEVERS; GITELSON, 2013). Therefore, all those high optical properties configure an attractive sensor for inland water studies, in particular, over high cloud cover regions (e.g., Amazon Basin) due to the high temporal resolution. The standard MSI scene is delivered as Level-1C (L1C) product with radiometric and geometric correction in UTM/WGS84 projection (BAILLARIN et al., 2012).

Simultaneously with the field observations, a cloud-free MSI image was acquired on 12 August 2016 at 14:37 UTC. Our study area is located within MSI granule 20MKB, which was downloaded from the Copernicus Scientific Data Hub website. As a first procedure, all MSI bands were resampled to a 10 m pixel size and the TOA reflectance was divided by a rescaling coefficient of 10,000. The granule has ~2% of cloud cover on granule, and particular cloud-free conditions over our twenty sample stations. Thus, in-situ measurements can be used to compare the MSI surface reflectance derived from atmospheric correction methods.

The time gap between in-situ measurements and the satellite overpass affects the reflectance comparison. Several studies discussed the time gap with respect to reservoir and lake research and the results pointed out that a comparison using measurements with ±3 or up to ±8 days is reasonable when the water and environmental conditions do not present rapid changes (KLOIBER et al., 2002; OLMANSON et al., 2008; SRIWONGSITANON et al., 2011; TEBBS et al., 2013). In our case, logistical and distances imposed difficulties to access all floodplain lakes concurrently with the satellite overpass. Thus, we started the radiometric measurements on 12 August concurrently with Sentinel-2 overpass, and were sampling new stations every day until all sample stations were completed by 19 August. The number of stations was limited to 2–3 per day to guarantee feasible solar conditions. Note that more than 50% of all sample station data were collected within three days from the satellite overpass, reducing the temporal influence on the radiometric dataset. Although the lakes exchange water with the Japurá River, variation of the water level during this season is a gradual process that relies on channel connections and hydrological periods. Additionally, all lakes presented a depth (>5 m) and low wind speed (~1 m/s) that minimize resuspension

and circulation of sediment from the bottom. Therefore, the time gap between MSI image (12 August) and in-situ measurements (12–19 August) was in principle not considered to be an issue for the comparisons.

Table 5.1. Spectral bands of MSI sensor on-board Sentinel-2 satellite.

MSI Bands (Spatial Res.)	Central Wavelength (nm)	Bandwidth (nm)	Lref ($W \cdot m^{-2} \cdot sr^{-1} \cdot \mu m^{-1}$)	SNR at Lref
Band 1 (60 m)	443 (Deep blue)	20	129	129
Band 2 (10 m)	490 (Blue)	65	128	154
Band 3 (10 m)	560 (Green)	35	128	168
Band 4 (10 m)	665 (Red)	30	108	142
Band 5 (20 m)	705 (Red-edge)	15	74.5	117
Band 6 (20 m)	740 (Red-edge)	15	68	89
Band 7 (20 m)	783 (Red-edge)	20	67	105
Band 8 (10 m)	842 (NIR)	115	103	172
Band 8A (20 m)	865 (NIR)	20	52.5	72
Band 9 (60 m)	945 (NIR)	20	9	114
Band 10 (60 m)	1375 (SWIR)	30	6	50
Band 11 (20 m)	1610 (SWIR)	90	4	100
Band 12 (20 m)	2190 (SWIR)	180	1.5	100

5.2.3. MAIAC Atmospheric Data

Several MODIS algorithms were developed to provide atmospheric products, such as aerosol optical depth, column water vapour and ozone (GAO; KAUFMAN, 2003; REMER et al., 2005a; HUBANKS et al., 2015). Continuous efforts have been made to enhance the accuracy of atmospheric retrievals from MODIS data. In addition to climate research, these atmospheric products are also used as input in the atmospheric correction of optical images (JIMÉNEZ-MUÑOZ et al., 2010). In this context, the MAIAC algorithm was developed to derive a surface bidirectional reflectance distribution function (BRDF) from MODIS data and a suite of atmospheric products at a high 1 km resolution (LYAPUSTINe A. et al., 2011). These atmospheric products include the cloud and cloud shadow mask, aerosol optical depth at 0.47 and 0.55 µm and column water vapour (U_{H2O}) (see Lyapustin et al. (LYAPUSTIN et al., 2011; LYAPUSTIN et al., 2012b for more details). **Figure 5.3** shows the MOD09 surface reflectance product and a comparison of three MODIS aerosol products for the same day of MSI image (12 August 2016): (**Figure 5.3b**) MAIAC AOD 1 km; (**Figure 5.3c**) MOD04 3 km

Collection 6; and (**Figure 5.3d**) MOD04 10 km Collection 6. There is a clear difference in the number of valid AOD retrievals between fine resolution MAIAC and MOD4 AOD products. Cloudy conditions limited the wide coverage of MOD04 retrievals at 3 and 10 km resolutions, while the fine-scale MAIAC retrieves AOD information for an individual set of cloud-free pixels. In our case, both Sentinel-2A and Terra satellite have an almost concurrent overpass (~10:30 a.m.), which guarantees fair applications of MODIS atmospheric products as auxiliary information in atmospheric correction. Thus, we selected tile h01v01 of the MAIAC atmospheric product on 12 August 2016. The average of AOD_{550} and U_{H2O} within a 2 km buffer from each lake was used as input for the 6SV model (**Table 5.2**). In addition, columnar ozone content was obtained from MODIS global daily product (MOD08_D3-Total_Ozone_mean) on 12 August 2016.

The assessment of MAIAC AOD_{550} is still missing in the Amazon region. Therefore, we performed an evaluation of this satellite AOD product by comparing it with ground measurements. In this context, AERONET program is a global sun-photometer network that provides a multi-spectral sun and sky radiance to derive aerosol optical properties, such as AOD and angstrom exponent information (HOLBEN et al., 1998). There are three long-term operational AERONET sites in the Amazon basin: Balbina (1993–2003), Belterra (1996–2005), and Manaus-Embrapa (2011–2016). These sites provide consolidated ground-truth data for the quality evaluation of satellite aerosol products. Therefore, we compared MAIAC AOD retrievals at 550 nm with AERONET observations based on procedures used by Lyapustin et al. (LYAPUSTIN et al., 2011). Besides validation of AOD products, we also calculated the monthly average of AOD_{550}, columnar water vapour and cloud cover frequency within the Mamirauá region (see red box in **Figure 5.1**) using the 15-year MAIAC Terra products (2000–2015). This temporal analysis provides background knowledge of the most variable atmospheric constituents in the study area.

Figure 5.3. MODIS AOD products concurrently with MSI image on 12 August 2016: (**a**) MOD09 surface reflectance; (**b**) MAIAC AOD_{550} 1 km; (**c**) MOD04 3 km Collection 6; and (**d**) MOD04 10 km Collection 6.

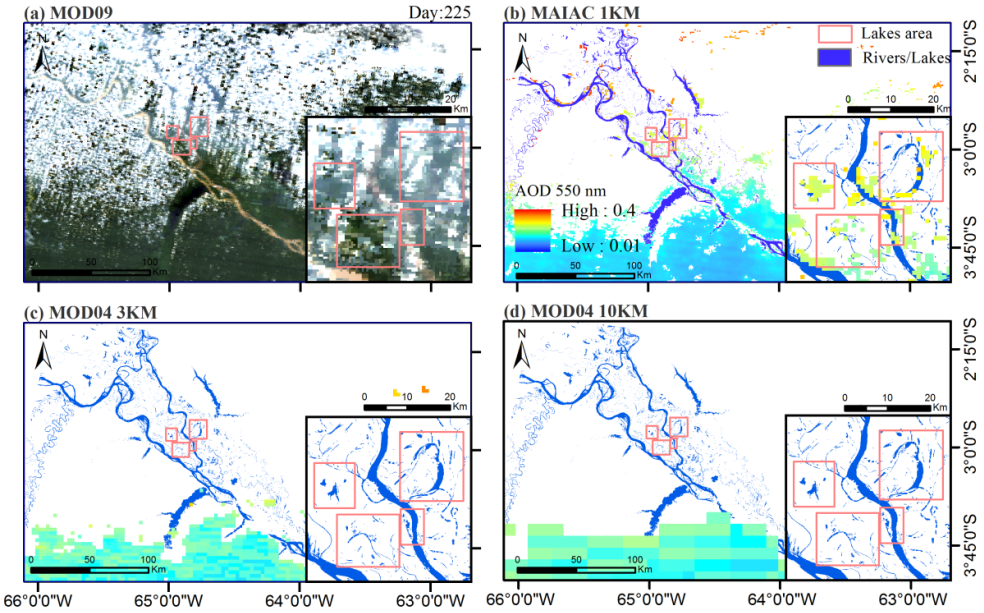

5.3. Methods

In this section, we present three atmospheric correction methods used for the MSI image and forest adjacency correction: (Section 5.3.1) 6SV model based on MAIAC AOD_{550} and U_{H2O} products; (Section 5.3.2) ACOLITE algorithm; (Section 5.3.3) Sen2Cor algorithm; and (Section 5.3.4) forest adjacency correction based on the LSU model. Based on the MSI-corrected image, we calculated the average of water surface reflectance using a 3 × 3-pixel box centered at each sample station to perform a direct comparison with in-situ measurements.

5.3.1. 6SV Model + MAIAC Atmospheric Products

The 6SV model is a robust radiative transfer code for the atmospheric correction of different satellite data for a variety of climatological conditions (VERMOTE et al., 1997b). The atmospheric radiative transfer computes attenuation effects caused by the scattering of molecules and aerosols and gaseous absorption by water vapour (H_2O),

carbon dioxide (CO_2), oxygen (O_2), and ozone (O_3). Currently, the 6SV model is an operational model used to derive the surface reflectance product from MODIS, ETM+ and OLI images (VERMOTE; KOTCHENOVA, 2008; VERMOTE et al., 2016). The comparison of 6SV with other complex RTCs, such as SHARM, DISORT and MODTRAN, showed that the vector mode is highly accurate and provides fair agreement results that agree with other RTCs (KOTCHENOVA et al., 2006). Due to consistency of multiple sensors and generic features, we used the 6SV model (version 1.1) to evaluate the atmospheric correction of the MSI image. For a given sun-view geometry, sensor characteristics, atmospheric condition and surface reflectance (R_{sur}), TOA reflectance can be estimated with the following Equation (5.4) (VERMOTE et al., 1997b):

$$R_{TOA}(\lambda, \theta_v, \varphi_v, \theta_0, \varphi_0) = \Big[R_{R+A}(\lambda, \theta_v, \theta_0, \varphi_0) + t_d(\lambda, \theta_0) t_u(\lambda, \theta_v) \frac{R_{sur}(\lambda)}{1 - S(\lambda) R_{sur}(\lambda)}\Big] T_g(\lambda, \theta_v, \theta_0,) \quad (5.4)$$

where T_g refers to gaseous transmission of the principal absorbing constituents (O_2,O_3,CO_2, H_2O); R_{R+A} is the molecular and aerosol scattering intrinsic reflectance; t_d and t_u represent the atmospheric transmittance of aerosol and molecular from sun to target and target to sensor, respectively; S is the atmosphere spherical albedo of the atmosphere; and θ_v, φ_v, θ_0, φ_0 are the view zenith, view azimuth, solar zenith and solar azimuth angles, respectively. Solving Equation (5.4) for surface reflectance and simplifying notations of angles, the atmospheric correction proceeds as following Equation (5):

$$R_{sur} = \big(R_{TOA}/T_g - R_{R+A}\big)/\big[t_d t_u + S\big(R_{TOA}/T_g - R_{R+A}\big)\big] \quad (5.5)$$

These atmospheric quantities are internally generated when running the model. In this study, the 6SV model was set to MSI bands using a spectral response function. Subsequently, the code was run for each subset of the MAIAC-based atmospheric data according to each lake, applying water vapour (U_{h_2O}, measured in $g \cdot cm^{-2}$), ozone content (U_{O_3}, measured in $cm \cdot atm^{-1}$), aerosol model and AOD at 550 nm described in

Table 5.2. We selected a biomass burning model based on the global aerosol mixture from Taylor et al. (TAYLOR et al., 2015), which indicated a dominance of biomass burning particles in August in the Mamirauá region (biomass burning: 72%, Sulphate: 22.8%, Maritime: 2.5%, and Dust: 2.7%). The sun angles, date and time of the image acquisition were obtained from the image metadata.

To understand the contribution of the atmosphere and surface to the TOA signal measured by MSI sensor, and to assess the atmospheric effects according to spectral bands, the TOA reflectance was simulated from the above mentioned water reflectance for each lake (Equation (3)). This theoretical TOA reflectance was simulated using the average AOD of August in the lakes (BUA: 0.178; MAM: 0.188; PANTA: 0.181; and PIRA: 0.19), biomass burning model, tropical atmosphere profile, and the average of in-situ reflectances from each lake.

Table 5.2. Input parameters of 6SV model for Sentinel MSI image.

Parameters	**BUA**	**MAM**	**PANTA**	**PIRA**
Solar zenith angle (°)	30.96	30.96	30.96	30.96
Solar azimuth angle (°)	53.99	53.99	53.99	53.99
Aerosol Model	------- Biomass Burning -------			
AOD at 550 nm [1]	0.3	0.26	0.34	0.3
Ozone (cm-atm)	0.346	0.346	0.346	0.346
Water vapour (g/cm^2)	4.88	4.7	4.06	4.15
Terrain elevation (km)	0.04	0.04	0.04	0.04

[1] AOD adjusted by Terra bias (Section 4.1).

5.3.2. ACOLITE Algorithm

The Atmospheric Correction for OLI "lite" (ACOLITE) algorithm was developed for the atmospheric correction of OLI/Landsat 8 and MSI/Sentinel 2 images for ocean and inland water studies (VANHELLEMONT; RUDDICK, 2014; 2015; VANHELLEMONT; RUDDICK, 2016). The ACOLITE algorithm removes scattering effects of molecular and aerosol components over clear and turbid water. The Rayleigh scattering was corrected using LUTs from the 6SV model, while aerosol scattering was estimated based on the NIR (842 and 865 nm) bands for clear water and SWIR (1610

and 2130 nm) bands for moderate and turbid water (VANHELLEMONT; RUDDICK, 2015). These bands are very useful to decouple the aerosol reflectance, because the water contribution can be assumed to be negligible. Thus, the aerosol reflectance is retrieved at those bands and extrapolated to VNIR wavelengths based on aerosol type (ε) or on ratio of Rayleigh corrected reflectance in these infrared bands.

The algorithm (version 2016.05.20) allows the user to choose some inputs for the atmospheric correction: (i) derive ε fixe on scene, per pixel or user-defined; (ii) gain factors for radiometric calibration (FRANZ et al., 2014; PAHLEVAN et al., 2014); (iii) atmospheric pressure; (iv) smooth window applied to aerosol reflectance values; and (v) cloud mask threshold (default: 0.0215 on the 1610 nm band). In our study, atmospheric correction was performed using the SWIR band approach, as recommended for turbid water (VANHELLEMONT; RUDDICK, 2015); aerosol correction per-pixel; a smooth window of 25 pixels; and cloud dilatation of 16 pixels (default).

5.3.3. Sen2Cor Algorithm

The Sentinel 2 MSI data are distributed as ortho-image TOA reflectance products. To derive the MSI land products at Level-2A, the Sentinel toolbox provides the Sen2Cor processor for atmospheric correction and scene classification (MAIN-KNORN et al., 2015). As a module of the Sen2Cor algorithm, an operational atmospheric correction is applied to the MSI spectral bands to retrieve atmospheric parameters from the image itself, with cirrus correction in a channel at 1375 nm; water vapour retrieval based on the B8A and B9 bands (865, 945 nm) and AOD retrieval (MULLER-WILM et al., 2013). Thus, the algorithm performs a semi-empirical approach that associates image-derived atmospheric properties with the pre-computed Look-up table (LUT) from libRadtran radiative transfer model. The advantage of this image-based approach is that is supports the application in regions without climatological information. The spectral relation of the reflectance of B4 (665 nm) and B2 (490 nm) bands with B12 (2190 nm) band is used for the AOD retrievals in reference areas, such as dense dark vegetation (DDV) surfaces (KAUFMAN et al., 1997a). In the Amazon region, DDV surfaces around lakes benefit AOD retrievals due to the strong reflectance relation between

visible and SWIR bands and temporal stability in these preserved areas. When these vegetated areas are not available on scene, the algorithm identifies dark soil and water surfaces, or applies a default visibility of 20 km. To run the Sen2Cor algorithm (version 2.2.1), we chose the rural aerosol, ozone content of 330 D.U., smooth window of 100 × 100 m^2 box applied to the water vapour map, and adjacency correction within the 1000 × 1000 m^2 box.

5.3.4. Adjacency Effect Correction

Adjacency effects are an optical-physical process caused by molecular and aerosol scattering where the target view is affected by radiation reflected from neighbourhood surfaces (TANRE et al., 1981). These multiple scattering regimes of photons from adjacent areas modify the spectral signal of the target pixel. The magnitude of these effects depends on the: (i) atmospheric turbidity, at a particular aerosol scattering phase function; (ii) spectral contrast of the surface reflectance; and (iii) sensor characteristics (OTTERMAN, 1979; KAUFMAN, 1984; CHERVET et al., 2002). The influence of atmospheric scattering on adjacency effects increases as a result of the high optical thickness (DOR et al., 2001). This impact produces blurring effects that distort the effective spatial resolution, reduce the apparent surface contrast and affect the land cover characterization (KAUFMAN, 1984; HUANG et al., 2002). In case of Sentinel-2 MSI, the actual spatial resolution allows discrimination of small water bodies (RADOUX et al., 2016), however, atmospheric scattering might change the effective pixel size and quality of the image according to aerosol microphysical properties (particle-size distribution, composition, and particle shapes) and loading (CHERVET et al., 2002). Moreover, the target spectrum is more susceptible to adjacency effects in heterogeneous areas, especially, at high-spatial resolution (SEI, 2015). In coastal and inland waters, these effects are more evident due to typical lower reflectance in relation to their neighbourhood surfaces, such as sand close to coastal waters and vegetation around reservoirs and lakes (STERCKX et al., 2015).

In our study, the large contrast of reflectance between forest and water surfaces contributes to spectral distortions of water-pixels, particularly, in the NIR signal

(**Figure 5.4**). For example, the water spectrum of the Mamirauá Lake is highly affected by the forest neighbourhood, due to the typical low reflectance (<1%) and narrow width (200–400 m between margins). Therefore, this phenomenon requires careful evaluation and several studies have proposed solutions (see, for example, Duan et al. 2015 and references therein). For example, previous applications derived the contextual information, known as an environmental reflectance function, based on the distance-weighted average reflectance of neighbouring pixels and ratio of direct and diffuse transmittance for adjacency correction (TANRE et al., 1981; VERMOTE et al., 1997b). However, this environmental reflectance is a critical issue when it is applied to areas with significant spectral contrast between surfaces, such as water and land targets (KISELEV et al., 2015). In addition, different procedures were developed based on atmosphere point spread function (PSF) to quantify surrounding contributions and synthesize the filter correction of the neighbouring reflections (DUAN et al., 2015; KISELEV et al., 2015). Although these methods are routinely used for adjacency correction, the image-based scheme provides a practical sense for remote sensing users and overcomes limitations of atmospheric parameters that are not always available in remote areas such as the Amazon.

Since adjacency effect consists of spectral mixing problems, we performed a simple procedure to decouple water and forest contributions using Linear Spectral Unmixing model (LSU) (BURAZEROVIC et al., 2012). The main idea of the LSU model is to decompose the surface reflectance contributions of mixed pixels based on the pure spectrum collection of their surfaces, called endmembers. In this sense, mixed spectrum is given by the linear sum of distinct proportion of each endmember (Equation (5.6)) and LSU model provides fraction maps of surface contributions per pixel (KESHAVA and MUSTARD, 2002).

$$R_i = ff_{1,i} \times R_{1,i} + ff_{2,i} \times R_{2,i} + \ldots + ff_{M,i} \times R_{M,i} + w$$
$$= \sum_{n=1}^{M} ff_{n,i} \times R_{n,i} + w \qquad (5.6)$$

where R is the reflectance of pixel, ff is the contribution fraction, R_M is the spectral reflectance of endmember (M), M is the number of endmembers, w is an error term accounting for additive noise (including sensor noise, endmember variability, and other model inadequacies) and i = [1, 2,…, i_n] is the number of spectral bands.

Briefly, this adjacency correction procedure is described in the following steps: (i) selection of water and forest endmembers as an input for the LSU model; (ii) calculation of the adjacency contribution based on a forest fraction map; and (iii) adjacency removal per water pixel of each lake. The selection of the water endmember is critical when all water-pixels are highly affected by adjacency effects. Thus, two main assumptions were made: (i) prior knowledge of the typical water reflectance as input for the LSU model; and (ii) the forest is the only adjacency surface that distorts the water spectrum. Based on these assumptions, we selected the highest spectrum of each sample station to calculate the average of water reflectance per lake (**Table 5.3**). For forest reference, five random spectra were selected over a vegetated area with NDVI > 0.8 up to 5 km from the lake (example in **Figure 5.4**). The average of these vegetation spectra is referred to as forest endmember per lake (**Table 5.3**).

Figure 5.4. Example of water and forest endmembers selection at Mamirauá Lake. (a) Random points in the forest surface near to Mamirauá Lake. (b) Water and forest endmembers (**Table 5.3**).

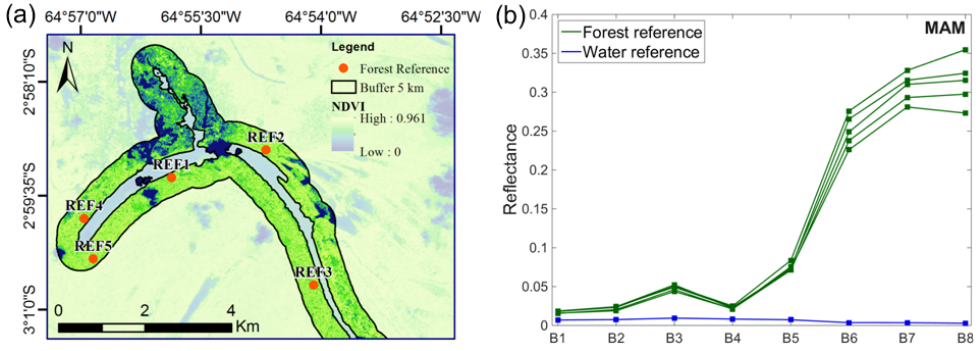

After running the LSU model, the forest fraction mapping of the lake was multiplied by forest reference spectrum to estimate adjacency effects for all water-pixels (Equation 5.7), which were then removed from the MSI surface reflectance derived from the 6SV model (Equation 5.8).

$$R_{adj,\,i}(x_n, y_n) = R_{fpure,\,i} \times ff_i(x_n, y_n) \quad (5.7)$$

$$R_{cor^*,\,i}(x_n, y_n) = R_{cor,\,i}(x_n, y_n) - R_{adj,\,i}(x_n, y_n) \quad (5.8)$$

where R_{adj} is the forest adjacency effects, R_{fpure} is the forest reference spectrum (**Table 5.3**), ff is the fraction of forest signal affecting the water spectrum, R_{cor} is the MSI-corrected image from 6SV model, R_{cor^*} is the adjacency corrected image, $x_n = [x_1,\ldots, x_n]$ is the column of pixel n, $y_n = [y_1,\ldots, y_n]$ is the row of pixel n over water surface, and i = [1 ,…, 8] is the number of spectral band. Finally, the adjacency corrected MSI image was also evaluated with in-situ measurements.

Table 5.3. Water and forest endmembers selected as input to LSU per lake.

Lake	Type	B1	B2	B3	B4	B5	B6	B7	B8
BUA	Water	0.005	0.006	0.008	0.007	0.006	0.002	0.002	0.002
	Forest	0.023	0.031	0.062	0.030	0.096	0.289	0.341	0.343
MAM	Water	0.007	0.008	0.009	0.008	0.007	0.004	0.004	0.003
	Forest	0.017	0.022	0.048	0.023	0.075	0.251	0.306	0.313
PANTA	Water	0.008	0.011	0.017	0.017	0.016	0.006	0.006	0.005
	Forest	0.009	0.015	0.042	0.019	0.072	0.249	0.300	0.296
PIRA	Water	0.008	0.012	0.019	0.018	0.015	0.005	0.004	0.003
	Forest	0.017	0.023	0.050	0.025	0.077	0.253	0.312	0.329

5.4. Results and Discussion

The results will be presented in the following sequence: (i) validation of MAIAC AOD_{550} product in the Amazon region; (ii) seasonal distribution of AOD_{550}, U_{H2O} and cloud cover over the study area; (iii) simulation of the TOA reflectance of the MSI spectral bands; (iv) inter-comparison of three atmospheric methods applied to the MSI image from 12 August 2016; and (v) forest adjacency correction based on the LSU model.

5.4.1. Evaluation of MAIAC AOD_{550}.

Figure 5.5 shows a comparison between the average of AERONET measurements within ±30 min of MODIS overpass and the average of MAIAC AOD_{550} within a 25 ×

25 km^2 area. The agreement between the satellite and ground measurements was assessed using a linear regression model and the standard expected error (EE) of MODIS atmospheric products (dashed red lines) defined by AOD = ± 0.05 ± 0.15 × AOD (REMER et al., 2005). EE is the number of MAIAC retrievals falling within the standard expected error, and Remer et al. (REMER et al., 2005) suggested that EE threshold of 66% represents a satisfactory accuracy of the satellite AOD retrievals. The number of match-ups for Terra (245) was higher than that for Aqua (67), due to the difference of the cloud cover between morning and afternoon periods. In general, our results showed that both Terra and Aqua products agree well with AERONET measurements, with both slope of linear regression and correlation coefficient (R) higher than 0.74. For comparison, the Aqua product presents a slightly better accuracy than that of Terra, with a mean ratio of 1.03 for Aqua and 0.8 for Terra. In this context, forest surfaces represent feasible areas for a strong relation of visible and SWIR bands used for the DDV approach (KAUFMAN et al., 1997a) and an increase the sensitivity of aerosol scattering effects in TOA reflectance (SEIDEL and POPP, 2012). Finally, the quality of MAIAC retrievals over the Amazon region are also observed by the number of AOD retrievals falling within standard expected error that presented EE values higher than 66% threshold (EE is 76.7% for Terra and 88.1% for Aqua). To increase the confidence in the AOD product as input for 6SV atmospheric correction, AOD values obtained from MAIAC Terra were corrected (AODcorrected = AOD × 1/0.803) using a mean ratio of 0.803 (see in Figure 5.5).

Figure 5.5. Scatter plot of MAIAC AOD_{550} (y-axis) compared to AERONET AOD_{550} data (x-axis) from three sites in the Amazon region: Balbina, Belterra and Manaus-Embrapa. Solid blue and grey lines are the linear regression fits for Terra and Aqua, respectively. Red dashed lines are the MODIS standard expected error intervals ($\Delta AOD = \pm 0.05 \pm 0.15 \times AOD$) (REMER et al., 2005b). Text box: Regression equation, correlation coefficient (R), match-ups (n), root mean square error (RMSE), mean ratio ($\overline{AOD}_{MAIAC}/\overline{AOD}_{AERONET}$), and EE is the number of retrievals falling within standard expected error.

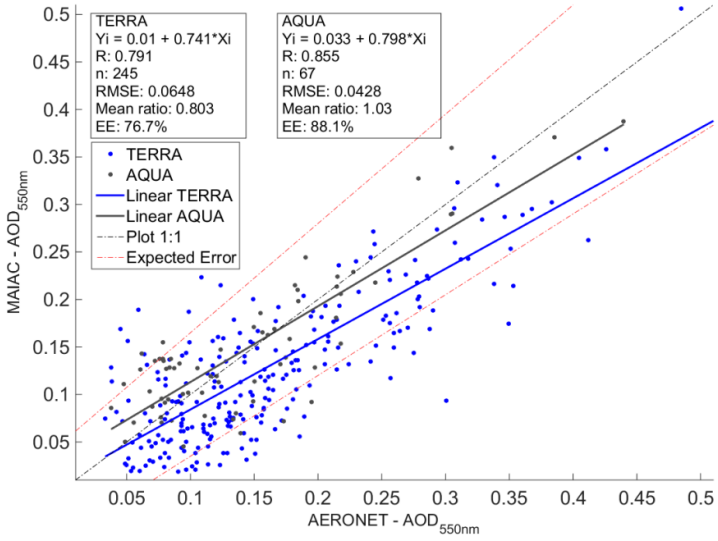

5.4.2. Background of Atmospheric Constituents

The seasonal variability of atmospheric constituents imposes distinct conditions for atmospheric correction and the background information of these constituents is desirable to understand the effects on remote sensing data (KONDRATYEV et al., 1992). **Figure 5.6** presents the monthly average of AOD_{550}, U_{H_2O} and cloud cover frequency using 15-year MAIAC Terra products in the study area (red box in Figure 5.1). The results showed that atmospheric components have distinct patterns between the first and second half of the year. In the first half of the year, high frequency cloud cover (~90%) was observed, which restricts continuous remote sensing observations of the Mamirauá region in this particular period. However, the probability of cloud-free images increases in July, August, and October, when the cloud cover decreased to 60%–80%. Hilker et al. (2015) also reported an increase of cloud-free pixels (40%–60%) in June, July and August based on MAIAC Terra observations from 2007 over the Amazon region and pointed out MAIAC improvements to detect small cloud-free areas

compared with the previous MOD09 product. Under these conditions, the temporal resolution of Sentinel 2 MSI images has the potential to increase the probability of cloud-free images over this tropical region thanks to a high five-day revisit scheduled for 2017. In parallel with cloud cover, AOD presents a remarkable seasonal variation in the first and second half of the year. In general, a low AOD (0.02–0.18) is typically observed throughout the year, however, the first half of the year registers the lowest AOD values (0.1–0.14), while the AOD values increase to 0.16–0.18 between August and November. Castro et al. (VIDELA et al., 2013) also found typical low AOD values in the Northern Amazon region (see TD1 region), and illustrated the variability between the first and second half of the year caused by local fires. Fires are the cheapest and most effective way for local communities to clear areas in order to introduce pasture and agricultural cultures (ARTAXO et al., 2013) and can be intentionally used to dissipate insect pests. Therefore, the temporal variation of AOD values imposes particular conditions for atmospheric correction depending on the period, and needs further attention during the second half of the year.

The Mamirauá region has high concentrations of water vapour (4.2 – 4.7 $g.cm^{-2}$), with quasi-permanent concentration throughout the year. Vermote et al. (1997b) showed that U_{H2O} content (variation of 0.5–4.1 $g.cm^{-2}$) implicates on higher atmospheric effects on the reflectance magnitude in the NIR region (3.4%–14.0%) than those for visible bands (0.5%–3.0%) of the Landsat 5 TM bands. Therefore, remote sensing applications using NIR bands should consider the temporal variability of this constituent, for example to vegetation indices. Our field campaign was performed during August, with the lowest cloud cover conditions (~62%) of the year, despite facing the highest AOD and water vapour concentrations. To better understand the atmospheric and surface contributions, we conducted a TOA simulation using the average AOD over the four lakes for the dataset from August, as shown in Section 5.4.3.

Figure 5.6. Monthly average of aerosol optical depth (AOD) at 550 nm, water vapour content and cloud cover from MAIAC Terra (2000–2015) in Mamirauá region (see red-box in Figure 5.1).

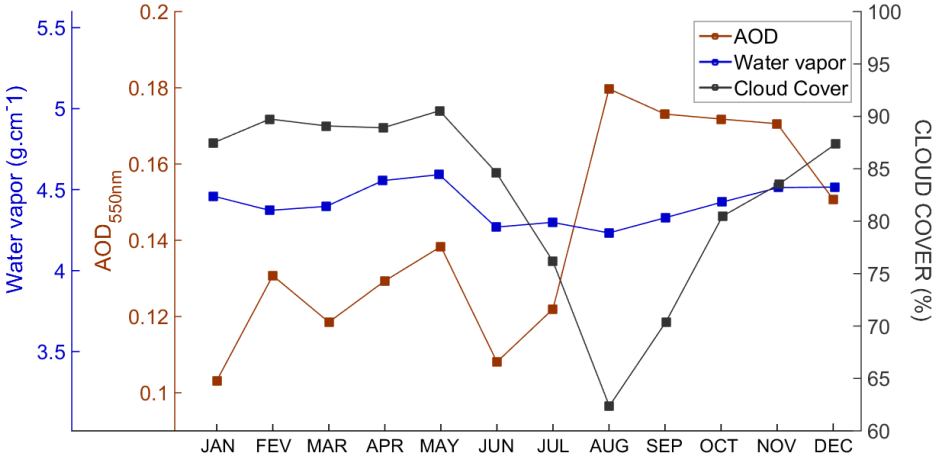

5.4.3. TOA Simulation Analysis

The contribution of atmosphere and surface reflectance from four Amazonian lakes to the TOA reflectance of MSI spectral bands was simulated using the AOD average of August (**Figure 5.7**). The major fraction of theTOA signal is due to atmospheric effects, whose contribution is higher than 75% and 50% over dark and bright lakes, respectively, for all MSI spectral bands. Because atmospheric scattering effects exponentially decay from shorter to longer wavelengths (BODHAINE et al., 1999), deep blue and blue bands are affected the most by atmospheric signals—representing more than 84% of TOA reflectance. The highest lake surface contribution was observed for red (B4) and red-edge (B5) bands, where the scattering of suspended inorganic particles in the water column increases surface reflectance, which reached ~43% of the TOA reflectance in the Panta-leão Lake. On the other hand, the contribution of dark lakes to TOA reflectance reduced dramatically, mainly in the deep blue band, when compared with bright lakes. For example, the Buá-Buá reflectance had a critical fraction that reached ~4.8% in the deep blue band, which clearly shows the difficulty in accurately removing of atmospheric effects over these low-reflectance surfaces. These results suggest that caution is required when the TOA reflectance band ratio is used to retrieve water quality parameters, even when the algorithms present a better correlation

using the TOA reflectance compared with surface reflectance (TEBBS et al., 2013). The atmospheric effects among the bands are quite different, and band ratio therefore does not remove all atmospheric effects.

In fact, the atmospheric correction is a challenging issue for water quality studies, because inaccuracies of the surface reflectances propagate errors to water quality retrievals. For example, the mapping of CDOM concentration using blue and green bands (KUTSER et al., 2005) requires an efficient removal of scattering effects of these (most affected) bands, where atmospheric effects can contribute up to 80% of the TOA signal over dark lakes. On the other hand, red and red-edge bands applied to model TSS concentrations are less affected by atmospheric effects (MATTHEWS, 2011). These examples thus illustrate that OACs modelling also requires a better understanding of atmospheric optical properties to derive accurate surface products.

Figure 5.7. Simulation of TOA reflectance based on month average AOD in August (biomass burning model) and average of water reflectance from four Amazon floodplain lakes. The table at the top right shows the percentage of atmospheric and surface contribution in TOA reflectance simulated for MSI VNIR bands.

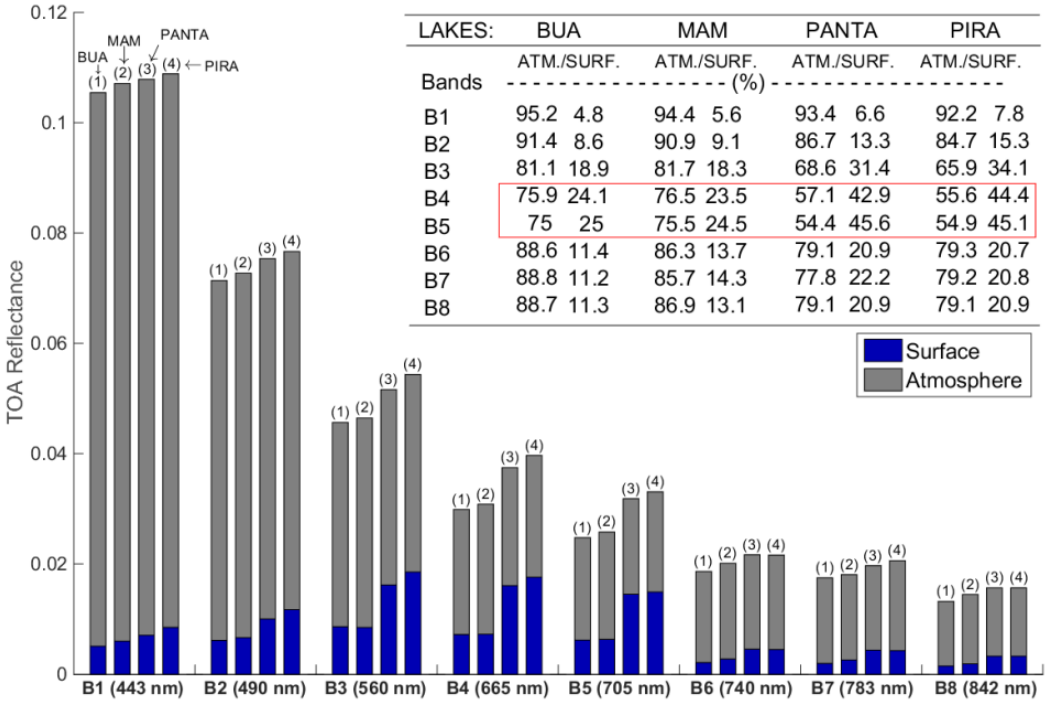

LAKES:	BUA		MAM		PANTA		PIRA	
	ATM./SURF.		ATM./SURF.		ATM./SURF.		ATM./SURF.	
Bands	(%)							
B1	95.2	4.8	94.4	5.6	93.4	6.6	92.2	7.8
B2	91.4	8.6	90.9	9.1	86.7	13.3	84.7	15.3
B3	81.1	18.9	81.7	18.3	68.6	31.4	65.9	34.1
B4	75.9	24.1	76.5	23.5	57.1	42.9	55.6	44.4
B5	75	25	75.5	24.5	54.4	45.6	54.9	45.1
B6	88.6	11.4	86.3	13.7	79.1	20.9	79.3	20.7
B7	88.8	11.2	85.7	14.3	77.8	22.2	79.2	20.8
B8	88.7	11.3	86.9	13.1	79.1	20.9	79.1	20.9

5.4.4. Inter-Comparison of Atmospheric Correction Methods

The atmospheric correction performances of three algorithms were assessed using the mean ratio ($\overline{R}_{sur}/\overline{R}_{w,situ}$) and root mean square error (RMSE). The performances are better when the mean ratio is close to unity and RMSE is low. The mean ratio also expresses a relative error, when the values are higher than 2, or relative error is 100%, exceed the maximum bias accepted here. This threshold is important for bio-optical models, because the high inaccuracy of the reflectance affects, for example, the COA retrievals (see Odermatt et al. (2012) for distinct bio-models).

Figure 5.8 presents the comparison of the in-situ measurements acquired at four Amazon floodplain lakes with spectra results from the three atmospheric correction methods, while Figure 5.9 describes the algorithm performance based on the mean ratio and RMSE. The three methods were capable of removing most of the atmospheric effects, where the reflectance magnitude mainly changed from TOA reflectance of ~12%–14% to surface of ~1%–2% of the deep blue and blue bands (**Figure 5.8**). Before atmospheric correction, TOA reflectance was a typical exponential spectrum dominated by Rayleigh and aerosol scattering effects. After correction, even with caveats, the MSI-corrected spectra (dark blue lines in **Figure 5.8**) presented a shape close to that of the in-situ measurements (light blue lines in **Figure 5.8**). The results showed that the quality of the MSI-corrected reflectance varies depending on the atmospheric correction method, spectral band, and lake characteristics.

In general, Sen2Cor produced the smallest overall RMSE and the best MSI-corrected shape compared with in-situ data (**Figure 5.9**), while the spectral shape of ACOLITE showed a bias varying per sample station. The 6SV method provided a quite similar spectral shape in the visible region for bright lakes (RMSE < 0.006), but the reflectance magnitude was higher than that of the in-situ measurements (**Figure 5.9c**). Regarding the comparison among lakes, the MSI-corrected reflectance of bright lakes is closer to that of the in-situ measurements than to that of dark lakes; all methods have a mean ratio of ~0.5–1.5 in the visible bands (**Figure 5.9a–c**).

In dark lakes, ACOLITE and Sen2Cor showed quite similar RMSE values in the blue, green and red bands (RMSE ~0.006) (**Figure 5.9b**), while 6SV was clearly limited under these low reflectance conditions (RMSE ~0.011), with a mean ratio exceeding the maximum threshold (>2) for all spectral bands (**Figure 5.9a**). In contrast, the MSI-reflectance corrected by the 6SV model had a lower RMSE (~0.006) and mean ratio of ~1.2–1.50 (overestimation) in the visible bands over bright lakes, compared with the in-situ measurements (**Figure 5.9c**). The generic design of 6SV model includes standard aerosol types for land applications, such as biomass burning, urban, continental, desert, and maritime. Bassani et al. (2015) highlighted the impact of the reflectance accuracy on coastal water when the standard 6SV aerosol use does not characterize the local aerosol microphysics. In our case, a complex mixture of natural biogenic and biomass burning particles over the central Amazon (ARTAXO et al., 2013) imposes a constraint for standard aerosol use, which might explain some limitations of the radiative transfer simulation in order to remove atmospheric effects. In addition, satellite aerosol retrievals are susceptive to several uncertainty sources, such as sensor calibration, cloud screen, aerosol models and surface properties (LI et al., 2009), which also help to explain the errors derived from the 6SV correction based on MAIAC product. Since most bio-optical models apply water surface reflectance mainly to visible bands (B1–B5) (ODERMATT et al., 2012), Sen2Cor and 6SV results produce a reasonable spectral shape compared with the in-situ measurements for bright lakes; although they overestimate the reflectance magnitude (**Figure 5.8b–f**).

Figure 5.8. Comparison between MSI reflectance simulated from in-situ measurements, MSI TOA reflectance and MSI-corrected reflectance from three methods: 6SV model based on MAIAC product (**a**,**b**); ACOLITE (**c**,**d**); and Sen2Cor (**e**,**f**). The left column shows reflectance spectra from dark lakes (Buá-Buá and Mamirauá) and, the right column shows reflectance spectra from bright (Pirarara and Panta-Leão) lakes.

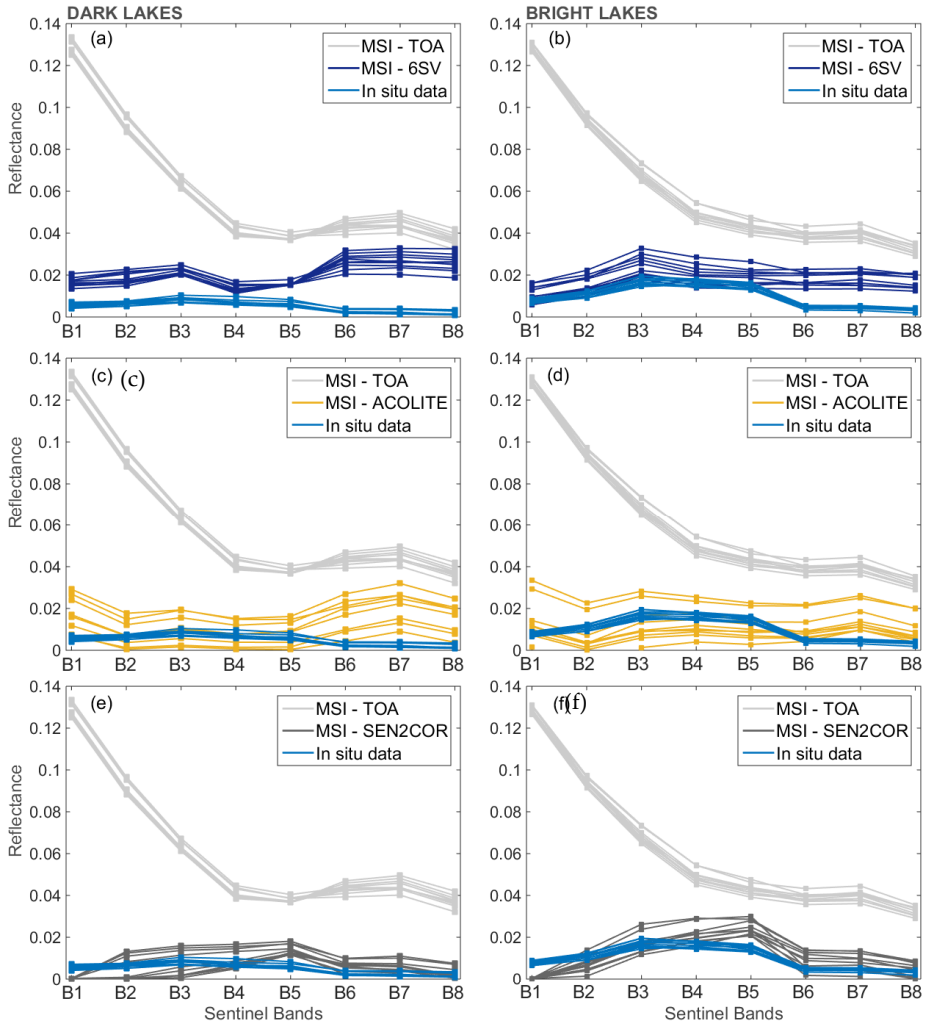

In the visible bands, the ACOLITE method produced distinct reflectance accuracy among the lakes, where water reflectance was overestimated (mean ratio ~1.1–1.5, except for B1) for dark lakes (**Figure 5.9a**) and underestimated (mean bias ~0.63–0.8, except for B1) for bright lakes (**Figure 5.9c**). A strong influence of the per-pixel correction was also observed; the random spatial error contributed to biases in the MSI-corrected reflectance for each sample station, while the 6SV produced a spatially

correlated error due to the assumption of homogeneous atmospheric effects on lakes. The ACOLITE-SWIR approach requires a high signal-to-noise ratio (SNR) for the accurate quantification of the aerosol effect on TOA reflectance particularly because the effective aerosol scattering is relatively lower at longer wavelengths (ECK et al., 1999) and accurate aerosol reflectance can be affected by a low SNR. Thus, the propagation of noisy aerosol reflectance from SWIR bands (SNR of 100, see **Table 5.1**) to the atmospheric correction of visible bands might explain the spatial variability of error in ACOLITE reflectance retrievals. Therefore, an optional smooth window applied to SWIR bands becomes essential to filter and minimize undesirable effects (VANHELLEMONT; RUDDICK, 2016). Although the ACOLITE produced variable errors in this study, the algorithm has been extensively used for the atmospheric correction of OLI images with satisfactory experiences in coastal and maritime water, for example, sediment plume mapping in the Florida offshore, USA (BARNES et al., 2015), and for turbidity quantification in the Wadden Sea, Germany (GARABA; ZIELINSKI, 2015). Our assessment represents preliminary experience with ACOLITE applied to Sentinel 2 MSI over floodplain water, and further evaluations could contribute to consolidate this image-based approach.

The Sen2Cor algorithm achieves very similar errors for both types of lakes, with RMSE between ~0.003–0.011 for all spectral bands (**Figure 5.9b–d**), and better mean ratio for blue, green and red bands (grey marker in **Figure 5.9a–c**). In fact, the presence of dense forest close to Amazon floodplain lakes provides feasible areas required for DDV application used by the Sen2Cor algorithm. Although an extensive validation has not been performed yet, first results of the comparison between Sen2Cor AOD retrievals over DDV areas and ground measurements led to an AOD uncertainty of about 0.03 (LOUIS et al., 2016), which affects the atmospheric correction accuracy of Sen2Cor algorithm. Toming et al. (TOMING et al., 2016) found the shape similarity of MSI-corrected dataset using the Sen2Cor algorithm compared with a historical dataset (2011–2013), although the MSI reflectance spectra were overestimated by the algorithm. In the Amazon context, the presence of forest surfaces benefits AOD

retrievals by the Sen2Cor algorithm, however, this surface neighbour also implies in severe adjacency contamination on the water spectrum measured by orbital sensors.

Figure 5.9. The mean ratio and RMSE for atmospheric correction methods from: dark lakes (**a**,**b**); and bright lakes (**c**,**d**). The left column shows the mean ratio ($\overline{R}_{sur}/\overline{R}_{W,situ}$), with better cases being close to unity, and the right column shows the root mean square error (RMSE). Note that all mean ratio values higher than maximum bias accepted here are represented as 2.

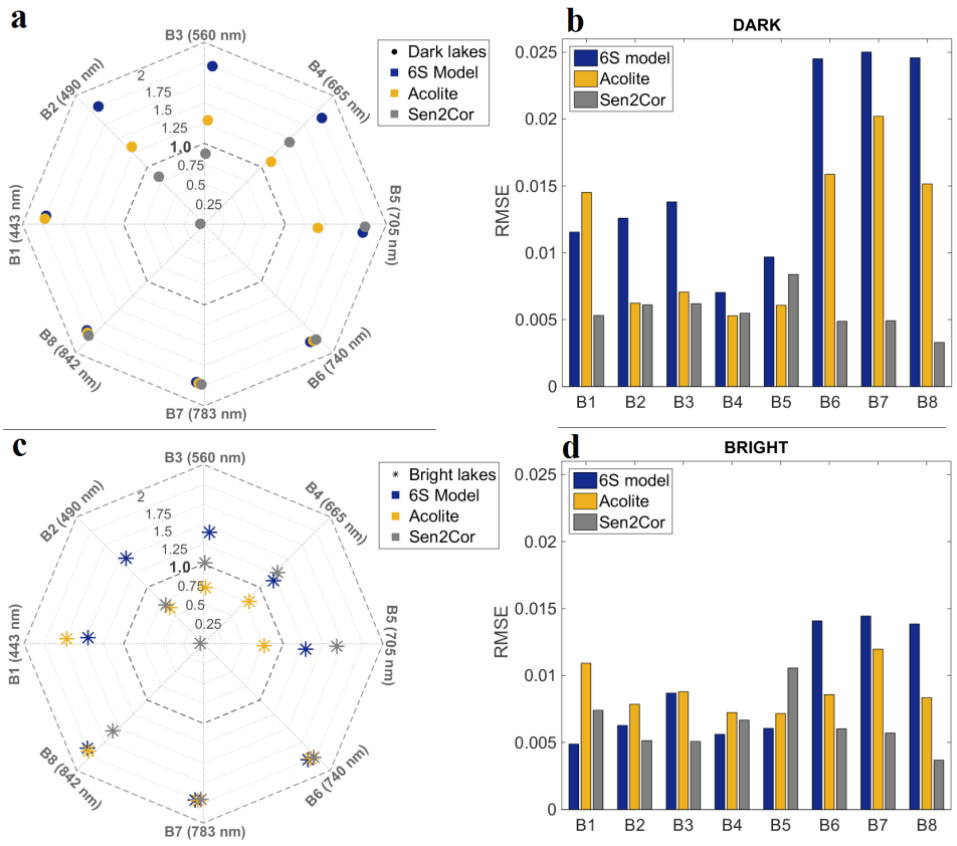

5.4.5. Adjacency Effect Correction

Large differences between forest and water reflectance contribute to strong adjacency effects on the water spectrum in the NIR region. For spectral bands above 705 nm, Sen2Cor correction minimizes the adjacency effects over dark lakes leading to a lower RMSE (<0.005) compared with ACOLITE and 6SV (RMSE > 0.013) (**Figure 5.9b–d**). Nevertheless, none of the methods presented a suitable performance to remove forest adjacency effects in the NIR region, with a mean ratio exceeding 2 (**Figure 5.9a–c**).

Dornhofer et al. (DÖRNHÖFER et al., 2016) evaluated the Sen2Cor and ACOLITE performances for bio-optical models in marine water and found an underestimation of the surface reflectance in the visible region for both methods and adjacency effects on the NIR bands due to sand surface of the shoreline. The adjacency correction applied by Sen2Cor is limited over low reflectance surfaces; methods focusing on water surfaces are required for a high spatial resolution (DUAN et al., 2015).

Figure 5.10 presents the adjacency correction based on LSU model applied to the MSI water reflectance from dark and bright lakes. The results showed that the adjacency correction improves the quality of water reflectance of all spectral bands. In both dark and bright lakes, MSI reflectance exhibits a better agreement with in-situ measurements, especially for MSI bands above 705 nm (B6–B8), where the RMSE decreases from ~0.023 to lower than 0.006 in dark lakes and from ~0.015 to lower than 0.004 in bright lakes (Figure 5.10). Evidently, the LSU approach solves the unmixing problem of the water spectrum and reduces the discrepancy caused by forest adjacency. However, note that results have limitations to an extensive application, because we assume that only the forest surface causes adjacency effects and the water endmember was based on prior knowledge of radiometric collection over lakes. These assumptions limit the operational correction to reservoir and lakes with historical radiometric collection or to cases where water endmember can be derived from the image itself. Furthermore, adjacency effects typically depend on the surface types in the scene, which makes it reasonable to consider that unmixing problems are caused by other surfaces. Recently, Sterckx et al. (2015) proposed a generic-sensor adjacency correction based on the NIR similarity spectrum for water studies, and showed positive or neutral effects on the reflectance accuracy depending on environmental conditions. In general, adjacency correction is a complex procedure that should consider a variety of environmental conditions. Our positive experience using the LSU model is a preliminary assessment to advance towards a more sophisticated image-based approach.

Figure 5.10. Comparison between MSI TOA reflectance (grey), MSI-corrected reflectance from 6SV model (dark blue), and MSI-adjacency corrected reflectance (purple) and MSI reflectance simulated from in-situ measurements (light blue) from dark (a,c) and bright lakes (b,d). RMSE bars before (6SV) and after adjacency correction (6SV + adj. cor) applied to MSI image from 12 August 2016.

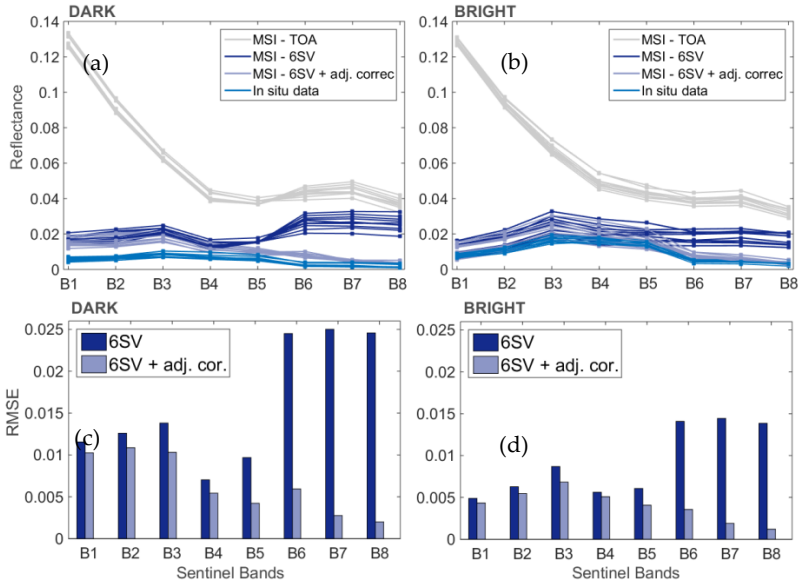

5.5. Conclusions

Sentinel 2 MSI images represent a new opportunity for monitoring small inland aquatic systems. However, to derive an accurate surface reflectance over complex water and consequently produce better water quality products, efforts must focus on the development of efficient atmospheric correction methods. Although our results present a variation in the surface reflectance accuracy along the spectral range, it is important to highlight the complexity of environmental condition in our study area, such as the water reflectance (<2%), narrow and irregular lakes, low spatial variability and strong influence of the adjacency forest.

In terms of the temporal variation of atmospheric constituents (cloud cover, AOD and U_{H_2O}) within the study area, high cloud cover (~90%) limits the cloud-free image during the first half of the year. The cloud cover decreases in the second half of the year (60%–80%), while AOD increases from ~0.12 to ~0.18 and water vapour remains constant ~4.4 g/cm^2 between seasons. The fine resolution of MAIAC AOD product has an acceptable accuracy to support radiative transfer models in the Amazon region. The

simulation of the TOA reflectance clearly shows an inherent difficulty faced by inland water studies, because the atmospheric contribution varies from ~50% to ~94% of TOA signal according to spectral band.

The atmospheric correction methods present a notable variation in the MSI-corrected accuracy along spectral bands depending on lake characteristics. For dark lakes, the results indicate method limitations to derive an accurate reflectance spectrum, particularly above 705 nm due to forest adjacency effects. In the visible bands, Sen2Cor and ACOLITE showed quite similar RMSEs for dark lakes whereas the 6SV model exhibited better results for bright lakes. Therefore, the selection of an atmospheric correction method needs to be aligned with the study purposes and user expertise to apply these tools, since our results present advantages and disadvantages of different methods for the reflectance shape and magnitude accuracy.

All methods showed limitations in the accurate retrievals in the NIR region due to forest adjacency effects. The performance of the adjacency correction using the LSU model improved the quality of MSI-corrected reflectance and derived better spectra shape compared with the in-situ measurements. However, there are constraints for operational application, such as selection of the water endmember and other adjacent surfaces, which need to be taken into account when applying the method to different contexts/regions. Therefore, this experience is considered to be a preliminary assessment to advance on image-based approaches to remove adjacency effects.

The assessment of these atmospheric correction methods has an inherent challenge due to the shortage of cloud-free images and the limitations of routine in-situ measurements. However, even for a single Sentinel-2 image, it was possible to explore the available methods applied to complex environmental conditions (low water reflectance, forest adjacency effects and seasonal variability of aerosol atmospheric), such as in the Amazon region. We recommend an extensive validation for distinct water types and atmospheric conditions to further understand the potential and limitations of these atmospheric correction methods.

6 FINAL CONSIDERATIONS

An assessment of atmospheric constituents is an important analysis to enhance our comprehension of atmospheric attenuation and its effects on satellite remote sensing data. In this dissertation, we have provided the detailed information about the (i) quality of MAIAC AOD retrievals across South America, (ii) main features of atmospheric constituents in Amazon basin, and (iii) evaluation of atmospheric correction over Amazon floodplain lakes. The research questions (*italic*) listed in section 1.2 are addressed below.

Chapter 3 - How adequate are MAIAC AOD retrievals in comparison to ground-truth AERONET measurements across South America? Is the quality feasible for aerosol monitoring?

Our findings in Chapter 3 show that MAIAC and AERONET AOD comparisons stratified by land cover type present distinct retrieval performance, with relative better results over vegetated and cropland areas than those over bright surfaces, such as urban and barren areas. Although performance varies according surface types, the overall correlation coefficient between MAIAC and AERONET data is close to unity for both Terra and Aqua products (R: 0.956 and 0.949, respectively). Critical condition is observed over relative bright surface and low AOD events (<0.2), which might reduce substantially the proportion of aerosol contribution in TOA signal and increase the complexity to decouple surface and aerosol signals. In central-west of South America, high biomass burning emissions increase the AOD magnitude during austral spring, with most part of fires occurring over pasture and cropland areas. Therefore, the results of MAIAC AOD retrievals over cropland and savanna during second half of year guarantee the quality of MAIAC data to further aerosol studies during critical AOD records across South America. Using the lower expected error compared to heritage MOD04 product, we note that MAIAC retrievals exceed the number of retrievals falling within 66% threshould (~1 sigma) in most surface types. These findings suggested that MAIAC AOD retrievals promise to overcome previous empirical limitations based on time-series approach using new threshold for expected error. Therefore, AOD retrievals

are feasible for aerosol monitoring at 1 km resolution in most surface of South America and additional care is needed over bright surfaces and extreme low AOD events.

Chapter 4 - What is the main feature of cloud cover and atmospheric constituents in the Amazon basin? What are their implications for the remote sensing monitoring of Amazon ecosystem?

In the chapter 4, we show the main seasonal features of cloud cover and atmospheric constituents in the Amazon region. Our findings show that persistence cloudy regime implies in significant obstacles for remote sensing over Northern region, while short period (3 to 5 month) of cloudless is observed in Southern Amazon. In the dry season, the opportunity for cloud-free image is followed by increase of aerosol and ozone content in most part of Amazon. The seasonal pattern of fires in southern region affects the atmospheric turbidity between August and October, what might increase the error in surface reflectance retrievals. In turn, water vapor content presents relative low seasonality, with high concentration throughout the year and slight decrease during dry season (June-July-August). The sensitivity analysis shows that water vapor and ozone transmittance actually have a slight variability between simulated concentration ranges. Indeed, aerosol and molecular scattering become most responsible to increase TOA reflectance, where scattering reflectance reaches more than 0.12 in the blue and deep blue bands. Remote sensing community could benefit of detailed seasonal analysis of atmospheric constituents in Amazon region: field campaign and remote sensing application might be planned to acquire images during clean atmospheric and low cloud cover regimes, such as June and July.

Chapter 5 - Are the atmospheric correction methods feasible to estimate the surface water reflectance in Amazon floodplain lakes? What are the challenges for atmospheric correction in region?

High-level quality of the MSI sensor presents potential in small lake remote sensing. However, strong impact of both atmospheric and adjacency effects is clearly observed in MSI TOA reflectance of Amazon floodplain lakes. None of atmospheric correction models presented an outstanding performance, although all algorithms are feasible to

remove most part of atmospheric contribution. Further, the relative better surface retrievals are observed in the visible bands, which is suggestive for biophysical model applications using spectral bands in this region. In our study, the major challenges are related to (i) high adjacency effects caused by forest neighbourhood and (ii) low water reflectance in dark lakes (up to 1%). The first challenge (i) impacts the near-infrared bands due to high contrast of spectral reflectance of water and vegetation in NIR region. In second (ii), low water reflectance reduces the proportional contribution of water surface in TOA measurements and comparisons between satellite and ground-data presented biases higher than 100% for 6SV method. Additionally, the simulation of TOA signal shows that atmospheric effects contribute to more than 50 % for all spectral bands, and consequently, emphasizes how complex is the accurate surface retrievals in water studies. The validation of these models is suggested to ensure the consistence of these methods in routine surface reflectance retrievals. In fact, the choice of method will most depend of user expertise and additional source data for input parameter in atmospheric correction, such as 6SV. Finally, while the high-resolution sensors provide a new scientific opportunity to observe small lakes, rivers and reservoirs, data processing has inherent challenges due to contribution of sun- and sky-glint at sub-pixel, signal-noise ratio, and adjacency effects (Ruddick et al., 2016).

7. REFERENCES

ABELL, R.; THIEME, M.L.; REVENGA, C.; BRYER, M.; KOTTELAT, M.; BOGUTSKAYA, N.; COAD, B.; MANDRAK, N.; BALDERAS, S. C.; BUSSING, W.; STIASSNY, M.L.J.; SKELTON, P.; ALLEN, G.R.; UNMACK, P.; NASEKA, A.; NG, R.; SINDORF, N.; ROBERTSON, J.; ARMIJO, E.; HIGGINS, J.V.; HEIBEL, T.J.; WIKRAMANAYAKE, E.; OLSON, D.; LÓPEZ, H.L.; REIS, R.E.; LUNDBERG, J.G.; PÉREZ, M.H.S.; PETR,Y P. Freshwater ecoregions of the world : a new map of biogeographic units for freshwater biodiversity conservation. **Bioscience**, v. 58, n. 5, p. 403, 2008.

AFFONSO, A. G.; QUEIROZ, H. L. DE; NOVO, E. M. L. D. M. Limnological characterization of floodplain lakes in Mamirauá Sustainable Development Reserve, central Amazon (Amazonas state, Brazil). **Acta Limnologica Brasiliensia**, v. 23, n. 1, p. 95–108, 2011.

AFFONSO, A. G.; QUEIROZ, H. L.; NOVO, E. M. L. M. Abiotic variability among different aquatic systems of the central Amazon floodplain during drought and flood events. **Brazilian Journal of Biology**, v. 75, n. 4, p. 60–69, 2015.

AINSWORTH, E.; YENDREK, C. R.; SITCH, S.; COLLINS, W. J.; EMBERSON, L. D. The effects of tropospheric ozone on net primary productivity and implications for climate change. **Annual Review of Plant Biology**, v. 63, p. 637–61, 2012.

AKAGI, S. K.; YOKELSON, R. J.; WIEDINMYER, C.; ALVARADO, M. J.; REID, J. S.; KARL, T.; CROUNSE, J. D.; WENNBERG, P. O. Emission factors for open and domestic biomass burning for use in atmospheric models. **Atmospheric Chemistry and Physics**, v. 11, n. 9, p. 4039–4072, 2011.

ANDERSON, T.; CHARLSON, R. Mesoscale variations of tropospheric aerosols. **Journal of the Atmospheric Sciences**, v. 60, p. 119–136, 2003.

ANDREAE, M. O.; MERLET, P. Emission of trace gases and aerosols from biomass burning. **Global Biogeochemical Cycles**, v. 15, n. 4, p. 955–966, 2001.

ANDREAE, M. O.; ROSENFELD, D. Aerosol–cloud–precipitation interactions. Part 1. The nature and sources of cloud-active aerosols. **Earth-Science Reviews**, v. 89, n. 1, p. 13-41, 2008.

ANDREAE, M. O. et al. The amazon tall tower observatory (atto): overview of pilot measurements on ecosystem ecology, meteorology, trace gases, and aerosols. **Atmospheric Chemistry and Physics**, v. 15, n. 18, p. 10723–10776, 2015.

ANDREWS, D. G. **An introduction to atmospheric physics**. Cambridge University Press, 2010.

Angal, A.; XIONG, X. J.; SUN, J.; GENG, X. On-orbit noise characterization of MODIS reflective solar bands. **Journal of Applied Remote Sensing**, v.9, n. 1, p. 094092-094092, 2015.

ÅNGSTRÖM, A. On the atmospheric transmission of sun radiation and on dust in the air. **Geografiska Annaler**, v. 11, p. 156-166, 1929.

ARAGÃO, L. E. O. C.; MALHI, Y.; BARBIER, N.; LIMA, A. A.; SHIMABUKURO, Y.; ANDERSON, L.; SAATCHI, S. Interactions between rainfall, deforestation and fires during recent years in the brazilian amazonia. **Philosophical Transactions of the Royal Society of London: Biological Sciences**, v. 363, n. 1498, p. 1779–85, 2008.

ARAGÃO, L. E. O. C.; SHIMABUKURO, Y. E. The incidence of fire in Amazonian forests with implications for REDD. **Science**, v. 328, n. 5983, p. 1275–1278, 2010.

ARAGAO, L. E. O. C.; MALHI, Y.; ROMAN-CUESTA, R.M.; SAATCHI, S.; ANDERSON, L.O.; SHIMABUKURO, Y.E. Spatial patterns and fire response of recent Amazonian droughts. **Geophysical Research Letters**, v. 34, n. 7, 2007.

ARAGÃO, L. E. O. C.; POULTER, B.; BARLOW, J. B.; ANDERSON, L. O.; MALHI, Y.; SAATCHI, S.; PHILLIPS, O. L.; GLOOR, E. Environmental change and the carbon balance of Amazonian forests. **Biological reviews**, v. 89, n. 4, p. 913–931, 2014.

ARTAXO, P.; HANSSON, H. C. Size distribution of biogenic aerosol particles from the Amazon basin. **Atmospheric Environment**, v. 29, n. 3, p. 393–402, 1995.

ARTAXO, P.; RIZZO, L. V; BRITO, J. F.; BARBOSA, H. M. J.; ARANA, A.; SENA, E. T.; CIRINO, G. G.; BASTOS, W.; MARTIN, S. T.; ANDREAE, M. O. Atmospheric aerosols in Amazonia and land use change: from natural biogenic to biomass burning conditions. **Faraday Discussions**, v. 165, p. 203, 2013.

ASNER, G. P. Cloud cover in Landsat observations of the Brazilian Amazon. **International Journal of Remote Sensing**, v. 22, n. 18, p. 3855–3862, 2001.

BAARS, H.; ANSMANN, A.; ALTHAUSEN, D.; ENGELMANN, R.; ARTAXO, P.; PAULIQUEVIS, T.; SOUZA, R. Further evidence for significant smoke transport from Africa to Amazonia. **Geophysical Research Letters**, v. 38, n. 20, 2011.

BACCINI, A.; GOETZ, S. J.; WALKER, W. S.; LAPORTE, N. T.; SUN, M.; SULLA-MENASHE, D.; HACKLER, J.; BECK, P. S. A.; DUBAYAH, R.; FRIEDL, M. A.; SAMANTA, S.; HOUGHTON, R. A. Estimated carbon dioxide emissions from tropical deforestation improved by carbon-density maps. **Nature Climate Change**, v. 2, n. 3, p. 182–185, 2012.

BAILLARIN, S. J.; MEYGRET, A.; DECHOZ, C.; PETRUCCI, B.; LACHERADE, S.; TREMAS, T.; ISOLA, C.; MARTIMORT, P.; SPOTO, F. Sentinel-2 level 1 products and image processing performances. In: IEEE INTERNATIONAL GEOSCIENCE AND REMOTE SENSING SYMPOSIUM, 2012, Munich, Germany. **Proceedings…** IEEE, 2012. p. 7003–7006.

BARBOSA, C. C. A.; ATKINSON, P. M.; DEARING, J. A. Remote sensing of ecosystem services: a systematic review. **Ecological Indicators**, v. 52, p. 430–443, 2015.

BARLOW, J.; PERES, C. A. Fire-mediated dieback and compositional cascade in an Amazonian forest. **Philosophical Transactions of the Royal Society of London: Biological**

Sciences, v. 363, n. 1498, p. 1787–1794, 2008.

BARNES, B. B.; HU, C.; KOVACH, C.; SILVERSTEIN, R. N. Sediment plumes induced by the port of Miami dredging: analysis and interpretation using Landsat and MODIS data. **Remote sensing of Environment**, v. 170, p. 328–339, 2015.

BARSI, J. A.; MARKHAM, B. L.; PEDELTY, J. A. The operational land imager: spectral response and spectral uniformity. In: **SPIE Optical Engineering + Applications**. International Society for Optics and Photonics, p. 81530G-81530G-11, 2011.

BASART, S.; PÉREZ, C.; CUEVAS, E.; BALDASANO, J. M.; GOBBI, G. P. Aerosol characterization in northern Africa, northeastern Atlantic, Mediterranean basin and middle east from direct-sun aeronet observations. **Atmospheric Chemistry and Physics**, v. 9, n. 21, p. 8265–8282, 2009.

BASSANI, C.; MANZO, C.; BRAGA, F.; BRESCIANI, M.; GIARDINO, C.; ALBEROTANZA, L. The impact of the microphysical properties of aerosol on the atmospheric correction of hyperspectral data in coastal waters. **Atmospheric Measurement Techniques**, v. 8, n. 3, p. 1593–1604, 2015.

BELL, M. L.; DAVIS, D. L.; GOUVEIA, N.; BORJA-ABURTO, V. H.; CIFUENTES, L. A. The avoidable health effects of air pollution in three Latin American cities: Santiago, São Paulo, and Mexico City. **Environmental Research**, v. 100, n. 3, p. 431–440, 2006.

BENAS, N.; CHRYSOULAKIS, N.; GIANNAKOPOULOU, G. Validation of MERIS/AATSR synergy algorithm for aerosol retrieval against globally distributed aeronet observations and comparison with MODIS aerosol product. **Atmospheric Research**, v. 132–133, p. 102–113, 2013.

BERGER, M.; MORENO, J.; JOHANNESSEN, J. A.; LEVELT, P. F.; HANSSEN, R. F. ESA's sentinel missions in support of Earth system cience. **Remote Sensing of Environment**, v. 120, p. 84-90, 2012.

BERK,A.; ANDERSON, G. P.; ACHARYA, P. K.; BERNSTEIN, L. S.; MURATOV,L.; LEE,J.; FOX,M. J.; ADLER-GOLDEN, S. M.; CHETWYND, J. H.; HOKE, M. L.; LOCKWOOD, R. B.; GARDNER, J. A.; COOLEY, T. W.; LEWIS, P. E. MODTRAN 5: a reformulated atmospheric band model with auxiliary species and practical multiple scattering options: update. In: **Defense and security**. International Society for Optics and Photonics, , 2005. p. 662-667.

BIBI, H.; ALAM, K.; CHISHTIE, F.; BIBI, S.; SHAHID, I.; BLASCHKE, T. Intercomparison of MODIS, MISR, OMI, and CALIPSO aerosol optical depth retrievals four locations on the Indo-Gangetic plains and validation against AERONET data. **Atmospheric Environment**, v. 111, p. 113-126, 2015.

BODHAINE, B. A.; WOOD, N. B.; DUTTON, E. G.; SLUSSER, J. R. On Rayleigh optical depth calculations. **Journal of Atmospheric and Oceanic Technology**, v. 16, n. 11, p. 1854–1861, 1999.

BOERS, N.; MARWAN, N.; BARBOSA, H. M. J.; KURTHS, J. A deforestation-induced

tipping point for the South American Monsoon system. **Scientific Reports**, v. 7, 2017.

BORBAS, E. E.; SEEMANN, S.W.; KERN, A.; MOY, L.; LI, J. **MODIS atmospheric profile retrieval algorithm theoretical basis document**: collection 6. NASA ATBD, 2011.

BORDI, I.; DE BONIS, R.; FRAEDRICH, K.; SUTERA, A. Interannual variability patterns of the world's total column water content: Amazon River basin. **Theoretical and applied climatology**, v. 122, n. 3–4, p. 441–455, 2014.

BROXTON, P. D.; ZENG, X.; SULLA-MENASHE, D.; TROCH, P. A. A global land cover climatology using MODIS data. **Journal of Applied Meteorology and Climatology**, v. 53, n. 6, p. 1593–1605, 2014.

BURAZEROVIC, D.; GEENS, B.; HEYLEN, R.; STERCKX, S.; SCHEUNDERS, P. Unmixing for detection and quantification of adjacency effects. In: IEEE INTERNATIONAL GEOSCIENCE AND REMOTE SENSING SYMPOSIUM, 2012, Munich, Germany. **Proceedings…** IEEE, 2012. p. 3090–3093.

CARSLAW, K. S.; LEE, L. A; REDDINGTON, C. L.; PRINGLE, K. J.; RAP, A.; FORSTER, P. M.; MANN, G. W.; SPRACKLEN, D. V; WOODHOUSE, M. T.; REGAYRE, L. A; PIERCE, J. R. Large contribution of natural aerosols to uncertainty in indirect forcing. **Nature**, v. 503, n. 7474, p. 67–71, 2013.

CARVALHO, L. M. V; JONES, C.; LIEBMANN, B. The South Atlantic Convergence Zone: intensity, form, persistence, and relationships with intraseasonal to interannual activity and extreme rainfall. **Journal of Climate**, v. 17, n. 1, p. 88–108, 2004.

CASTANHO, A. D.; MARTINS, J. V.; ARTAXO, P.. MODIS aerosol optical depth retrievals with high spatial resolution over an urban area using the critical reflectance. **Journal of Geophysical Research**, v. 113, p. D02201, 2008.

CASTELLO, L.; VIANA, J. P.; WATKINS, G.; PINEDO-VASQUEZ, M.; LUZADIS, V. A. Lessons from integrating fishers of arapaima in small-scale fisheries management at the mamirauá reserve, amazon. **Environmental Management**, v. 43, n. 2, p. 197–209, 2009.

CHAMBERS, J. Q.; ASNER, G. P.; MORTON, D. C.; ANDERSON, L. O.; SAATCHI, S. S.; ESPÍRITO-SANTO, F. D. B.; PALACE, M.; SOUZA, C. Regional ecosystem structure and function: ecological insights from remote sensing of tropical forests. **Trends in Ecology and Evolution**, v. 22, n. 8, p. 414–423, 2007.

CHANDER, G.; MARKHAM, B. L.; HELDER, D. L. Summary of current radiometric calibration coefficients for LANDSAT MSS, TM, ETM+, and EO-1 ALI sensors. **Remote Sensing of Environment**, v. 113, n. 5, p. 893–903, 2009.

CHAVEZ, P. S. An improved dark-object subtraction technique for atmospheric scattering correction of multispectral data. **Remote Sensing of Environment**, v. 24, n. 3, p. 459–479, 1988.

CHEN, Y.; MORTON, D. C.; JIN, Y.; COLLATZ, G. J.; KASIBHATLA, P. S.; VAN DER WERF, G. R.; DEFRIES, R. S.; RANDERSON, J. T. Long-term trends and interannual

variability of forest, savanna and agricultural fires in South America. **Carbon Management**, v. 4, n. 6, p. 617–638, 2013.

CHERVET, P.; LAVIGNE, C.; ROBLIN, A.; BRUSCAGLIONI, P. Effects of aerosol scattering phase function formulation on point-spread-function calculations. **Applied Optics**, v. 41, n. 30, p. 6489–6498, 2002.

CHU, D. A. Validation of MODIS aerosol optical depth retrieval over land. **Geophysical Research Letters**, v. 29, n. 12, p. 8007, 2002.

CHUDNOVSKY, A.; TANG, C.; LYAPUSTIN, A.; WANG, Y.; SCHWARTZ, J.; KOUTRAKIS, P. A critical assessment of high-resolution aerosol optical depth retrievals for fine particulate matter predictions. **Atmospheric Chemistry and Physics**, v. 13, n. 21, p. 10907–10917, 2013.

CLEVERS, J. G. P. W.; GITELSON, A. A. Remote estimation of crop and grass chlorophyll and nitrogen content using red-edge bands on Sentinel-2 and -3. **International Journal of Applied Earth Observation and Geoinformation**, v. 23, n. 1, p. 344–351, 2013.

COSTA, M. H.; BIAJOLI, M. C.; SANCHES, L.; MALHADO, A. C. M.; HUTYRA, L. R.; DA ROCHA, H. R.; AGUIAR, R. G.; DE ARAÚJO, A. C. Atmospheric versus vegetation controls of amazonian tropical rain forest evapotranspiration: are the wet and seasonally dry rain forests any different? **Journal of Geophysical Research: Biogeosciences**, v. 115, n. 4, p. 1–9, 2010.

CZAPLA-MYERS, J.; MCCORKEL, J.; ANDERSON, N.; THOME, K.; BIGGAR, S.; HELDER, D.; AARON, D.; LEIGH, L.; MISHRA, N. The ground-based absolute radiometric calibration of Landsat 8 OLI. **Remote Sensing**, v. 7, n. 1, p. 600-626, 2015.

D'ALMEIDA, G. A.; KOEPKE, P.; SHETTLE, E. P. **Atmospheric aerosols:** global climatology and radiative characteristics. A Deepak Pub, 1991.

DAVIDSON, E. A.; DE ARAÚJO, A. C.; ARTAXO, P.; BALCH, J. K.; BROWN, I. F.; C. BUSTAMANTE, M. M.; COE, M. T.; DEFRIES, R. S.; KELLER, M.; LONGO, M.; MUNGER, J. W.; SCHROEDER, W.; SOARES-FILHO, B. S.; SOUZA, C. M.; WOFSY, S. C. The amazon basin in transition. **Nature**, v. 481, n. 7381, p. 321–328, 2012.

DOR, B. B.; DEVIR, A. D.; SHAVIV, G.; BRUSCAGLIONI, P.; DONELLI, P., ISMAELLI, A. Atmospheric scattering effect on spatial resolution of imaging systems. **Optical Society of America**, v. 14, n. 6, p. 1329–1337, 1997.

DÖRNHÖFER, K.; GÖRITZ, A.; GEGE, P.; PFLUG, B.; OPPELT, N. Water constituents and water depth retrieval from Sentinel-2A—a first evaluation in an oligotrophic lake. **Remote Sensing**, v. 8, n. 11, p. 941, 2016.

DRUSCH, M.; DEL BELLO, U.; CARLIER, S.; COLIN, O.; FERNANDEZ, V.; GASCON, F.; HOERSCH, B.; ISOLA, C.; LABERINTI, P.; MARTIMORT, P.; MEYGRET, A.; SPOTO, F.; SY, O.; MARCHESE, F.; BARGELLINI, P. Sentinel-2: ESA's optical high-resolution mission for GMES operational services. **Remote Sensing of Environment**, v. 120, p. 25–36, 2012.

DUAN, S.-B.; LI, Z.-L.; TANG, B.-H.; WU, H.; TANG, R.; BI, Y. Atmospheric correction of

high-spatial-resolution satellite images with adjacency effects: application to EO-1 ALI data. **International Journal of Remote Sensing**, v. 36, n. 19–20, p. 5061–5074, 2015.

DUDGEON, D.; ARTHINGTON, A. H.; GESSNER, M. O.; KAWABATA, Z.-I.; KNOWLER, D. J.; LÉVÊQUE, C.; NAIMAN, R. J.; PRIEUR-RICHARD, A.-H.; SOTO, D.; STIASSNY, M. L. J.; SULLIVAN, C. A. Freshwater biodiversity: importance, threats, status and conservation challenges. **Biological Reviews**, v. 81, n. 2, p. 163, 2006.

ECK, T. F.; HOLBEN, B. N.; REID, J. S.; DUBOVIK, O.; SMIRNOV, A.; O'NEILL, N. T.; SLUTSKER, I.; KINNE, S. Wavelength dependence of the optical depth of biomass burning, urban, and desert dust aerosols. **Journal of Geophysical Research**, v. 104, n. 1, p. 31333, 1999.

ECK, T. F.; HOLBEN, B. N.; SINYUK, A.; PINKER, R. T.; GOLOUB, P.; CHEN, H.; CHATENET, B.; LI, Z.; SINGH, R. P.; TRIPATHI, S. N.; REID, J. S.; GILES, D. M.; DUBOVIK, O.; O'NEILL, N. T.; SMIRNOV, A.; WANG, P.; XIA, X. Climatological aspects of the optical properties of fine/coarse mode aerosol mixtures. **Journal of Geophysical Research Atmospheres**, v. 115, n. 19, 2010.

ELTAHIR, E. A. B.; BRAS, R. L. Precipitation recycling in the Amazon basin. **Quarterly Journal of the Royal Meteorological Society**, v. 120, n. 518, p. 861–880, 1994.

EMCK, P. **A climatology of South Ecuador-with special focus on the major Andean ridge as Atlantic-Pacific climate divide**. 2007. Doctoral Thesis - Friedrich-Alexander-Universität Erlangen-Nürnberg (FAU), 2007.

ENT, R. J. V.D.; SAVENIJE, H. H.; SCHAEFLI, B; STEELE-DUNNE, S. C. Origin and fate of atmospheric moisture over continents. **Water Resources Research**, v. 46, n. 9, 2010.

ESPINOZA VILLAR, R.; MARTINEZ, J. M.; GUYOT, J. L.; FRAIZY, P.; ARMIJOS, E.; CRAVE, A.; BAZÁN, H.; VAUCHEL, P.; LAVADO, W. The integration of field measurements and satellite observations to determine river solid loads in poorly monitored basins. **Journal of Hydrology**, v. 444–445, p. 221–228, 2012.

FENG, M.; SEXTON, J. O.; HUANG, C.; MASEK, J. G.; VERMOTE, E. F.; GAO, F.; NARASIMHAN, R.; CHANNAN, S.; WOLFE, R. E.; TOWNSHEND, J. R. Global surface reflectance products from Landsat: assessment using coincident MODIS observations. **Remote Sensing of Environment**, v. 134, p. 276–293, 2013.

FRANZ, B. A.; BAILEY, S. W.; KURING, N.; WERDELL, P. J. **Ocean color measurements from Landsat-8 OLI using SEADAS**. NASA report, 2014.

FRASER, R. S.; KAUFMAN, Y. J. The relative importance of aerosol scattering and absorption in remote sensing. **IEEE Transactions on Geoscience and Remote Sensing**, v. 23, n. 5, p. 625-633, 1985.

FU, R.; DICKINSON, R.; CHEN, M.; WANG, H. How do tropical sea surface temperatures influence the seasonal distribution of precipitation in the equatorial Amazon? **Journal of Climate**, v. 14, n. 20, p. 4003-4026, 2001.

FU, R.; LI, W. The influence of the land surface on the transition from dry to wet season in

Amazonia. **Theoretical and applied climatology**, v. 78, n. 1–3, p. 97–110, 2004.

GALVÃO, L. S.; ROBERTS, D. A.; FORMAGGIO, A. R.; NUMATA, I.; BREUNIG, F. M.. View angle effects on the discrimination of soybean varieties and on the relationships between vegetation indices and yield using off-nadir Hyperion data. **Remote Sensing of Environment**, v. 113, n. 4, p. 846-856, 2009.

GALVÃO, L. S.; BREUNIG, F. M.; DOS SANTOS, J. R.; DE MOURA, Y. M. View-illumination effects on hyperspectral vegetation indices in the Amazonian Tropical Forest. **International Journal of Applied Earth Observation and Geoinformation**, v. 21, n. 1, p. 291–300, 2012.

GAO, B. C.; KAUFMAN, Y. J. Water vapor retrievals using moderate resolution imaging spectroradiometer (MODIS) near-infrared channels. **Journal of Geophysical Research: Atmospheres**, v. 108, n. 13, 2003.

GAO, B. C.; MONTES, M. J.; DAVIS, C. O.; GOETZ, A. F. H. Atmospheric correction algorithms for hyperspectral remote sensing data of land and ocean. **Remote Sensing of Environment**, v. 113, p. 17-24, 2009.

GARABA, S. P.; ZIELINSKI, O. An assessment of water quality monitoring tools in an estuarine system. **Remote Sensing Applications: Society and Environment**, v. 2, p. 1–10, 2015.

GARREAUD, R. D. The Andes climate and weather. **Advances in Geosciences**, v. 22, p. 3–11, 2009.

GASCON, F.; CADAU, E.; COLIN, O.; HOERSCH, B.; ISOLA, C.; LÓPEZ FERNÁNDEZ, B.; MARTIMORT, P. Copernicus Sentinel-2 mission: products, algorithms and cal/val. In: **SPIE Optical Engineering+ Applications**. International Society for Optics and Photonics, p. 92181E-92181E-9, 2014.

GILLINGHAM, S. S. et al. Limitations of the dense dark vegetation method for aerosol retrieval under Australian conditions. **Remote Sensing Letters**, v. 3, n. 1, p. 67-76, 2012.

GINOUX, P.; PROSPERO, J. M.; GILL, T. E.; HSU, N. C.; ZHAO, M. Global-scale attribution of anthropogenic and natural dust sources and their emission rates based on modis deep blue aerosol products. **Reviews of Geophysics**, v. 50, n. 3, p. 1–36, 2012.

GOMIS-CEBOLLA, J.; JIMÉNEZ-MUÑOZ, J.; SOBRINO, J. Modis-based monthly LST products over Amazonia under different cloud mask schemes. **Data**, v. 1, n. 2, p. 2, 2016.

GRAU, E.; GASTELLU-ETCHEGORRY, J. P. Radiative transfer modeling in the Earth–Atmosphere system with DART model. **Remote Sensing of Environment**, v. 139, p. 149-170, 2013.

GRIMM, A. M.; TEDESCHI, R. G. ENSO and extreme rainfall events in South America. **Journal of Climate**, v. 22, n. 7, p. 1589–1609, 2009.

GRIMM, A. M. Interannual climate variability in South America: impacts on seasonal

precipitation, extreme events, and possible effects of climate change. **Stochastic environmental research and risk assessment**, v. 25, n. 4, p. 537–554, 2011.

GRODSKY, S. A.; CARTON, J. A. The Intertropical Convergence Zone in the South Atlantic and the Equatorial cold tongue. **Journal of Climate**, v. 16, n. 4, p. 723–733, 2003.

HADJIMITSIS, D. G.; CLAYTON, C. R. I.; HOPE, V. S. An assessment of the effectiveness of atmospheric correction algorithms through the remote sensing of some reservoirs. **International Journal of Remote Sensing**, v. 25, n. 18, p. 3651–3674, 2004.

HANSEN, J. E.; TRAVIS, L. D.. Light scattering in planetary atmospheres. **Space Science Reviews**, v. 16, n. 4, p. 527-610, 1974.

HANSEN, M. C.; POTAPOV, P. V.; MOORE, R.; HANCHER, M.; TURUBANOVA, S. A.; TYUKAVINA, A.; THAU, D.; STEHMAN, S. V.; GOETZ, S. J.; LOVELAND, T. R.; KOMMAREDDY, A.; EGOROV, A.; CHINI, L.; JUSTICE, C. O.; TOWNSHEND, J. R. G. High-resolution Global maps of 21st-century forest cover change. **Science**, v. 342, n. 6160, p. 850–853, 2013.

HARPER, A.; BAKER, I. T.; DENNING, A. S.; RANDALL, D. A.; DAZLICH, D.; BRANSON, M. Impact of evapotranspiration on dry season climate in the Amazon forest. **Journal of climate**, v. 27, n. 2, p. 574–591, 2014.

HEDLEY, J.; ROELFSEMA, C.; KOETZ, B.; PHINN, S. Capability of the Sentinel 2 mission for tropical coral reef mapping and coral bleaching detection. **Remote sensing of Environment**, v. 120, p. 145–155, 2012.

HELDER, D.; THOME, K. J.; MISHRA, N.; CHANDER, G.; XIONG, X.; ANGAL, A.; CHOI, T.. Absolute radiometric calibration of Landsat using a pseudo invariant calibration site. **IEEE Transactions on Geoscience and Remote Sensing**, v. 51, n. 3, p. 1360-1369, 2013.

HENDERSON, P. A.; HAMILTON, W. D.; CRAMPTON, W. G. R. Evolution and diversity in Amazonian floodplain communities. In: DYNAMICS OF TROPICAL COMMUNITIES: 37TH SYMPOSIUM OF THE BRITISH ECOLOGICAL SOCIETY, 37., 1998, London. **Proceedings…** Cambridge University Press, p. 385. 1998.

HILKER, T.; LYAPUSTIN, A. I.; TUCKER, C. J.; SELLERS, P. J.; HALL, F. G.; WANG, Y. Remote sensing of tropical ecosystems: atmospheric correction and cloud masking matter. **Remote Sensing of Environment**, v. 127, p. 370–384, 2012.

HILKER, T.; LYAPUSTIN, A. I.; HALL, F. G.; MYNENI, R.; KNYAZIKHIN, Y.; WANG, Y.; TUCKER, C. J.; SELLERS, P. J. On the measurability of change in Amazon vegetation from MODIS. **Remote Sensing of Environment**, v. 166, p. 233–242, 2015.

HOELZEMANN, J. J.; LONGO, K. M.; FONSECA, R. M.; DO ROSÁRIO, N. M. E.; EIBERN, H.; FREITAS, S. R.; PIRES, C. Regional representative of aeronet observation sites during the biomass burning season in South America determined by correlation studies with MODIS aerosol optical depth. **Journal of Geophysical Research Atmospheres**, v. 114, n. 13, p. 1–20, 2009.

HOLBEN, B. N.; ECK, T. F.; SLUTSKER, I.; TANRÉ, D.; BUIS, J. P.; SETZER, A.; VERMOTE, E.; REAGAN, J. A.; KAUFMAN, Y. J.; NAKAJIMA, T.; LAVENU, F.; JANKOWIAK, I.; SMIRNOV, A. AERONET—a federated instrument network and data archive for aerosol characterization. **Remote Sensing of Environment**, v. 66, n. 1, p. 1-16, 1998.

HOLBEN, B. N.; TANRE, D.; SMIRNOV, A.; ECK, T. F.; SLUTSKER, I.; ABUHASSAN, N.; KAUFMAN, Y. J.; NEWCOMB,W. W.;SCHAFER,J. S.; CHATENET,B.; LAVENU,F.; KAUFMAN,Y. J.;VANDE CASTLE,J. ;SETZER,A.; MARKHAM,B.; CLARK,D.; FROUIN,R.; HALTHORE,R.; KARNELI,A.; O'NEILL,N. T.; PIETRAS,C.; PINKER,R. T.; VOSS,K.; ZIBORDI, G. An emerging ground-based aerosol climatology: aerosol optical depth from aeronet. **Journal of Geophysical Research: Atmospheres**, v. 106, n. 11, p. 12067–12097, 2001.

HSU, N. C.; TSAY, S.-C.; KING, M. D.; HERMAN, J. R. Aerosol properties over bright-reflecting source regions. **IEEE Transactions on Geoscience and Remote Sensing**, v. 42, n. 3, p. 557–569, 2004.

HUANG, C.; TOWNSHEND, J. R. G.; LIANG, S.; KALLURI, S. N. V; DEFRIES, R. S. Impact of sensor's point spread function on land cover characterization : assessment and deconvolution. **Remote Sensing of Environment**, v. 80, n. 2, p. 203–212, 2002.

HUBANKS, P.; PLATNICK, S.; KING, M. **MODIS atmosphere L3 gridded product algorithm theoretical basis document (ATBD) -** users guide. ATBD MOD-30, NASA, 2015.

HYER, E. J.; REID, J. S.; ZHANG, J. An over-land aerosol optical depth data set for data assimilation by filtering, correction, and aggregation of MODIS Collection 5 optical depth retrievals. **Atmospheric Measurement Techniques**, v. 4, n. 3, p. 379–408, 2011.

INSTITUTO BRASILEIRO DE GEOGRAFIA E ESTATÍSTICA (IBGE). **Mudanças na cobertura e uso da terra 2000 – 2010 – 2012 - 2014**. Rio de Janeiro. 29 p. Available in ftp://geoftp.ibge.gov.br/informacoes_ambientais/cobertura_e_uso_da_terra/mudancas/documentos/mudancas_de_cobertura_e_uso_da_terra_2000_2010_2012_2014.pdf. Acess in: May, 05, 2017.

ICHOKU, C.; CHU, D. A.; MATTOO, S.; KAUFMAN, Y. J.; REMER, L. A.; TANRE, D.; SLUTSKER, I.; HOLBEN, B. N. A spatio-temporal approach for global validation and analysis of MODIS aerosol products. **Geophysical Research Letters**, v. 29, n. 12, p. 1–4, 2002.

ICHOKU, C.; REMER, L. A.; ECK, T. F. Quantitative evaluation and intercomparison of morning and afternoon Moderate Resolution Imaging Spectroradiometer (MODIS) aerosol measurements from terra and aqua. **Journal of geophysical research d: atmospheres**, v. 110, n. 10, p. 1–23, 2005.

IOCCG. Atmospheric correction for remotely-sensed Ocean-colour products. **Reports and Monographs of the International Ocean-colour Coordinating Group**, n. 10, p. 78, 2010.

SOLOMON, S.et al. (eds). **IPCC Climate Change 2007**: the physical science basis. Contribution of Working Group I to the Fourth Assessment Report of the Intergovernmental Panel on Climate Change. Cambride: University Press, 2007.

STOCKER, T.F.; QIN, D.; PLATTNER, G.-K.; TIGNOR, M.; ALLEN, S.K.; BOSCHUNG, J.; NAUELS, A.; XIA, Y.; BEX, V.; MIDGLEY, P.M. (eds.). **Climate change 2013**: the physical science basis. Contribution of Working Group I to the Fifth Assessment Report of the Intergovernmental Panel on Climate Change. Cambridge University Press, Cambridge, United Kingdom and New York, NY, USA, 2013.1535 p, doi:10.1017/CBO9781107415324.

IQBAL, M. **An introduction to solar radiation**. Elsevier, 1983.

IRONS, J. R.; DWYER, J. L.; BARSI, J. A. The next Landsat satellite: the Landsat data continuity mission. **Remote Sensing of Environment**, v. 122, p. 11-21, 2012.

JACOB, D. J.; WOFSY, S. C. Photochemistry of biogenic emissions over the amazon forest. **Journal of Geophysical Research: Atmospheres**, v. 93, n. 2, p. 1477-1486, 1988.

JAFFE, D. A.; WIGDER, N. L. Ozone production from wildfires: a critical review. **Atmospheric environment**, v. 51, p. 1–10, 2012.

JARDINE, K.; JARDINE, A. Biogenic volatile organic compounds in Amazonian forest ecosystems. In: Nagy, L.; Forsberg, B.R.; Artaxo, P. (Eds.). **Interactions between biosphere, atmosphere and human land use in the Amazon Basin**. Springer Berlin Heidelberg, p. 19-33. 2016.

JENSEN, J. R. **Remote sensing of the environment**: an Earth resource perspective. Pearson Education India, 2009.

JIMÉNEZ-MUÑOZ, J. C.; SOBRINO, J. A.; MATTAR, C.; FRANCH, B. Atmospheric correction of optical imagery from modis and reanalysis atmospheric products. **Remote Sensing of Environment**, v. 114, n. 10, p. 2195-2210, 2010.

JIMÉNEZ-MUÑOZ, J. C.; MATTAR, C.; BARICHIVICH, J.; SANTAMARÍA-ARTIGAS, A.; TAKAHASHI, K.; MALHI, Y.; SOBRINO, J. A.; SCHRIER, G. VAN DER. Record-breaking warming and extreme drought in the Amazon rainforest during the course of El Niño 2015–2016. **Scientific Reports**, v. 6, 33130, 2016. doi:10.1038/srep33130.

JONQUIÈRES, I.; MARENCO, A.; MAALEJ, A.; ROHRER, F. Study of ozone formation and transatlantic transport from biomass burning emissions over West Africa during the airborne Tropospheric Ozone Campaigns TROPOZ I and TROPOZ II. **Journal of Geophysical Research: Atmospheres**, v. 103, n. 15, p. 19059-19073, 1998.

JU, J.; ROY, D. P.; VERMOTE, E.; MASEK, J.; KOVALSKYY, V. Continental-scale validation of MODIS-based and LEDAPS Landsat ETM+ atmospheric correction methods. **Remote Sensing of Environment**, v. 122, p. 175-184, 2012.

KAHN, R. A.; GAITLEY, B. J.; MARTONCHIK, J. V.; DINER, D. J.; CREAN, K. A.; HOLBEN, B. Multiangle Imaging Spectroradiometer (MISR) Global aerosol optical depth validation based on 2 years of coincident AErosol RObotic NETwork (AERONET) observations. **Journal of Geophysical Research: Atmospheres**, v. 110, n. 10, p. 1–16, 2005.

KARL, T.; GUENTHER, A.; YOKELSON, R. J.; GREENBERG, J.; POTOSNAK, M.; BLAKE, D. R.; ARTAXO, P. The tropical forest and fire emissions experiment: Emission, chemistry, and transport of biogenic volatile organic compounds in the lower atmosphere over Amazonia. **Journal of Geophysical Research: Atmospheres**, v. 112, n. 18, p. 1–17, 2007.

KASTEN, F. A new table and approximation formula for the relative optial air mass. **Archiv für Meteorologie, Geophysik und Bioklimatologie, Serie B**, v. 14, n. 2, p. 206-223, 1965.

KAUFMAN, Y. J. Atmospheric effect on spatial resolution of surface imagery. **Applied Optics**, v. 23, n. 22, p. 4164–4172, 1984.

KAUFMAN, Y. J.; WALD, A. E.; REMER, L. A.; BO-CAI GAO; RONG-RONG LI; FLYNN, L. The MODIS 2.1-μm channel-correlation with visible reflectance for use in remote sensing of aerosol. **IEEE Transactions on Geoscience and Remote Sensing**, v. 35, n. 5, p. 1286–1298, 1997a.

KAUFMAN, Y. J.; TANRÉ, D.; REMER, L. A.; VERMOTE, E. F.; CHU, A.; HOLBEN, B. N. Operational remote sensing of tropospheric aerosol over land from EOS Moderate Resolution Imaging Spectroradiometer. **Journal of Geophysical Research: Atmospheres**, v. 102, n. 14, p. 17051-17067, 1997b.

KAUFMAN, Y. J.; TANRÉ, D.; BOUCHER, O. A satellite view of aerosols in the Climate system. **Nature**, v. 419, n. 6903, p. 215–223, 2002.

KAUFMAN, Y. J.; KOREN, I.; REMER, L. A.; TANRÉ, D.; GINOUX, P.; FAN, S. Dust transport and deposition observed from the Terra-Moderate Resolution Imaging Spectroradiometer (MODIS) spacecraft over the Atlantic Ocean. **Journal of Geophysical Research: Atmospheres**, v. 110, n. 10, p. 1–16, 2005.

KESHAVA, N.; MUSTARD, J. F. Spectral unmixing. **IEEE Signal Processing Magazine**, v. 19, n. 1, p. 44–57, 2002.

KING, M. D.; MENZEL, W. P.; KAUFMAN, Y. J.; TANRE, D.; BO-CAI GAO; PLATNICK, S.; ACKERMAN, S. A.; REMER, L. A.; PINCUS, R.; HUBANKS, P. A. Cloud and aerosol properties, precipitable water, and profiles of temperature and water vapor from modis. **IEEE Transactions on Geoscience and Remote Sensing**, v. 41, n. 2, p. 442–458, 2003.

KISELEV, V.; BULGARELLI, B.; HEEGE, T. Sensor independent adjacency correction algorithm for coastal and inland water systems. **Remote sensing of environment**, v. 157, p. 85–95, 2015.

KLOIBER, S. M.; BREZONIK, P. L.; OLMANSON, L. G.; BAUER, M. E. A procedure for regional lake water clarity assessment using landsat multispectral data. **Remote Sensing of Environment**, v. 82, n. 1, p. 38–47, 2002.

KLOOG, I.; SOREK-HAMER, M.; LYAPUSTIN, A.; COULL, B.; WANG, Y.; JUST, A. C.; SCHWARTZ, J.; BRODAY, D. M. Estimating daily PM 2.5 and PM10 across the complex geo-climate region of Israel using MAIAC satellite-based aod data. **Atmospheric Environment**, v. 122, p. 409-416, 2015.

KONDRATYEV, K.; KOZODEROV, V.; SMOKTY, O. **Remote sensing of the Earth from Space:** atmospheric correction. 1992.

KOREN, I.; REMER, L. A.; KAUFMAN, Y. J.; RUDICH, Y.; MARTINS, J. V. On the twilight zone between clouds and aerosols. **Geophysical Research Letters**, v. 34, n. 8, p. 1–5, 2007.

KOTCHENOVA, S. Y.; VERMOTE, E. F.; MATARRESE, R.; KLEMM, JR., F. J. Validation of a vector version of the 6S radiative transfer code for atmospheric correction of satellite data part i: path radiance. **Applied Optics**, v. 45, n. 26, p. 6762, 2006.

KUTSER, T.; PIERSON, D. C.; KALLIO, K. Y.; REINART, A.; SOBEK, S. Mapping lake cdom by satellite remote sensing. **Remote Sensing of Environment**, v. 94, n. 4, p. 535–540. 2005.

LENOBLE, J.; REMER, L.; TANRÉ, D. **Aerosol remote sensing**. Springer Science & Business Media. 2013.

LEVY, R. C.; REMER, L. A.; DUBOVIK, O. Global aerosol optical properties and application to Moderate Resolution Imaging Spectroradiometer aerosol retrieval over land. **Journal of Geophysical Research: Atmospheres**, v. 112. 2007a.

LEVY, R. C.; REMER, L. A.; MATTOO, S.; VERMOTE, E. F.; KAUFMAN, Y. J. Second-generation operational algorithm: retrieval of aerosol properties over land from inversion of Moderate Resolution Imaging Spectroradiometer spectral reflectance. **Journal of Geophysical Research: Atmospheres**, v. 112, n. 13, p. 1–21, 2007b.

LEVY, R. C.; REMER, L. A.; KLEIDMAN, R. G.; MATTOO, S.; ICHOKU, C.; KAHN, R.; ECK, T. F. Global evaluation of the Collection 5 MODIS Dark-target aerosol products over land. **Atmospheric Chemistry and Physics**, v. 10, n. 21, p. 10399–10420, 2010.

LEVY, R. C.; MATTOO, S.; MUNCHAK, L. A.; REMER, L. A.; SAYER, A. M.; PATADIA, F.; HSU, N. C. The Collection 6 MODIS aerosol products over Land and Ocean. **Atmospheric Measurement Techniques**, v. 6, n. 11, p. 2989–3034, 2013.

LEVY, R. C.; MUNCHAK, L. A.; MATTOO, S.; PATADIA, F.; REMER, L. A.;HOLZ, R. E. Towards a long-term global aerosol optical depth record: applying a consistent aerosol retrieval algorithm to MODIS and VIIRS-observed reflectance. **Atmospheric Measurement Techniques**, v.8, n.10, 4083. 2015.

LI, Z.; ZHAO, X.; KAHN, R.; MISHCHENKO, M.; REMER, L.; LEE, K.-H.; WANG, M.; LASZLO, I.; NAKAJIMA, T.; MARING, H. Uncertainties in satellite remote sensing of aerosols and impact on monitoring its long-term trend: a review and perspective. **Annales Geophysicae**, v. 27, n. 7, p. 2755–2770, 2009.

LIANG, S.; FANG, H.; CHEN, M. Atmospheric correction of Landsat ETM+ land surface imagery. I. Methods. **IEEE Transactions on Geoscience and Remote Sensing**, v. 39, n. 11, p. 2490-2498, 2001.

LIOU, K-N. **An introduction to atmospheric radiation**. Academic press, 2002.

LOBO, F. L.; COSTA, M. P. F.; NOVO, E. M. L. M. Time-series analysis of Landsat-MSS/TM/OLI images over Amazonian waters impacted by gold mining activities. **Remote Sensing of Environment**, v. 157, p. 170–184, 2014.

LOUIS, J.; DEBAECKER, V.; PFLUG, B.; MAIN-KNORN, M. Sentinel-2 sen2cor: L2A processor for users. **Proceedings living planet symposium**, p. 1–8, 2016.

LYAPUSTIN, A. I.; WANG, Y.; FREY, R. An automatic cloud mask algorithm based on time series of modis measurements. **Journal of Geophysical Research: Atmospheres**, v. 113, n. 16, p. 1–15, 2008.

LYAPUSTIN, A.; WANG, Y.; LASZLO, I.; KAHN, R.; KORKIN, S.; REMER, L.; LEVY, R.; REID, J. S. Multiangle Implementation of Atmospheric Correction (MAIAC): 2. Aerosol algorithm. **Journal of Geophysical Research: Atmospheres**, v. 116, n. 3, p. 1–15. 2011.

LYAPUSTIN, A.; KORKIN, S.; WANG, Y.; QUAYLE, B.; LASZLO, I. Discrimination of biomass burning smoke and clouds in MAIAC algorithm. **Atmospheric Chemistry and Physics**, v. 12, n. 20, p. 9679–9686, 2012a.

LYAPUSTIN, A.; WANG, Y.; LASZLO, I.; HILKER, T.; HALL, F.; SELLERS, P.; TUCKER, J.; KORKIN, S. Multi-Angle Implementation of Atmospheric Correction for MODIS (MAIAC): 3. Atmospheric correction. **Remote Sensing of Environment**, v. 127, p. 385-393, 2012b.

LYAPUSTIN, A.;WANG, Y.; XIONG, X.; MEISTER, G.; PLATNICK, S.; LEVY, R.; HALL, F.; FRANZ, B.; KORKIN, S.; HILKER, T.; TUCKER, J.; HALL, F.; SELLERS, P.; WU, A.;ANGAL, A. Scientific impact of MODIS C5 calibration degradation and C6+ improvements. **Atmos. Meas. Tech.,** v.7, p. 4353-4365,- 2014.

MACCORD, P. F. L.; SILVANO, R. A. M.; RAMIRES, M. S.; CLAUZET, M.; BEGOSSI, A. Dynamics of artisanal fisheries in two brazilian Amazonian reserves: implications to co-management. **Hydrobiologia**, v. 583, n. 1, p. 365–376, 2007.

MAIN-KNORN, M.; PFLUG, B.; DEBAECKER, V.; LOUIS, J. Calibration and Validation Plan for the L2A Processor and Products of the Sentinel-2 Mission. **The International Archives of Photogrammetry, Remote Sensing and Spatial Information Sciences**, v. 40, n. 7, p. 1249, 2015.

MALENOVSKÝ, Z.; ROTT, H.; CIHLAR, J.; SCHAEPMAN, M. E.; GARCÍA-SANTOS, G.; FERNANDES, R.; BERGER, M. Sentinels for science: potential of Sentinel-1, -2, and -3 missions for scientific observations of ocean, cryosphere, and land. **Remote Sensing of Environment**, v. 120, p. 91–101, 2012.

MALHI, Y.; PEGORARO, E.; NOBRE, A. D.; PEREIRA, M. G. P.; GRACE, J.; CULF, A. D.; CLEMENT, R. Energy and water dynamics of a central Amazonian rain forest. **Journal of Geophysical Research: Atmospheres**, v. 107, n. 20, p. 1–17, 2002.

MALHI, Y.; ROBERTS, J. T.; BETTS, R. A.; KILLEEN, T. J.; LI, W.; NOBRE, C. A. Climate change, deforestation, and the fate of the Amazon. **Science**, v. 319, n. 5860, p. 169–72, 2008.

MALTHUS, T. J.; HESTIR, E. L.; DEKKER, A. G.; BRANDO, V. E. The case for a global inland water quality product. In: IEEE INTERNATIONAL GEOSCIENCE AND REMOTE SENSING SYMPOSIUM, 2012, Munich, Germany. **Proceedings…** IEEE, 2012. p. 5234–5237.

MARENGO, J. A. On the hydrological cycle of the Amazon basin: a historical review and current state-of-the-art. **Revista Brasileira de Meteorologia**, v. 21, n. 3, p. 1–19, 2006.

MARENGO, J. A.; NOBRE, C. A.; TOMASELLA, J.; OYAMA, M. D.; DE OLIVEIRA, G. S.; DE OLIVEIRA, R.; CAMARGO, H.; ALVES, L. M.; BROWN, I. F. The drought of Amazonia in 2005. **Journal of Climate**, v. 21, n. 3, p. 495–516, 2008.

MARENGO, J. A.; ESPINOZA, J. C. Extreme seasonal droughts and floods in Amazonia: causes, trends and impacts. **International Journal of Climatology**, v. 36, n. 3, p. 1033–1050, 2016.

MARKHAM, B. L.; BARKER, J. L. Spectral characterization of the Landsat Thematic Mapper sensors. **International Journal of Remote Sensing**, v. 6, n. 5, p. 697-716, 1985.

MARTINS, V.S.; LYAPUSTIN, A; CARVALHO, L.A.S.; BARBOSA, C.C.F.; NOVO, E.M.L.M.. Validation of high-resolution MAIAC aerosol product over South America. **Journal Geophysical Research: Atmospheres**. Under review. 2017.

MARSHAK, A.; WEN, G.; COAKLEY JR., J. A.; REMER, L. A.; LOEB, N. G.; CAHALAN, R. F. A simple model for the cloud adjacency effect and the apparent bluing of aerosols near clouds. **J. geophys. res.**, v. 113, n. D14, p. D14S17, 2008.

MARTIN, S. T.; ANDREAE, M.O.; ARTAXO, P.; BAUMGARDNER, D.; CHEN, Q.; GOLDSTEIN, A. H.; GUENTHER, A.; HEALD, C. L.; MAYOL-BRACERO, O. L; MCMURRY, P. H; PAULIQUEVIS, T.; PÖSCHL, U.; PRATHER, K. A.; ROBERTS, G. C.; SALESKA, S.R.; SILVA DIAS, M.A.; SPRACKLEN, D. V; SWIETLICKI, E.; TREBS, I. Sources and properties of Amazonian aerosol particles. **Reviews of Geophysics**, v. 48, n. 2, 2010.

MARTONCHIK, J. V. et al. Techniques for the retrieval of aerosol properties over land and ocean using multiangle imaging. **IEEE Transactions on Geoscience and Remote Sensing**, v. 36, n. 4, p. 1212-1227, 1998.

MATTHEWS, M. W. A current review of empirical procedures of remote sensing in inland and near-coastal transitional waters. **International Journal of Remote Sensing**, v. 32, n. 21, p. 6855–6899, 2011.

MERTES, L.; SMITH, M.; ADAMS, J. Estimating suspended sediment concentrations in surface waters of the Amazon river wetlands from landsat images. **Remote Sensing of Environment**, v. 43, n. 3, p. 281–301, 1993.

MILLS, G.; PLEIJEL, H.; BRAUN, S.; BÜKER, P.; BERMEJO, V.; CALVO, E.; DANIELSSON, H.; EMBERSON, L.; FERNÁNDEZ, I. G.; GRÜNHAGE, L.; HARMENS, H.; HAYES, F.; KARLSSON, P. E.; SIMPSON, D. New stomatal flux-based critical levels for ozone effects on vegetation. **Atmospheric Environment**, v. 45, n. 28, p. 5064–5068, 2011.

MINOMURA, M.; KUZE, H.; TAKEUCHI, N. Adjacency effect in the atmospheric correction of satellite remote sensing data: evaluation of the influence of aerosol extinction profiles. **Optical Review**, v. 8, n. 2, p. 133–141, 2001.

MISHCHENKO, M. I. Multiple scattering, radiative transfer, and weak localization in discrete random media: unified microphysical approach. **Reviews of Geophysics**, v. 46, n. 2, 2008.

MOBLEY, C. D. Estimation of the remote-sensing reflectance from above-surface measurements. **Applied Optics**, v. 38, n. 36, p. 7442, 1999.

MOBLEY, C. D. Polarized reflectance and transmittance properties of windblown sea surfaces. **Applied optics**, v. 54, n. 15, p. 4828, 2015.

MONKS, P. S.; GRANIER, C.; FUZZI, S.; STOHL, A.; WILLIAMS, M. L.; AKIMOTO, H.; AMANN, M.; BAKLANOV, A.; BALTENSPERGER, U.; BEY, I.; BLAKE, N.; BLAKE, R.S.; CARSLAW, K.; COOPER, O.R.; DENTENER, F. Atmospheric composition change–Global and Regional air quality. **Atmospheric Environment**, v. 43, n. 33, p. 5268-5350, 2009.

MORTON, D. C.; DEFRIES, R. S.; RANDERSON, J. T.; GIGLIO, L.; SCHROEDER, W.; VAN DER WERF, G. R. Agricultural intensification increases deforestation fire activity in Amazonia. **Global Change Biology**, v. 14, n. 10, p. 2262–2275, 2008.

MULLER-WILM, U.; LOUIS, J.; RICHTER, R.; GASCON, F.; NIEZETTE, M. Sentinel-2 level 2A prototype processor: Architecture, algorithms and first results. In: ESA LIVING PLANET SYMPOSIUM, 2013, Edinburgh, UK. **Proceedings…** ESA, 2013. p. 9-13.

MURRAY, L. T.; LOGAN, J. A.; JACOB, D. J. Interannual variability in tropical tropospheric ozone and oh: the role of lightning. **Journal of Geophysical Research: Atmospheres**, v. 118, n. 19, p. 11468–11480, 2013.

NAGY, L.; FORSBERG, B. R.; ARTAXO, P. Interactions between biosphere, atmosphere and human land use in the Amazon Basin. **Ecological studies**, v. 227, p. 3-15, 2016. (ISSN 0070-8356).

NAZEER, M.; NICHOL, J. E.; YUNG, Y. Evaluation of atmospheric correction models and Landsat surface reflectance product in an urban coastal environment. **International Journal of Remote Sensing**, v. 35, n. 16, p. 6271-6291, 2014.

NOBRE, C. A.; OBREGÓN, G. O.; MARENGO, J. A.; FU, R.; POVEDA, G. Characteristics of Amazonian climate: main features. In: **Amazonia and Global change**. American Geophysical Union, 2009. p. 149–162. Change Geophysical Monograph Series 186.

NOBRE, C. A.; SAMPAIO, G.; BORMA, L. S.; CASTILLA-RUBIO, J. C.; SILVA, J. S.; CARDOSO, M. Land-use and climate change risks in the Amazon and the need of a novel sustainable development paradigm. **Proceedings of the National Academy of Sciences of the United States of America**, v. 113, n. 39, p. 10759–10768, 2016.

ODERMATT, D.; GITELSON, A.; BRANDO, V. E.; SCHAEPMAN, M. Review of constituent retrieval in optically deep and complex waters from satellite imagery. **Remote Sensing of Environment**, v. 118, p. 116–126, 2012.

OKIN, G. S.; GU, J. The impact of atmospheric conditions and instrument noise on atmospheric correction and spectral mixture analysis of multispectral imagery. **Remote Sensing of Environment**, v. 164, p. 130–141. 2015.

OLMANSON, L. G.; BAUER, M. E.; BREZONIK, P. L. A 20-year Landsat water clarity census of Minnesota's 10,000 lakes. **Remote Sensing of Environment**, v. 112, n. 11, p. 4086–4097. 2008.

OO, M. M.; JERG, M.; HERNANDEZ, E.; PICON, A.; GROSS, B. M.; MOSHARY, F.; AHMED, S. A. Improved modis aerosol retrieval using modified vis/swir surface albedo ratio over urban scenes. **IEEE Transactions on Geoscience and Remote Sensing**, v. 48, n. 3, p. 983–1000, 2010.

OTTERMAN, J.; FRASER, R. S. Adjacency effects on imaging by surface reflection and atmospheric scattering : cross radiance to zenith. **Applied Optics**, v. 18, n. 16, 1979.

OUAIDRARI, H.; VERMOTE, E. F. Operational atmospheric correction of Landsat TM data. **Remote Sensing of Environment**, v. 70, n. 1, p. 4-15, 1999.

PACIFICO, F.; FOLBERTH, G. A.; SITCH, S.; HAYWOOD, J. M.; RIZZO, L. V.; MALAVELLE, F. F.; ARTAXO, P. Biomass burning related ozone damage on vegetation over the amazon forest: a model sensitivity study. **Atmospheric Chemistry and Physics**, v. 15, n. 5, p. 2791–2804, 2015.

PAHLEVAN, N.; LEE, Z.; WEI, J.; SCHAAF, C. B.; SCHOTT, J. R.; BERK, A. On-orbit radiometric characterization of OLI (LANDSAT-8) for applications in aquatic remote sensing. **Remote Sensing of Environment**, v. 154, p. 272–284, 2014.

PALMER, S. C. J.; KUTSER, T.; HUNTER, P. D. Remote sensing of inland waters: challenges, progress and future directions. **Remote Sensing of Environment**, v. 157, p. 1–8, 2015.

PARK, E.; LATRUBESSE, E. M. Modeling suspended sediment distribution patterns of the Amazon river using modis data. **Remote Sensing of Environment**, v. 147, p. 232–242, 2014.

PETRENKO, M.; ICHOKU, C.; LEPTOUKH, G. Multi-sensor aerosol products sampling system (MAPSS). **Atmospheric Measurement Techniques**, v. 5, n. 5, p. 913–926, 2012.

PÖSCHL,U.; MARTIN, S. T.; SINHA,B.; CHEN, Q.; GUNTHE,S. S.; HUFFMAN, J. A.; BORRMANN, S.; FARMER, D. K.; GARLAND, R. M.; HELAS,G.; JIMENEZ,J. L.; KING, S. M.;MANZI,A.; MIKHAILOV, E.; PAULIQUEVIS,T.; PETTERS, M. D.; PRENNI,A. J.; ROLDIN,P.; ROSE,D.; SCHNEIDER,J.; SU,H.; ZORN,S. R.; ARTAXO,P.; ANDREAE, M. O. Rainforest aerosols as biogenic nuclei of clouds and precipitation in the Amazon. **Science**, v. 329, n. 5998, p. 1513-1516, 2010.

RADOUX, J.; GUILLAUME, C.; JACQUES, D. C.; WALDNER, F.; BELLEMANS N.; MATTON, N.; LAMARCHE, C.; D'ANDRIMONT R.; DEFOURNY, P.. Sentinel-2's potential for sub-pixel landscape feature detection. **Remote Sensing**, v. 8, n. 6, p. 488, 2016.

RAMALHO, E. E.; MACEDO, J.; VIEIRA, T. M.; VALSECCHI, J.; CALVIMONTES, J.;

MARMONTEL, M.; QUEIROZ, H. L. Ciclo hidrológico nos ambientes de várzea. **Uakari**, v. 5, n. 1, p. 61–87, 2009.

REDDINGTON, C. L.; BUTT, E. W.; RIDLEY, D. A; ARTAXO, P.; MORGAN, W. T.; COE, H.; SPRACKLEN, D. V. Air quality and human health improvements from reductions in deforestation-related fire in Brazil. **Nature Geoscience**, v. 8, n. 10, p. 768–771, 2015.

REMER, L. A.; KAUFMAN, Y. J.; TANRÉ, D.; MATTOO, S.; CHU, D. A.; MARTINS, J. V.; LI, R.-R.; ICHOKU, C.; LEVY, R. C.; KLEIDMAN, R. G.; ECK, T. F.; VERMOTE, E.; HOLBEN, B. N. The MODIS aerosol algorithm, products, and validation. **Journal of the Atmospheric Sciences**, v. 62, n. 4, p. 947–973, 2005.

REMER, L. A., S. MATTOO, R. C. LEVY, AND L. A. MUNCHAK. MODIS 3 km aerosol product: algorithm and global perspective. **Atmospheric Measurement Techniques,** v. 6, n. 7, p. 69-112, 2013.

REN, H.; DU, C.; LIU, R.; QIN, Q.; YAN, G.; LI, Z. L.; MENG, J.. Noise Evaluation of early images for Landsat 8 Operational Land Imager. **Optics Express**, v. 22, n. 22, p. 27270-27280, 2014.

ROSENFELD, D.; SHERWOOD, S.; WOOD, R.; DONNER, L. Climate effects of aerosol-cloud interactions. **Science**, v. 343, n. 6169, p. 379–380, 2014.

ROY, D.P.; WULDER, M.A.; LOVELAND, T.R.; WOODCOCK , C.E.; ALLEN, R.G.; ANDERSON, M.C.; HELDER, D.; IRONS,J.R.; JOHNSON, D.M.; KENNEDY, R.; SCAMBOS , T.A.; SCHAAF, C.B.; SCHOTT , J.R.; SHENG ,Y.; VERMOTE , E.F.; BELWARD,A.S.; BINDSCHADLER, R.; COHEN,W.B.; GAO, F.; HIPPLE, J.D.; HOSTERT,P.; HUNTINGTON , J.; JUSTICE , C.O.; KILIC, A.; KOVALSKYY, V.; LEE, Z.P.; LYMBURNER , L.; MASEK, J.G.; MCCORKEL, J.; SHUAI, Y.; TREZZA, R.; VOGELMANN,J.; WYNNE, R.H.; ZHU, Z. Landsat-8: science and product vision for terrestrial global change research. **Remote Sensing of Environment**, v. 145, n.5, p. 154-172, 2014.

FOWLER, D.; AMANN, M.; ANDERSON, F.; ASHMORE, M.; COX, P.; DEPLEDGE, M. et al. (eds). **Ground-level ozone in the 21st century:** future trends, impacts and policy implications. London : The Royal Society, 2008. 132 p. (Royal Society Policy Document 15/08).

RUMMEL, U.; AMMANN, C.; KIRKMAN, G. A.; MOURA, M. A. L.; FOKEN, T.; ANDREAE, M. O.; MEIXNER, F. X.. Seasonal variation of ozone deposition to a tropical rain forest in Southwest Amazonia. **Atmospheric Chemistry and Physics**, v. 7, n. 20, p. 5415–5435, 2007.

SALOMONSON, V. V.; BARNES, W. L.; MAYMON, P. W.; MONTGOMERY, H. E.; OSTROW, H. MODIS: advanced facility instrument for studies of the Earth as a system. **IEEE Transactions on Geoscience and Remote Sensing**, v. 27, n. 2, p. 145–153, 1989.

SAMPAIO, G.; NOBRE, C.; COSTA, M. H.; SATYAMURTY, P.; SOARES-FILHO, B. S.; CARDOSO, M. Regional climate change over eastern amazonia caused by pasture and soybean cropland expansion. **Geophysical Research Letters**, v. 34, n. 17, p. 1–7, 2007.

SAYER, A. M.; HSU, N. C.; BETTENHAUSEN, C.; JEONG, M. J. Validation and uncertainty estimates for MODIS Collection 6 “Deep Blue” aerosol data. **Journal of Geophysical Research: Atmospheres**, v. 118, n. 14, p. 7864–7872, 2013.

SCHAFER, J. S.; ECK, T. F.; HOLBEN, B. N.; ARTAXO, P.; DUARTE, A. F. Characterization of the optical properties of atmospheric aerosols in Amazônia from long-term aeronet monitoring (1993–1995 and 1999–2006). **Journal of Geophysical Research**, v. 113, n. 4, 2008.

SCHMID, B.; THORNE, K. J.; DEMOULIN, P.; PETER, R.; MÄTZLER, C.; SEKLER, J. Comparison of modeled and empirical approaches for retrieving columnar water vapor from solar transmittance measurements in the 0.94-μm region. **Journal of Geophysical Research: Atmospheres**, v. 101, p. 9345–9358. 1996.

SCHUSTER, G. L.; DUBOVIK, O.; HOLBEN, B. N. Angstrom exponent and bimodal aerosol size distributions. **Journal of Geophysical Research: Atmospheres**, v. 111, n. 7, p. 1–14, 2006.

SEEMANN, S. W.; LI, J.; MENZEL, W. P.; GUMLEY, L. E. Operational retrieval of atmospheric temperature, moisture, and ozone from MODIS infrared radiances. **Journal of Applied Meteorology**, v. 42, p. 1072–1091, 2003.

SEI, A. Efficient correction of adjacency effects for high- resolution imagery: integral equations, analytic continuation, and padé approximants. **Applied Optics**, v. 54, n. 12, p. 3748–3758, 2015.

SEIDEL, F. C.; POPP, C. Critical surface albedo and its implications to aerosol remote sensing. **Atmospheric Measurement Techniques**, v. 5, n. 7, p. 1653–1665, 2012.

SHI, W.; WANG, M. An assessment of the black ocean pixel assumption for MODIS SWIR bands. **Remote Sensing of Environment**, v. 113, n. 8, p. 1587–1597, 2009.

SHI, Y.; ZHANG, J.; REID, J. S.; HYER, E. J.; ECK, T. F.; HOLBEN, B. N.; KAHN, R. A. Where do we need additional in situ aerosol and sun photometer data: a critical examination of spatial biases between MODIS and MISR aerosol products. **Atmospheric Measurement Techniques Discussions**, v. 4, n. 4, p. 4295–4323. 2011.

SIERRA, J. P.; ARIAS, P. A; VIEIRA, S. C. Precipitation over northern South America and its seasonal variability as simulated by the CMIP5 models. **Advances in Meteorology**, v. 2015, p. 1–22, 2015.

SOBOLEV, V. V. **Light scattering in planetary atmospheres**. Oxford and New York, Pergamon Press. v. 1, p. 263, 1975.

SONG, C.; WOODCOCK, C. E.; SETO, K. C.; LENNEY, M. P.; MACOMBER, S. A.. Classification and change detection using Landsat TM data: When and how to correct atmospheric effects? **Remote sensing of Environment**, v. 75, n. 2, p. 230-244, 2001.

SUN, J.; XIONG, X.; ANGAL, A.; CHEN, H.; GENG, X.; WU. A. On-orbit performance of the MODIS reflective solar bands time-dependent response versus scan angle algorithm. **Proc. SPIE 8510, Earth Observing Systems XVII**, 85100J (October 15, 2012); doi:10.1117/12.930021. 2012.

SUPERCZYNSKI, S. D., S. KONDRAGUNTA, AND A. I. LYAPUSTIN. Evaluation of the multi-angle implementation of atmospheric correction (MAIAC) aerosol algorithm through intercomparison with VIIRS aerosol products and AERONET. **Journal of Geophysical Research: Atmospheres**, v.122, n. 5, p. 3005-3022, 2017.

TOLLER, G., X. XIONG, J. SUN, B. N. WENNY, X. GENG, J. KUYPER, A. ANGAL, H. CHEN, S. MADHAVAN, AND A. WU. Terra and Aqua moderate-resolution imaging spectroradiometer collection 6 level 1B algorithm. **Journal of Applied Remote Sensing**, p. 7, n. 1, p. 073557-073557, 2013.

SRIWONGSITANON, N.; SURAKIT, K.; THIANPOPIRUG, S. Influence of atmospheric correction and number of sampling points on the accuracy of water clarity assessment using remote sensing application. **Journal of Hydrology**, v. 401, n. 3–4, p. 203–220, 2011.

STERCKX, S.; KNAEPS, S.; KRATZER, S.; RUDDICK, K. Similarity environment correction (SIMEC) applied to MERIS data over inland and coastal waters. **Remote Sensing of Environment**, v. 157, p. 96–110, 2015.

TANRE, D.; HERMAN, M.; DESCHAMPS, P. Y. Influence of the background contribution upon space measurements of ground reflectance. **Applied Optics**, v. 20, p. 3676–3684, 1981.

TAYLOR, M.; KAZADZIS, S.; AMIRIDIS, V.; KAHN, R. A. Global aerosol mixtures and their multiyear and seasonal characteristics. **Atmospheric Environment**, v. 116, p. 112–129, 2015.

TEBBS, E. J.; REMEDIOS, J. J.; HARPER, D. M. Remote sensing of chlorophyll-a as a measure of cyanobacterial biomass in lake Bogoria, a hypertrophic, saline–alkaline, flamingo lake, using landsat ETM+. **Remote Sensing of Environment**, v. 135, p. 92–106, 2013.

TOMING, K.; KUTSER, T.; LAAS, A.; SEPP, M.; PAAVEL, B.; NÕGES, T. First experiences in mapping lake water quality parameters with Sentinel-2 MSI imagery. **Remote Sensing**, v. 8, n. 8, p. 640, 2016.

VANHELLEMONT, Q.; RUDDICK, K. Turbid wakes associated with offshore wind turbines observed with LANDSAT 8. **Remote Sensing of Environment**, v. 145, p. 105–115, 2014.

VANHELLEMONT, Q.; RUDDICK, K. Advantages of high quality SWIR bands for ocean colour processing: examples from LANDSAT-8. **Remote Sensing of Environment**, v. 161, p. 89–106, 2015.

VANHELLEMONT, Q.; RUDDICK, K. ACOLITE for Sentinel-2: aquatic applications of MSI imagery. ESA LIVING PLANET SYMPOSIUM, 2016, Prague, Czech Republic. **Proceedings...** ESA, 2016. p. 9–13.

VERA, C.; BAEZ, J.; DOUGLAS, M.; EMMANUEL, C. B.; MARENGO, J.; MEITIN, J.;

NICOLINI, M.; NOGUES-PAEGLE, J.; PAEGLE, J.; PENALBA, O.; SALIO, P.; SAULO, C.; SILVA DIAS, M. A.; SILVA DIAS, P.; ZIPSER, E. The South American low-level jet experiment. **Bulletin of the American Meteorological Society**, v. 87, n. 1, p. 63–77, 2006.

VERBESSELT, J.; HYNDMAN, R.; NEWNHAM, G.; CULVENOR, D. Detecting trend and seasonal changes in satellite image time series. **Remote Sensing of Environment**, v. 114, n. 1, p. 106–115, 2010.

VERMOTE, E. F.; EL SALEOUS, N.; JUSTICE, C. O.; KAUFMAN, Y. J.; PRIVETTE, J. L.; REMER, L.; ROGER, J. C.; TANRÉ, D. Atmospheric correction of visible to middle-infrared EOS-MODIS data over land surfaces: background, operational algorithm and validation. **Journal of geophysical research**, v. 102, n. D14, p. 17131-17141, 1997a.

VERMOTE, E. F.; TANRÉ, D.; DEUZÉ, J. L.; HERMAN, M.; MORCRETTE, J. J. Second Simulation of the Satellite Signal in the Solar Spectrum, 6S: an overview. **IEEE Transactions on Geoscience and Remote Sensing**, v. 35, n. 3, p. 675–686, 1997b.

VERMOTE, Eric F.; EL SALEOUS, Nazmi Z.; JUSTICE, Christopher O. Atmospheric correction of MODIS data in the visible to middle infrared: first results. **Remote Sensing of Environment**, v. 83, n. 1, p. 97-111, 2002.

VERMOTE, E. F.; KOTCHENOVA, S. Atmospheric correction for the monitoring of land surfaces. **Journal of Geophysical Research: Atmospheres**, v. 113, n. 23, 2008.

VERMOTE, E.; JUSTICE, C.; CLAVERIE, M.; FRANCH, B. Preliminary analysis of the performance of the LANDSAT 8/OLI land surface reflectance product. **Remote Sensing of Environment**, v. 185, p. 46–56, 2016.

VIDELA, F. C.; BARNABA, F.; ANGELINI, F.; CREMADES, P.; GOBBI, G. P. The relative role of Amazonian and non-Amazonian fires in building up the aerosol optical depth in South America: a five year study (2005-2009). **Atmospheric Research**, v. 122, p. 298–309, 2013.

VÖRÖSMARTY, C. J.; MCINTYRE, P. B.; GESSNER, M. O.; DUDGEON, D.; PRUSEVICH, A; GREEN, P.; GLIDDEN, S.; BUNN, S. E.; SULLIVAN, C. A; LIERMANN, C. R.; DAVIES, P. M. Global threats to human water security and river biodiversity. **Nature**, v. 467, n. 7315, p. 555–561, 2010.

VUILLE, M.; BURNS, S. J.; TAYLOR, B. L.; CRUZ, F. W.; BIRD, B. W.; ABBOTT, M. B.; KANNER, L. C.; CHENG, H.; NOVELLO, V. F. A review of the South American monsoon history as recorded in stable isotopic proxies over the past two millennia. **Climate of the Past**, v. 8, n. 4, p. 1309–1321, 2012.

WALLACE, J. M.; HOBBS, P. V. **Atmospheric science:** an introductory survey. Academic press, 2006.

WANG, D.; MORTON, D.; MASEK, J.; WU, A.; NAGOL, J.; XIONG, X.; LEVY, R.; VERMOTE, E.;WOLFE, R. Impact of sensor degradation on the MODIS NDVI time series. **Remote Sensing of Environment**, v. 119, p. 55-61, 2012.

WANG, J.; KREJCI, R.; GIANGRANDE, S.; KUANG, C.; BARBOSA, H. M. J.; BRITO, J.; CARBONE, S.; CHI, X.; COMSTOCK, J.; DITAS, F.; LAVRIC, J.; MANNINEN, H. E.; MEI, F.; ZULOAGA, D. M.; PÖHLKER, C.; PÖHLKER, M. L.; SATURNO, J.; SCHMID, B.; SOUZA, R. A. F.; SPRINGSTON, S. R.; TOMLINSON, J. M.; TOTO, T.; WALTER, D.; WIMMER, D.; SMITH, J. N.; KULMALA, M.; MACHADO, L. A. T.; ARTAXO, P.; ANDREAE, M. O.; PETÄJÄ, T.; MARTIN, S. T. Amazon boundary layer aerosol concentration sustained by vertical transport during rainfall. **Nature**, v. 539, n. 7629, p. 416-419, 2016.

WIEDINMYER, C. Atmospheric chemistry: breathing easier in the Amazon. **Nature Geoscience**, v. 8, n. 10, p. 751–752, 2015.

WILSON, R. T. Py6s: a python interface to the 6s radiative transfer model. **Computers and Geosciences**, v. 51, p. 166–171, 2013.

XIE, Y.; ZHANG, Y.; XIONG, X.; QU, J. J.; CHE, H. Validation of MODIS aerosol optical depth product over China using CARSNET measurements. **Atmospheric Environment**, v. 45, n. 33, p. 5970–5978, 2011.

XIONG, X.; ANGAL, A.; WU, A.; LINK, D.; GENG, X.; BARNES, W.; SALOMONSON, V. Sixteen years of Terra MODIS on-orbit operation, calibration, and performance. **Proc. SPIE 10000**, Sensors, Systems, and Next-Generation Satellites XX, doi:10.1117/12.2241352. 2016.

YU, H.; KAUFMAN, Y. J.; CHIN, M.; FEINGOLD, G.; REMER, L. A.; ANDERSON, T. L.; BALKANSKI, Y.; BELLOUIN, N.; BOUCHER, O.; CHRISTOPHER, S.; DECOLA, P.; KAHN, R.; KOCH, D.; LOEB, N.; REDDY, M. S.; SCHULZ, M.; TAKEMURA, T.; ZHOU, M. A review of measurement-based assessments of the aerosol direct radiative effect and forcing. **Atmospheric Chemistry and Physics**, v. 6, p. 613–666, 2006.

ZELAZOWSKI, P., SAYER, A. M., THOMAS, G. E., & GRAINGER, R. G. Reconciling satellite-derived atmospheric properties with fine-resolution land imagery: insights for atmospheric correction. **Journal of Geophysical Research: Atmospheres**, v. 116, n. 18, 2011.

ZIEMKE, J. R.; CHANDRA, S.; DUNCAN, B. N.; SCHOEBERL, M. R.; TORRES, O.; DAMON, M. R.; BHARTIA, P. K. Recent biomass burning in the tropics and related changes in tropospheric ozone. **Geophysical Research Letters**, v. 36, n. 15, p. 1–5, 2009.